



# ATLAS NOTE

SUSY-2016-08

19th July 2017



Draft version 2.0

## Search for long-lived, heavy particles using displaced multi-track vertices in 13 TeV $pp$ collisions

Karri DiPetrillo<sup>h</sup>, Jordi Duarte-Campderros<sup>a</sup>, Dominik Krauss<sup>b</sup>, Lawrence Lee Jr<sup>h</sup>, Kazuki Motohashi<sup>c</sup>, Christian Ohm<sup>d</sup>, Hideyuki Oide<sup>e</sup>, Hidetoshi Otono<sup>f</sup>, Nora Emilia Pettersson<sup>g</sup>, Jennifer Roloff<sup>h</sup>, Abner Soffer<sup>a</sup>

<sup>a</sup>Tel Aviv University

<sup>b</sup>Max-Planck-Institut fuer Physik

<sup>c</sup>Tokyo Institute of Technology

<sup>d</sup>Lawrence Berkeley National Lab.

<sup>e</sup>University of Genova

<sup>f</sup>Kyushu University

<sup>g</sup>University of Massachusetts

<sup>h</sup>Harvard University

### Abstract

We report on a search for long-lived heavy particles produced in  $pp$  collisions at 13 TeV centre-of-mass energy with the ATLAS detector at the LHC. The search is sensitive to processes yielding events containing at least one displaced high-mass vertex and large missing transverse momentum. The search is based on a dataset with luminosity  $32.7 \text{ fb}^{-1}$  which was collected by the ATLAS detector in 2016. The observed yield is consistent with the background-only hypothesis and the results are interpreted in the context of models with long-lived gluinos (e.g. Split SUSY)

## 24 **Contents**

25	<b>0 Updates since 1st circulation</b>	4
26	<b>1 Introduction</b>	4
27	<b>2 Data and Monte Carlo samples</b>	5
28	2.1 Data sample	5
29	2.1.1 The DRAW_RPVLL format	5
30	2.1.2 The DAOD_SUSY15 format	7
31	2.1.3 Data quality requirements	7
32	2.2 Monte Carlo samples	7
33	2.2.1 Signal: decaying $R$ -hadrons	7
34	2.2.2 Other Monte Carlo samples	10
35	<b>3 Event selection</b>	12
36	3.1 Event pre-selection	13
37	3.1.1 Non-collision background	14
38	3.2 Special reconstruction	17
39	3.2.1 Tracking	17
40	3.2.2 Reconstruction of secondary vertices	18
41	3.3 Final event selection	20
42	3.4 Vertex selection	20
43	3.5 Material map	21
44	<b>4 Selection efficiency</b>	25
45	4.1 Event and vertex yields	25
46	4.2 Vertex reconstruction efficiency as a function of radial position	25
47	4.3 Reweighting efficiencies for intermediate lifetimes	27
48	<b>5 Background estimation</b>	30
49	5.1 Overview of control, validation and signal regions	30
50	5.2 Hadronic Interaction	30
51	5.3 Merged Vertices	33
52	5.4 Randomly crossing tracks	34
53	5.4.1 Seed vertices and track templates	36
54	5.4.2 Constructing the invariant mass templates	37
55	5.5 Validation of the background estimation	39
56	5.5.1 Low- $E_T^{\text{miss}}$ Validation Region - VRLM	42
57	5.5.2 Material-dominated Validation Region - VRM	46
58	5.6 Total background estimate and event-selection transfer factor	48
59	5.7 Systematic uncertainties on the background estimation	52
60	<b>6 Systematic uncertainties</b>	55
61	6.1 Uncertainty on tracking and vertexing efficiencies	55
62	6.2 Uncertainty on $E_T^{\text{miss}}$ selection	56
63	6.3 Uncertainty on jet selection	58
64	6.4 Uncertainty related to ISR	58

65	6.5	Uncertainty due to pileup re-weighting	59
66	6.6	Summary of uncertainties on the efficiency	59
67	6.7	Signal efficiency vs lifetime including all systematic uncertainty	61
68	<b>7</b>	<b>Results</b>	<b>62</b>
69	7.1	Final yields	62
70	7.2	Distributions	62
71	<b>8</b>	<b>Interpretation of results</b>	<b>66</b>
72	<b>9</b>	<b>Conclusions</b>	<b>69</b>
73	<b>Appendix</b>		<b>70</b>
74	<b>A</b>	<b>Samples details</b>	<b>71</b>
75	<b>B</b>	<b>Monte Carlo signal cut flows</b>	<b>79</b>
76	<b>C</b>	$E_T^{\text{miss}}$ cut dependence on signal	<b>80</b>
77	<b>D</b>	<b>SUSY Background Forum analysis checklist items</b>	<b>81</b>
78	<b>E</b>	<b>Large radius tracking validation</b>	<b>84</b>
79	<b>F</b>	<b>Hadronic interactions</b>	<b>89</b>
80	F.1	Hadronic interactions in material-dominated detector regions	89
81	F.2	GEANT4 studies	92
82	<b>G</b>	<b>Vertex pileup dependence</b>	<b>94</b>
83	<b>H</b>	<b>Primary vertex reconstruction under R-hadron presence</b>	<b>98</b>
84	<b>I</b>	<b>Lifetime re-weighting</b>	<b>102</b>
85	<b>J</b>	<b>JES and JER uncertainties due to displacement</b>	<b>103</b>
86	<b>K</b>	<b>Parametrized Efficiencies for Reinterpretation</b>	<b>107</b>
87	K.1	Definition of Acceptances	107
88	K.2	Efficiencies	108
89	K.3	Closure Test	115
90	<b>Auxiliary material</b>		<b>120</b>

## 91 0. Updates since 1st circulation

92 Since first circulation, several minor items have changed.

- 93     • Some errors were found in the interpolation of the 2D limit plots as well as in the values that were  
94       being interpolated. These have been fixed below. Instabilities are fixed due to the change but the  
95       overall physics message is not hugely affected.
  - 96           – Specifically, the upper limit in a scan of signal strength  $\mu$  was being plotted instead of the  
97           convention of using the CLs values at fixed  $\mu$ .
  - 98           – More importantly, the interpolation involved connecting those grid points available that were  
99           deemed excluded. This was done instead of doing a proper interpolation to find the contour  
100          of iso-CLs used to define the 95% CL lines. Fixing this gives rise to more physical shapes that  
101          is insensitive to effects like signal grid spacing.
- 102     • The additional uncertainties due to measurements of jets produced with some displacement have  
103       been assessed. Over the available fiducial volume, the JES varies only 2-3%, within the existing  
104       uncertainties, while the JER varies as much as 50% for extreme displacements outside of the nominal  
105        $\approx 5\%$  JER uncertainty. However, taking this maximum value as a very conservative envelope  
106       yields an additional uncertainty of order 5% which has been taken into account.
- 107     • Reinterpretation material has been completed factorizing event-, track-, and vertex-level acceptance  
108       and efficiencies for use by the outside community.

## 109 1. Introduction

110 Searches for massive long-lived particles are an important part of the search program for new physics at  
111 the LHC [1]. Pioneering work was done in the ATLAS experiment with  $pp$  collisions at  $\sqrt{s} = 7$  TeV  
112 in 2010 [2, 3], which focused on a signature with displaced vertices associated with high- $p_T$  muons,  
113 predicted in a specific  $R$ -parity violating model [4]. The same signature was investigated with the 2011  
114 data [5, 6] and 2012 data [7, 8]. Following these searches, other signatures with displaced vertices were  
115 explored in the 2012 data, i.e., a displaced vertex associated with a high- $p_T$  electron, or in an event with  
116 several high- $p_T$  jets or large missing transverse energy ( $E_T^{\text{miss}}$ ) [9–11], which can feature in more general  
117  $R$ -parity violating model [4], a Split SUSY model [12] and a Gauge-Mediated SUSY model [13].

118 In this work, we use  $32.7 \text{ fb}^{-1}$   $pp$  collision data at  $\sqrt{s} = 13$  TeV recorded in 2016. As the first such search  
119 in Run II, we target signatures with at least one displaced vertex and significant  $E_T^{\text{miss}}$ . This channel is  
120 sensitive to large regions of phase space in the various signal models and has the benefit that complex  
121 uncertainties related to the reconstruction of muons and electrons from displaced decays are avoided.  
122 A Split SUSY model [12] is considered here and features pair-production of long-lived gluinos which  
123 hadronise into  $R$ -hadrons before decaying into two quarks and neutralino shown as Fig 1.

124 The previous search in Run I [9–11] targeted high-mass gluino with a fixed neutralino mass at 100 GeV, so  
125 that we could require at least two energetic “trackless” jets by  $E_T > 50$  GeV and  $\text{SumPtTrack} < 5$  GeV,  
126 i.e., total  $p_T$  of tracks from the primary vertices pointing towards this jet is less than 5 GeV. The search  
127 presented in this note also targets scenarios with a small mass difference between the gluino and the  
128 neutralino, which is favoured from the relic dark matter abundance [14].

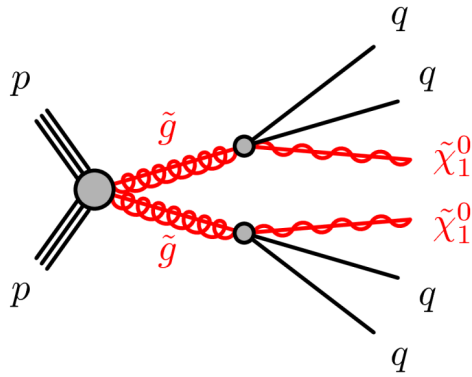


Figure 1: Feynman diagram representing production of long-lived gluinos in a Split SUSY model, which form  $R$ -hadrons and give rise to displaced decays with hadronic final states.

## <sup>129</sup> 2. Data and Monte Carlo samples

### <sup>130</sup> 2.1. Data sample

<sup>131</sup> The analysis uses the full 25 ns  $pp$  dataset from 2016. As the standard ATLAS tracking algorithms are  
<sup>132</sup> inefficient for finding tracks with impact parameters as large as expected for the sought signal, track re-  
<sup>133</sup> construction has to be re-run with relaxed settings downstream in the analysis workflow. Since this Large  
<sup>134</sup> Radius Tracking processing (see Section 3) requires low-level data, we make use of the DRAW\_RPVLL [15]  
<sup>135</sup> described below, and the DAOD\_SUSY15 derivation format.

<sup>136</sup> As a brief executive summary, here is an overview of the workflow and the various formats for the pro-  
<sup>137</sup> cessing of the data:

<sup>138</sup> `RAW => DRAW_RPVLL (Tier-0 f-tags) => DAOD_RPVLL (r8669) => DAOD_SUSY15 (p2875)`

<sup>139</sup> The Run II data used for this analysis are from datasets matching the following patterns:

<sup>140</sup> `DRAW_RPVLL : data16_13TeV.*.physics_Main.merge.DRAW_RPVLL.f*_m*`  
<sup>141</sup> `DAOD_RPVLL : data16_13TeV.*.physics_Main.recon.DAOD_RPVLL.f*_r8669`  
<sup>142</sup> `DAOD_SUSY15 : data16_13TeV.*.physics_Main.recon.DAOD_RPVLL.f*_r8669_p2875`

<sup>143</sup> Table 1 describes the various data periods and their corresponding integrated luminosity for the dataset  
<sup>144</sup> used in this search.

#### <sup>145</sup> 2.1.1. The DRAW\_RPVLL format

<sup>146</sup> This data format is designed specifically to give access to low-level detector and reconstruction informa-  
<sup>147</sup> tion for searches that need to do custom reconstruction or use unconventional variables based on low-level  
<sup>148</sup> detector data. To minimize the disk space used by this format, only a small subset of events are made  
<sup>149</sup> available this way. To select them, tight trigger and offline selections are applied to “skim” the data, while

Table 1: Data taking periods and the corresponding amounts of the integrated luminosity for the 2016 dataset after the application of data quality requirements. Runs in period H were recorded with the beam condition of low  $\mu$  for forward physics. Runs in period J were taken with  $\beta^* = 2.5$  km for the measurement of elastic pp-scattering by the “Absolute Luminosity For ATLAS” (ALFA) detector.

Period	Run Numbers	Dates	$\int \mathcal{L} dt [pb^{-1}]$
A	297730 - 300279	28 Apr. - 27 May.	552.7
B	300345 - 300908	27 May. - 06 Jun.	1922.6
C	301912 - 302393	11 Jun. - 21 Jun.	2861.3
D	302737 - 303560	24 Jun. - 10 Jul.	4624.2
E	303638 - 303892	10 Jul. - 16 Jul.	1481.0
F	303943 - 304494	16 Jul. - 25 Jul.	3398.9
G	305380 - 306451	02 Aug. - 17 Aug.	3818.4
H	N/A	N/A	N/A
I	307126 - 308084	25 Aug. - 10 Sep.	5760.7
J	N/A	N/A	N/A
K	309375 - 309759	26 Sep. - 03 Oct.	2191.6
L	310015 - 311481	06 Oct. - 26 Oct.	6127.5
A-L	297730 - 311481	28 Apr. - 26 Oct.	32739.0

150 retaining the full RAW contents for the selected events. The filters for the 2016 DRAW\_RPVLL dataset  
 151 related to this search required any of the following triggers:

- 152 • HLT\_xeXX
- 153 • HLT\_xeXX\_tc\_lcw
- 154 • HLT\_xeXX\_mht\_L1XEYY
- 155 • HLT\_xe110\_mht\_L1XE50\_AND\_xe70\_L1XE50
- 156 • HLT\_xeXX\_topoclPS
- 157 • HLT\_xeXX\_topoclPUC

158 where XX = 90, 100, 110, 120, 130 and YY = 50, 55, 60. On top of the trigger requirement, the following  
 159 offline criteria were applied depending on the data taking period:

- 160 **Periods A-J:** MET\_LocHadTopo > 130 GeV AND any of the following requirements:
- at least one jet with  $p_T > 70$  GeV and  $\text{SumPtTrk} < 5$  GeV,
  - at least two jets with  $p_T > 25$  GeV and  $\text{SumPtTrk} < 5$  GeV,
  - $\text{Rnd}() < 0.05$  (prescale factor of 20),  
 where  $\text{SumPtTrk} = \sum p_T$  of tracks from the PV (with  $p_T > 0.5$  GeV) associated to the jet

- 162 **Periods K-L:** MET\_LocHadTopo > 180 GeV

163 The trackless-jet requirement was used in the Run I analyses where the targeted scenarios predicted  
 164 significant hadronic activity. This search also targets scenarios with small mass differences between the  
 165 long-lived particle and the LSP (see Section 1) which do not provide displaced jets with enough energy to  
 166 fulfill the trackless jet requirements. For this reason, the DRAW filter for the DV searches was changed

167 during the year to instead use a simple (but tighter) requirement on MET\_LocHadTopo in the processing  
 168 at Tier-0. This is justified by the increased signal efficiencies for the compressed signal scenarios shown  
 169 in Section 2.2.

170 The data was processed at Tier-0 throughout the year, and a small subset of events were streamed out to  
 171 the DRAW\_RPVLL format. The selection for this stream is implemented in LongLivedParticleDPDMaker  
 172 and the skimming changed during the year. As described above, the  $E_T^{\text{miss}}$ -based DV filter changed signifi-  
 173 cantly between periods J and K. The last run to be processed with the old filter was 308084 (using AMI  
 174 tag f741, 20.7.7.9), and the first to be processed by the new was 309311 (using f746, 20.7.8.1).

175 The events in the tightly skimmed DRAW\_RPVLL datasets were then processed centrally on the grid by the  
 176 reprocessing coordinators using **AtlasProduction 20.7.8.7** and the r8669 configuration. Note that  
 177 this configuration includes the third-pass tracking with looser cuts, the so-called *Large Radius Tracking*  
 178 (LRT) described in Section 3.2.1; and the specialized vertex algorithm using the tracks from the LRT and  
 179 the standard tracking as inputs (see Section 3.2.2). The output DAOD\_RPVLL is a normal AOD but with  
 180 additional tracks from the LRT mode and a vertex collection from the VrtSecInclusive algorithm that  
 181 reconstructs secondary vertices [16].

### 182 2.1.2. The DAOD\_SUSY15 format

183 Finally, for further data reduction and in order to apply so-called “AOD-fix” corrections, a proper deriva-  
 184 tion, DAOD\_SUSY15, is produced from the DAOD\_RPVLL. This further skims the data sample by selecting  
 185 the events passing any of a set of triggers defined within the SUSY and Exotics long-lived searches  
 186 groups. This list includes the lowest-threshold unprescaled  $E_T^{\text{miss}}$  triggers used by this analysis. The full  
 187 list of triggers is available in Ref. [17]. Note that no skimming is applied in the SUSY15 step when  
 188 processing the MC.

### 189 2.1.3. Data quality requirements

190 Due to the special processing above, a small number of luminosity blocks were processed incompletely,  
 191 and these are therefore rejected by masking them out manually using a modified version of the standard  
 192 Good Runs List. The reasons for the failing jobs are not related to the event content, so this loss does not  
 193 bias the analysis. The modified GRL is available in the gitlab repository for the analysis:

194 [data16\\_13TeV\\_periodAllYear\\_DetStatus-v83-pro20-15\\_DQDefects-00-02-04\\_PHYS\\_StandardGRL\\_All\\_Good\\_25ns\\_DAOD\\_RPVLL\\_r8669.xml](#)

195 The surviving data corresponds to an integrated luminosity of  $32.7 \text{ fb}^{-1}$  when evaluated with the **0flLumi-13TeV-008**  
 196 calibration tag (compared to the nominal GRL, 0.37% is lost due to incomplete processing).

## 197 2.2. Monte Carlo samples

### 198 2.2.1. Signal: decaying $R$ -hadrons

199 Simulation of  $R$ -hadrons is technically challenging and described in detail elsewhere [18]. The generator  
 200 PYTHIA 6.427 [19] is used to simulate gluino production and hadronisation, and the resulting  $R$ -hadron  
 201 is passed through specialised routines in GEANT4 [20] to simulate their propagation through the detector.

202 Pythia routines then decay the  $R$ -hadron into quark pairs plus a neutralino. Samples are prepared for  
 203 gluino masses varying from 600 GeV to 2000 GeV. The neutralino mass is fixed at 100 GeV for one  
 204 set of samples. For another set,  $m_{\tilde{\chi}^0}$  is varied so that the mass difference from gluino become 30 GeV,  
 205 50 GeV, 80 GeV or 130 GeV. Further details and sample parameters can be found at Appendix A. The  
 206 proper decay length is also scanned with some samples produced at  $\tau = 0.04, 0.01, 0.4, 1, 3, 10, 30, 50$   
 207 ns. Figure 2 shows the dataset identification (DSid) for the available MC signal samples in the different  
 mass and proper decay length planes.

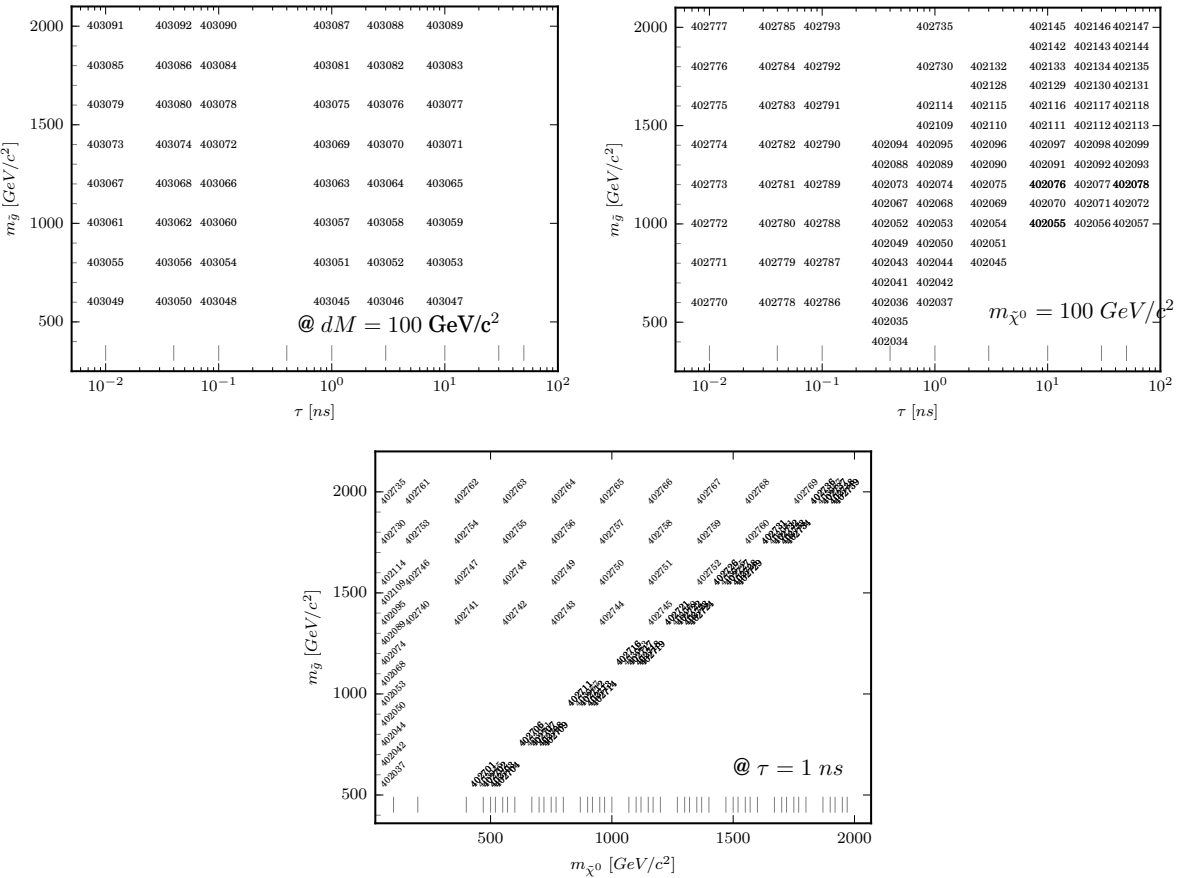


Figure 2: Dataset identification numbers (DSIDs) for the MC samples in the different planes: the top plots shows the gluino mass vs. the proper decay length, at fixed gluino-neutralino mass difference for the top-left figure, and at fixed neutralino mass of 10 GeV for the top-right one. The bottom figure is plotting the DSIDs in the the gluino vs. neutralino mass plane at fixed proper decay length (1 ns)

208

209 For each model point 10k events are generated. The samples are produced in the standard ATLAS and  
 210 MC15c configuration [21] augmented with special options for the GEANT4 detector simulation of the long-  
 211 lived particles (e.g. interactions and decays of  $R$ -hadrons) and the Large Radius Tracking option and a  
 212 special secondary-vertexing algorithm in the reconstruction step. The samples are processed centrally  
 213 from HITS<sup>1</sup> using **AtlasProduction 20.7.8.8** and the **r8788** configuration tag. The DAOD\_SUSY15

<sup>1</sup> To ensure that the processing is consistent with the data reconstructed from DRAW\_RPVLL.

Not reviewed, for internal circulation only

214 derivations are then made using the p2877 tag. The samples used for optimization and analysis design  
 215 are listed below.

```
216 mc15_13TeV.402073.PythiaRhad_AUET2BCTEQ6L1_gen_gluino_p1_1200_qq_100_p4ns.recon.DAOD_RPVLL.e4809_s2810_s2183_r8788
217 mc15_13TeV.402074.PythiaRhad_AUET2BCTEQ6L1_gen_gluino_p1_1200_qq_100_1ns.recon.DAOD_RPVLL.e4620_s2770_s2183_r8788
218 mc15_13TeV.402075.PythiaRhad_AUET2BCTEQ6L1_gen_gluino_p1_1200_qq_100_3ns.recon.DAOD_RPVLL.e4620_s2770_s2183_r8788
219 mc15_13TeV.402716.PythiaRhad_AUET2BCTEQ6L1_gen_gluino_p1_1200_qq_1070_1ns.recon.DAOD_RPVLL.e4732_s2821_s2183_r8788
220 mc15_13TeV.402717.PythiaRhad_AUET2BCTEQ6L1_gen_gluino_p1_1200_qq_1120_1ns.recon.DAOD_RPVLL.e4732_s2821_s2183_r8788
221 mc15_13TeV.402718.PythiaRhad_AUET2BCTEQ6L1_gen_gluino_p1_1200_qq_1150_1ns.recon.DAOD_RPVLL.e4732_s2821_s2183_r8788
222 mc15_13TeV.402719.PythiaRhad_AUET2BCTEQ6L1_gen_gluino_p1_1200_qq_1170_1ns.recon.DAOD_RPVLL.e4732_s2821_s2183_r8788
223 mc15_13TeV.402735.PythiaRhad_AUET2BCTEQ6L1_gen_gluino_p1_2000_qq_100_1ns.recon.DAOD_RPVLL.e4732_s2770_s2183_r8788
224 mc15_13TeV.402777.PythiaRhad_AUET2BCTEQ6L1_gen_gluino_p1_2000_qq_100_p01ns.recon.DAOD_RPVLL.e5220_s2821_r8788
225 mc15_13TeV.402785.PythiaRhad_AUET2BCTEQ6L1_gen_gluino_p1_2000_qq_100_p04ns.recon.DAOD_RPVLL.e5220_s2821_r8788
226 mc15_13TeV.402793.PythiaRhad_AUET2BCTEQ6L1_gen_gluino_p1_2000_qq_100_p1ns.recon.DAOD_RPVLL.e5220_s2821_r8788
227
```

228 The rest of the signal MC samples used for interpretation of the results are all available in DAOD\_SUSY15  
 229 derivation format as well.

230 As for most physics MC samples, additional  $pp$  minimum-bias interactions simulated using PYTHIA 8 [22]  
 231 are overlaid on the signal events to model the pileup. During the analysis processing, all simulated events  
 232 are re-weighted such that the distribution of  $\mu$  (the average number of  $pp$  interactions per bunch crossing)  
 233 matches that observed in the data. The standard ATLAS tool [23] is used to perform this re-weighting.  
 234 Figure 3 shows the number of primary vertex distribution in the 2016 collected DAOD\_RPVLL data com-  
 235 pared with a MC signal sample with the pileup reweighting procedure not applied, and how the agreement  
 with data is improved when it is applied on top of the MC15c pileup configuration.

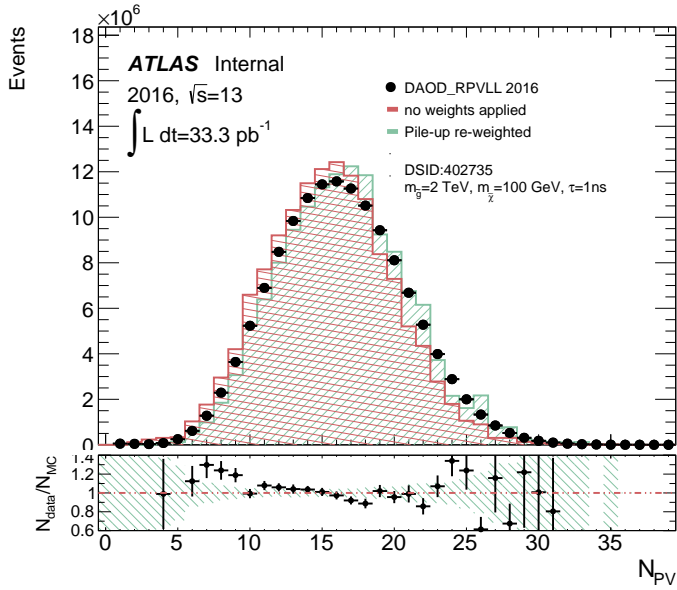


Figure 3: Number of primary vertices distributions for data (black points) and for a MC sample (red and green lines), DSID: 402735, with  $m_{\tilde{g}} = 2000$  GeV,  $m_{\tilde{\chi}^0} = 2000$  GeV, with a proper lifetime for the R-hadron of  $\tau = 1$  mm. The red line plot is showing the MC distribution without using the pileup reweighting procedure, whilst it was applied to the green line histogram, showing a better agreement with data.

Figures 4(a) and 4(b) show that removing the trackless-jet requirement and raising the threshold of MET\_LocHadTopo in the DRAW\_RPVLL filter improves the signal efficiencies of the compressed scenarios significantly. The efficiencies for the scenarios with larger mass differences are reduced, but only slightly.

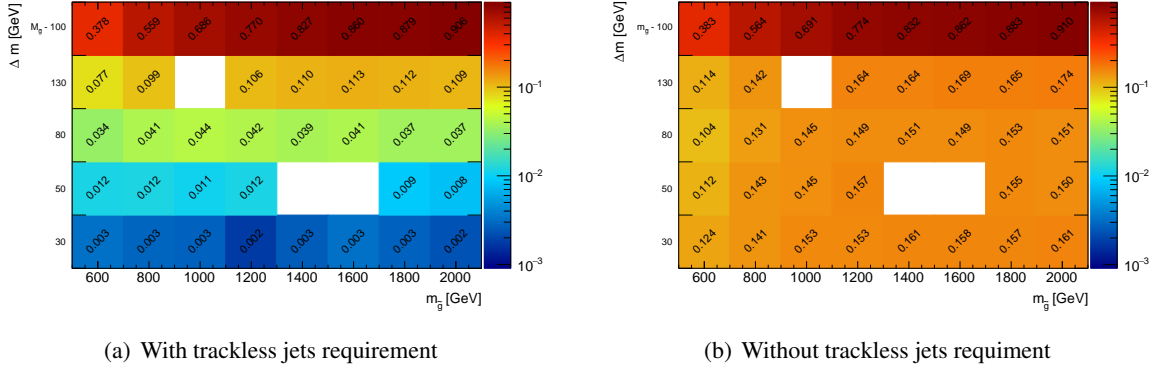


Figure 4: Efficiencies of filter and offline MET cut at 250 GeV for MC samples of R-hadrons (a) with trackless jets requirement and (b) without trackless jets requirement but the MET\_LocHadTopo threshold is raised to 180 GeV.

Not reviewed, for internal circulation only

### 2.2.2. Other Monte Carlo samples

The use of MC samples for this analysis is mainly limited by two factors:

- In order to use the Large Radius Tracking (LRT) processing described in Section 3.2.1, we need HITS-level information, which sometimes is not available for some MC samples and in the case is available, we need to reprocess the full digitization and reconstruction steps, including the LRT and vertexing. Those reprocessing are very demanding in both CPU and storage, therefore, we would be limited in the amount of events to process.
- The event passing the DRAW filter correspond to an esoteric mix of triggers, which would be hard to replicate on background MC without applying the same filtering and thereby severely limiting the available statistics.

However, there are various systematic effects which can be studied using background MC samples: it is important to verify that the LRT gives similar performance for data and MC in order to gain confidence in our estimated signal efficiency. We therefore use the simulated dijet samples listed in Table 2, for which the RAW are available. These samples were produced in Pythia 8 [22] with the NNPDF2.3LO PDF set and the min-bias tune A14 [24].

```

256 mc15_13TeV.361021.Pythia8EvtGen_A14NNPDF23LO_jetjet_JZ1W.merge.HITS.e3569_s2576_s2132
257 mc15_13TeV.361022.Pythia8EvtGen_A14NNPDF23LO_jetjet_JZ2W.merge.HITS.e3668_s2576_s2132
258 mc15_13TeV.361023.Pythia8EvtGen_A14NNPDF23LO_jetjet_JZ3W.merge.HITS.e3668_s2576_s2132
259 mc15_13TeV.361024.Pythia8EvtGen_A14NNPDF23LO_jetjet_JZ4W.merge.HITS.e3668_s2576_s2132
260 mc15_13TeV.361025.Pythia8EvtGen_A14NNPDF23LO_jetjet_JZ5W.merge.HITS.e3668_s2576_s2132
261 mc15_13TeV.361026.Pythia8EvtGen_A14NNPDF23LO_jetjet_JZ6W.merge.HITS.e3569_s2608_s2183

```

Table 2: Di-jet MC samples used to assess the systematic uncertainty on the vertex reconstruction due to the tracking reconstruction efficiency.

Name	Leading parton $p_T$ [GeV]	$\sigma$ (pb)	Filter eff.	Events generated
JZ1W	20-60	$7.8 \cdot 10^{10}$	$6.72 \cdot 10^{-4}$	2 M
JZ2W	60-160	$2.4 \cdot 10^{10}$	$3.33 \cdot 10^{-4}$	2 M
JZ3W	160-400	$2.7 \cdot 10^7$	$3.20 \cdot 10^{-4}$	8 M
JZ4W	400-800	0.255	$5.30 \cdot 10^{-4}$	8 M
JZ5W	800-1300	0.455	$9.23 \cdot 10^{-4}$	8 M
JZ6W	1300-1700	257.5	$9.40 \cdot 10^{-4}$	2 M

Not reviewed, for internal circulation only

262 **Mininum Bias samples** The data-MC comparation of tracking-related quantities have been performed  
 263 with minimum bias samples. Details of both data and simulation samples used are described in Ap-  
 264 pendix E.

265 **MadGraph MC samples** The modelling of initial-state radiation (ISR) is known to be better in Mad-  
 266 Graph than in Pythia6 which is used to generate the signal samples. The reason that MadGraph performs  
 267 better in this respect is twofold. MadGraph supports generating the additional jet as part of the matrix  
 268 element while Pythia relies on generating this from the parton shower. MadGraph is therefore used to  
 269 generate samples with gluino pair production so that the Pythia samples can be re-weighted to the im-  
 270 proved ISR performance. The reason why MadGraph is not used to simulate the main signal samples is  
 271 that it is that it cannot be interfaced with Pythia6 which hadronises the long-lived gluinos. The following  
 272 MadGraph MC samples with varying gluino masses are used:

273 mc15\_13TeV.372525.MGPy8EG\_A14N23LO\_SM\_GG\_N2\_ZN1\_400\_100\_2L.merge.AOD.e4214\_a766\_a777\_r6282  
 274 mc15\_13TeV.372526.MGPy8EG\_A14N23LO\_SM\_GG\_N2\_ZN1\_600\_100\_2L.merge.AOD.e4214\_a766\_a777\_r6282  
 275 mc15\_13TeV.372528.MGPy8EG\_A14N23LO\_SM\_GG\_N2\_ZN1\_800\_100\_2L.merge.AOD.e4214\_a766\_a777\_r6282  
 276 mc15\_13TeV.372531.MGPy8EG\_A14N23LO\_SM\_GG\_N2\_ZN1\_1000\_100\_2L.merge.AOD.e4214\_a766\_a777\_r6282  
 277 mc15\_13TeV.372535.MGPy8EG\_A14N23LO\_SM\_GG\_N2\_ZN1\_1200\_100\_2L.merge.AOD.e4214\_a766\_a777\_r6282  
 278 mc15\_13TeV.372541.MGPy8EG\_A14N23LO\_SM\_GG\_N2\_ZN1\_1400\_100\_2L.merge.AOD.e4214\_a766\_a777\_r6282  
 279 mc15\_13TeV.372547.MGPy8EG\_A14N23LO\_SM\_GG\_N2\_ZN1\_1600\_100\_2L.merge.AOD.e4214\_a766\_a777\_r6282  
 280 mc15\_13TeV.372553.MGPy8EG\_A14N23LO\_SM\_GG\_N2\_ZN1\_1800\_100\_2L.merge.AOD.e4214\_a766\_a777\_r6282

### 281 3. Event selection

- 282 The selection of events of interest with signal characteristics is performed by applying several sequential  
 283 cuts. In brief, for events passing the pre-selection described at section 3.1, we apply further offline  
 284 object requirements (Sec. 3.3) before considering the reconstructed vertices within these events. These  
 285 requirements are designed to consolidate the pre-selection filter and ensure that we are not close to any  
 286 thresholds where these cuts might have different efficiency in data and MC. They are not optimised to  
 287 maximise signal significance or background rejection as we wish to keep the search as model-independent  
 288 as possible, and it is expected that the vertex selection criteria (Sec. 3.4) will be effective at removing  
 289 essentially all background. After the criteria described there are applied, events are required to contain *at*  
 290 *least one* reconstructed DV.
- 291 The DRAW\_RPVLL filter is implemented in the analysis code and applied to signal MC, correctly taking into  
 292 account the proportions of the data processed with the two different period-dependent requirements. It is  
 293 validated by comparing the output of the DRAW\_RPVLL filters and the analysis code that these selections  
 294 are reproduced exactly.
- 295 The event selection cuts are summarised in Table 3 and described in more detail in the subsequent sub-  
 296 sections.

Table 3: Sequential cuts applied to select signal events.

<b>Skimming:</b>	
DRAW_RPVLL filter:	see description in Sec 2.1.1
SUSY15 Skimming	see description in Sec 2.1.2
<b>Analysis-level cuts:</b>	
Event pre-selection:	
Event cleaning	Rejection of bad/corrupted events (LAr, Tile, TTC restart, ...)
Good run list	Removal of bad lumi blocks based on data quality assessment
Primary vertex	At least 1 good PV, with $N_{\text{PV}}^{\text{tracks}} \geq 2$ AND $ z_{\text{PV}}  < 200$ mm
Non-collision bg veto	Reject events where the leading jet satisfy $\text{FracSamplingMax} > 0.8$    $\text{EMFrac} > 0.96$
Final event selection:	
MET Trigger:	Lowest un-prescaled: HLT_xe100_mht_L1XE50, HLT_xe110_mht_L1XE50, HLT_xe110_mht_L1XE50_AND_xe70_L1XE50
$E_T^{\text{miss}}$ cut	Offline calibrated $E_T^{\text{miss}} > 250$ GeV
DV selection	See section 3.4

297 In order to use all the available statistics, the sample passing the event pre-selection is used for the back-  
 298 ground estimation methods.

### 299 **3.1. Event pre-selection**

300 To have access to the low-level hit information needed for the Large Radius Tracking, the DRAW\_RPVLL  
 301 event stream described in Section 3.2.1 is used. This format provides full RAW event content for a tightly  
 302 skimmed subset of events, selected by the filter requirements detailed at Section 2.1.

303 The events passing the skimming criteria for the formats used in this analysis have to:

- 304 • pass the DRAW\_RPVLL skimming criteria described in Section 2.1
- 305 • pass any of the triggers defined in the derivation DAOD\_SUSY15.

306 For the MC samples, the two period-dependent DRAW\_RPVLL filters are simulated by slicing the samples  
 307 proportionally to the respective integrated luminosity of the two data periods using randomly drawn run  
 308 numbers from the PileupReweightingTool. No skimming is applied in the SUSY15 step when pro-  
 309 cessing the MC.

310 In addition to the above skimming criteria, the event pre-selection also includes several cleaning cuts that  
 311 reject events affected by detector problems:

312 Following the standard ATLAS recommendations from Data Preparation [25, 26], we veto events that  
 313 are:

- 314 • affected by LAr noise bursts and/or data corruption
- 315 • affected by corruption of the Tile data
- 316 • affected by non-operational cells in the Tile and Hadronic End Cap (HEC) calorimeters
- 317 • affected by the recovery procedure for single event upsets in the SCT

318 Events in luminosity blocks not included in the Good Runs List (see Section 2.1) are also rejected from  
 319 the analysis. The events are required to contain at least one good Primary Vertex (PV) with at least two  
 320 tracks, and  $z$  position  $|z_{PV}| < 200$  mm. When several such vertices are available, the one with the largest  
 321  $\sum(p_T^{\text{trk}})^2$  is chosen as the selected PV.

322 When studying the  $\phi$  distribution of the  $E_T^{\text{miss}}$  for the events passing our selection, it became clear that  
 323 there was a significant contribution from non-collision background processes (e.g. beam halo). To reject  
 324 these events at an early stage of the analysis, all events used in this analysis are also required to pass  
 325 cleaning cuts designed specifically for this analysis, described and motivated in detail in the following  
 326 subsection.

327 Events passing the requirements described above are said to pass the "event pre-selection".

328 **3.1.1. Non-collision background**

329 When studying the  $\phi$  distribution of the  $E_T^{\text{miss}}$  for the events passing our selection, it became clear that  
 330 there is a significant contribution from non-collision background processes (e.g. beam halo). Figure  
 331 5 shows this distribution, on the left for three different selections on the full (blinded) dataset: all  
 332 events passing the DRAW+SUSY15 selection, all events passing the event-level selection including the  
 333  $E_T^{\text{miss}} > 250$  GeV cut, and after also requiring a good DV passing all but the  $n_{\text{tracks}}$  and  $m_{\text{DV}}$  cuts. On the  
 334 right the last distribution is split up for periods A-J and K-L showing that both periods are significantly  
 335 contaminated, i.e. both of the two DRAW filters that were used for the processing of the data for the two  
 336 periods select non-collision background events.

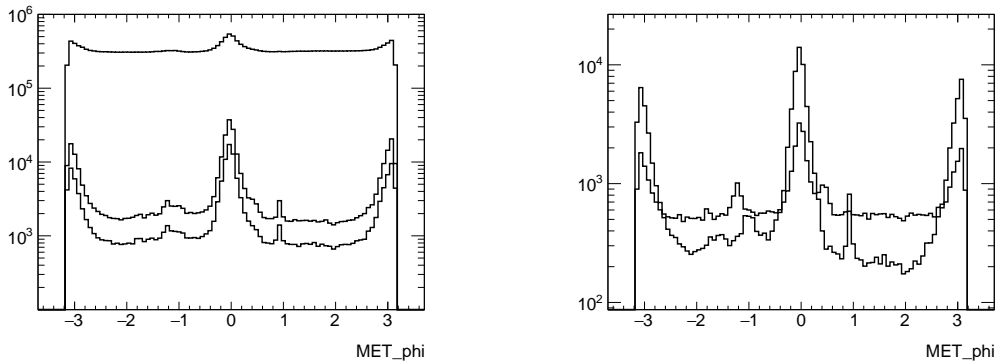


Figure 5: Distributions of the  $\phi$  of the  $E_T^{\text{miss}}$  for the data. Left: all events passing the DRAW+SUSY15 selection, all events passing the event-level selection including the  $E_T^{\text{miss}} > 250$  GeV cut, and after also requiring a good DV passing all but the  $n_{\text{tracks}}$  and  $m_{\text{DV}}$  cuts. Right: the events passing the last selection on the left but separated for periods A-J (larger yield) and K-L (smaller yield).

337 The event selection does not require any hard physics object associated to the PV, and this means the  
 338 search is more sensitive to contamination of non-collision background events. Studying many of the vari-  
 339 ables commonly used for jet cleaning, a few have been identified that efficiently discriminate the events in  
 340 the peaks around  $\phi = 0$  and  $\phi = \pm\pi$  (from non-collision background processes) from the events not con-  
 341 tamated by non-collision processes. In particular, requiring that the leading jet has `FracSamplingMax`  
 342  $< 0.7$  the peaks are dramatically reduced as can be seen for one significantly affected run in Figure 6. The  
 343 variable `FracSamplingMax` is the highest fraction of the energy in a jet deposited in a single sampling,  
 344 i.e. calorimeter layer. The leading jet is simply the highest- $p_T$  `AntiKt4EMTopo` jet after calibration,  
 345 without any other requirements imposed.

346 This analysis vetoes events where the leading jet satisfies either of these criteria:

- 347 • `FracSamplingMax`  $> 0.8$
- 348 • `EMFrac`  $> 0.96$

349 Figure 7 shows the two-dimensional distributions for these variables for data (a) and an example signal  
 350 MC sample (b). In summary, studies on a subset of the data and a representative set of signal MC samples  
 351 indicate that the cuts above reject 90% of the data in the  $\phi$  peaks (i.e. almost all NCB) while rejecting  
 352  $< 1\%$  of the signal events. Applying this cut requires processing all of the derivations again, and this  
 353 will happen during the next days. It needs to be studied if the significantly lower data event yields (about

Not reviewed, for internal circulation only

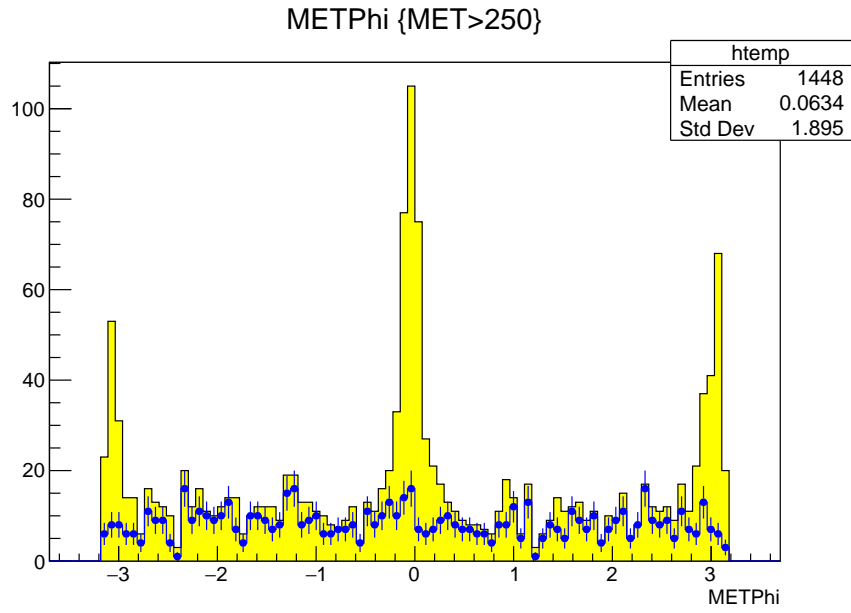


Figure 6: The  $\phi$  distribution of the  $E_T^{\text{miss}}$  for one run significantly contaminated by non-collision background before (yellow histogram) and after (blue markers) requiring  $\text{FracSamplingMax} < 0.7$  for the leading jet.

354 50% are in the  $\phi$  peaks) will cause low statistics in some detector regions for the data-driven background  
 355 estimation method.

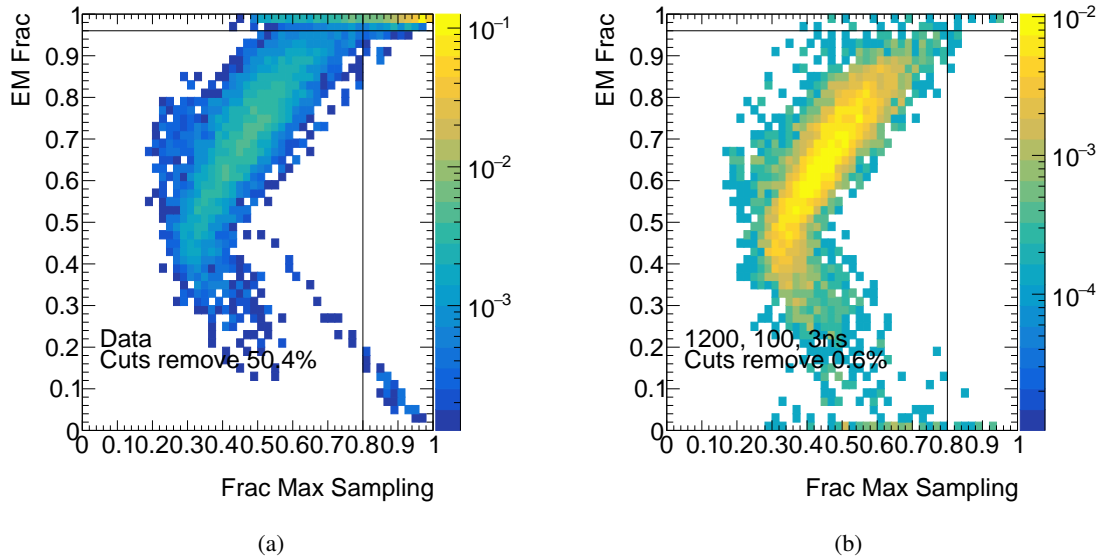


Figure 7: Two-dimensional distributions for the two variables proposed to use for the NCB veto, for (a) data and (b) an example signal MC sample.

356 Figure 8 shows the azimuthal  $E_T^{\text{miss}}$  angle for events before and after the NCB veto described above. This

357 is shown with and without an additional requirement that events have a displaced vertex with at least 3  
 358 tracks, showing that the final contribution of NCB on the analysis is minimal after the explicit veto. The  
 359 timing distributions for the leading jets in these events is similarly shown in Figure 9.

Not reviewed, for internal circulation only

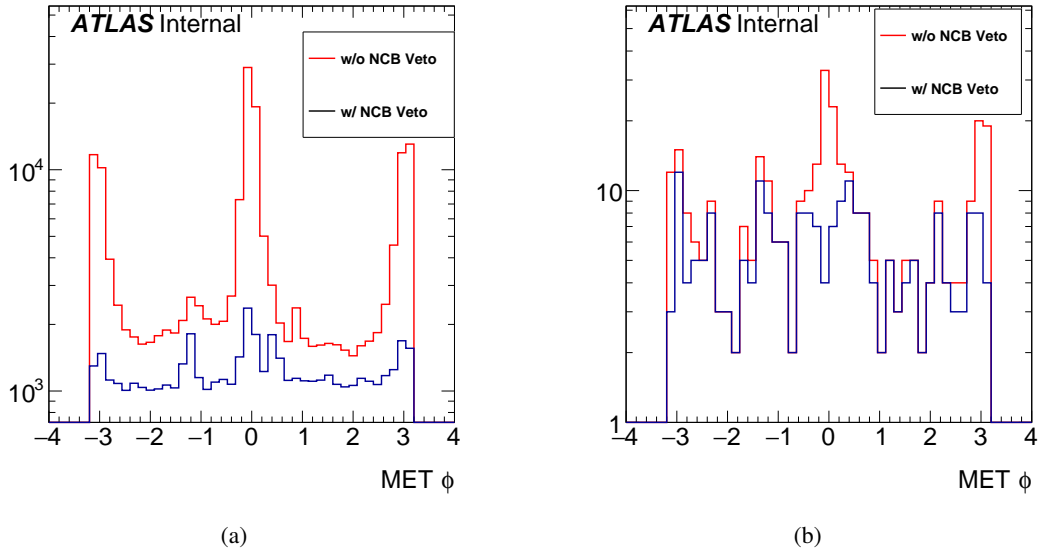


Figure 8: The  $E_T^{\text{miss}} \phi$  distributions for events with and without the NCB veto described in the text applied to (a) a blinded event selection and (b) the same selection but also requiring the presence of a vertex with at least three tracks (right).

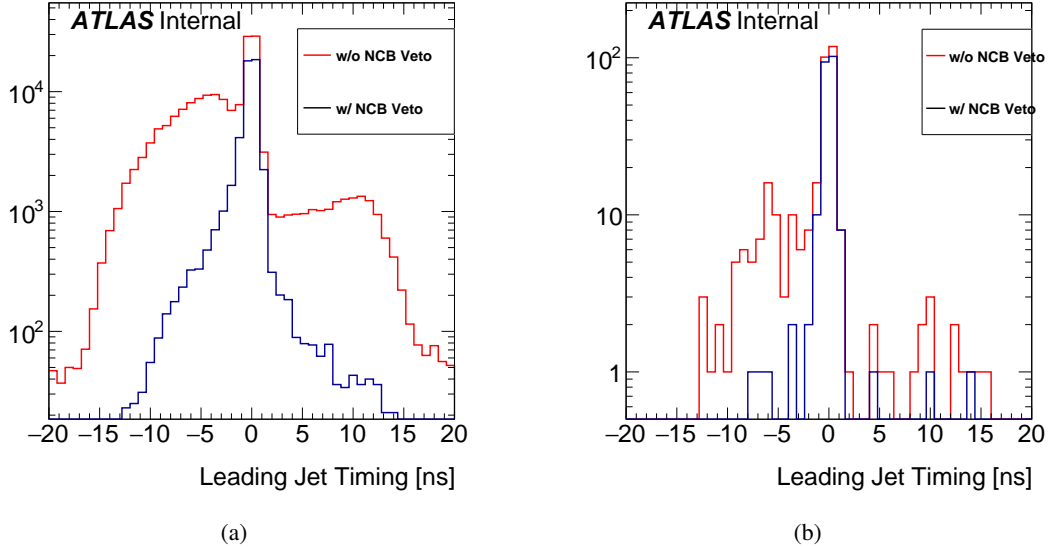


Figure 9: The leading-jet time distributions are shown for event selections with and without the NCB veto described in the text for (a) a blinded event selection and (b) the same selection but requiring also the presence of a vertex with at least three tracks.

360 While these figures show that an additional requirement on the leading-jet time will have a minimal effect  
 361 on the residual NCB, an important consideration is that the signals considered here do not have leading  
 362 jets with timing near 0 ns unlike prompt jet production. This is shown in Figure 10 for several signals  
 363 with varying  $R$ -hadron lifetimes. It's clear from these distributions that a veto on events with leading-jet  
 364 time far away from zero can have a detrimental effect on long-lived signal acceptances.

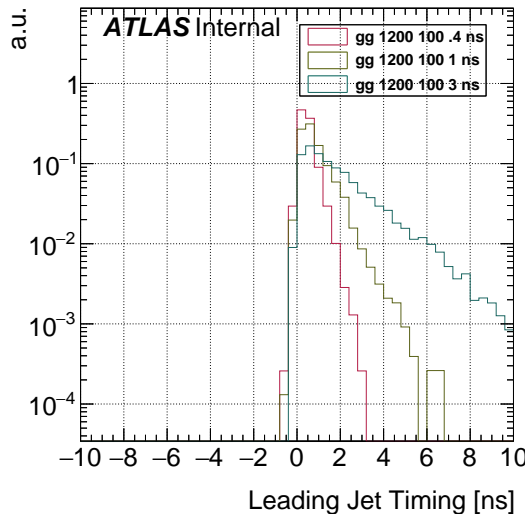


Figure 10: Distribution of leading-jet time with varying  $R$ -hadron lifetime for simulated signal samples.

### 365 3.2. Special reconstruction

366 The final event selection for the analysis requires selections involving the output from special recon-  
 367 struction algorithms. This subsection describes the special track and vertex reconstruction used in this  
 368 analysis.

#### 369 3.2.1. Tracking

370 In common with previous iterations of this analysis, we process the data and MC using special tracking  
 371 now called *Large Radius Tracking* (LRT) [27]: a specialised third-pass tracking for LRT tracks , after the  
 372 two standard inside-out (first) and outside-in (second) passes [28]. The third-pass tracking is based on a  
 373 standard inside-out sequence where the hits used to seed and construct the tracks are the leftovers of the  
 374 previous passes. Some modifications in the algorithm cuts allow to increase the efficiency for high radius  
 375 tracks, without including too many fakes. The main differences with respect to the standard sequence are  
 376 that:

- 377 • the allowed region to search hits used for seeding is extended slightly compared to the standard  
 378 tracking,
- 379 • the requirements on the transverse and longitudinal impact parameters are loosened,
- 380 • some quality cuts (mainly related to hit multiplicities in the various tracking detectors) are re-tuned.

381 Note that tracks from standard tracking and those found by re-tracking are added to the same `TrackParticle`  
 382 collection (`InDetTrackParticles`). The cuts applied in the standard ATLAS tracking algorithms (Si-  
 383 seeded and TRT-seeded) and in the LRT processing are listed in Table 4. The LRT performance and  
 384 validation plots are available in Appendix E (and a special document is also in preparation by the LRT  
 385 group).

Table 4: Cuts applied in the different tracking algorithms.

cut	Si-seeded	TRT-seeded	high- $d_0$ tracking
max $d_0$	10 mm	100 mm	300 mm
max $z_0$	250 mm	-	1500 mm
min $p_t$	400 MeV	2 GeV	500 MeV
min Pix hits	0	-	0
min Si hits	7	4	7
min TRT hits	9*	15	9*
min NOT Shared	6	4	5
max Shared	1	1	2
max Si Holes	2	2	2
max Pixel Holes	1	2	1
max SCT Holes	2	2	2
max Double Holes	1	1	1

\* on track extension

### 386 3.2.2. Reconstruction of secondary vertices

387 In Run 1, two packages existed for vertexing after re-tracking, and they were both based on the same  
 388 algorithm described below. These were `RPVDispVrt` for the beyond-SM long-lived particle searches [2,  
 389 3, 5–11] and `VrtSecInclusive` which was used for the inner detector material measurement [29]. The  
 390 `VrtSecInclusive` package was updated to use the xAOD EDM for the Run 2 inner detector material  
 391 measurement [30, 31], and it was therefore decided to use this package also for the new physics searches  
 392 in Run 2.

393 Following this strategy, the inner detector volume is segmented into several regions defined by major  
 394 structures, and different hit requirements are applied as summarised in Table 4.

395 The input to this algorithm is a list of `TrackParticles` found by standard tracking and Large Radius  
 396 Tracking, and with the following additional requirements imposed:

- 397 •  $\geq 2$  SCT hits
- 398 • Transverse momentum  $p_T > 1$  GeV
- 399 • Transverse impact parameter  $|d_0| > 2$  mm
- 400 • Tracks are rejected if they have fewer than two Pixel hits *and* no TRT hits. This requirement is  
 401 effective at removing fake tracks made up of hits in the SCT endcaps.

Not reviewed, for internal circulation only

402 The algorithm first makes a set of two-track “seed” vertices which satisfy  $\chi^2/N_{\text{dof}} < 5$ , using the *in-*  
 403 *compatibility graph* method [32]. For these seed vertices, a fake-vertex rejection depending on the vertex  
 404 position is applied by requiring certain hit patterns in the Pixels and SCT for tracks forming the vertex.  
 405 The hit patterns are required to be consistent with the assumption that daughter particles fly from inner to  
 406 outer radii. Figure 11(a) illustrates the fake-tracks rejection scheme. The tracks forming the vertex must  
 407 not have hits in the layers at smaller radii than the vertex, and the tracks are required also to have a hit  
 408 in the first layer outside the vertex position in the radial direction (defined as the distance of the vertex in  
 409 the  $x$ - $y$  plane from the origin of the ATLAS coordinate system). If the vertex position is inside a layer  
 410 or within several millimetre’s (depending on the layer) of one of the layers, hits are required on the next  
 411 outer layer, but hits are neither forbidden nor required for the inner layer (Figure 11(b)).  
 412 Because of the required-hit and forbidden-hit criteria placed on the tracks composing a candidate vertex,  
 413 the fake-rejection scheme can over-zealously veto vertices reconstructed directly in front of pixel modules  
 414 (i.e. at lower radius) that have been disabled for a significant portion of the dataset as the algorithm  
 415 performing the cleaning is unaware of the detector data quality. Because of this, regions directly in  
 416 front of pixel modules that have been disabled for any portion of the 2016 dataset are explicitly vetoed  
 417 in order to properly account for this effect in any simulation used. The signal acceptance would be  
 418 calculated incorrectly if this effect in the data would not be properly modelled in the simulation. This  
 419 very conservative treatment should completely mitigate the problem at the price of only a few percent  
 420 reduced overall signal acceptance. The overall volume vetoed by this procedure is 3,960 cm<sup>3</sup> out of a  
 421 total fiducial volume of 169,645 cm<sup>3</sup>, effectively vetoing 2.3% of the fiducial volume.

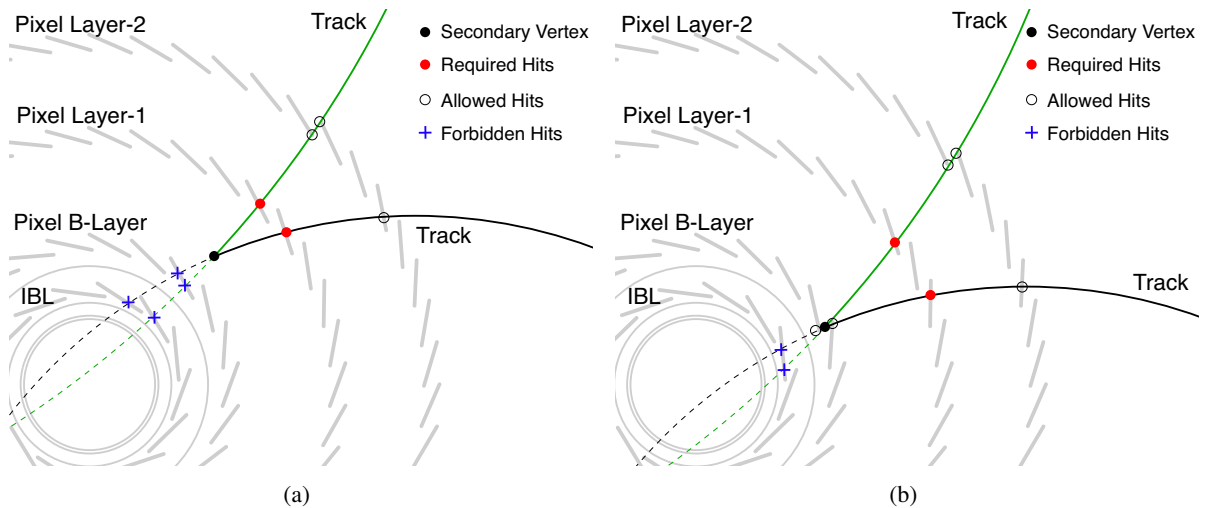


Figure 11: Schematic illustration of fake tracks rejection. (a) The vertex is between the two layers of B-Layer and Layer-1 sensors. The tracks of the reconstructed secondary vertex must not have hits on the layers inner than the vertex radius (i.e. IBL and B-Layer), and must have hits on the closest layer outside the vertex (i.e. Layer-1). (b) The vertex is close to the Pixel B-Layer sensors. In this example where the vertex is just inside the B-Layer, the tracks are not allowed to have hits on the IBL but may have hits on the B-Layer, and must have hits on the Layer-1. Analogous requirements are made on vertices close to the other layers.

422 The incompatibility graph is then applied again in order to use the surviving seed vertices to create all  
 423 possible  $N$ -track vertices. At this point it is possible that the same track is used in more than one vertex.  
 424 An iterative “clean-up” algorithm is therefore applied as follows:

- 425 1. For all tracks that are used in more than one vertex, the vertex+track combination with the largest  
426  $\chi^2$  is found.
- 427 2. If this  $\chi^2$  is greater than 6, or the two vertices are separated by more than  $3\sigma$  (according to the  
428 uncertainties on their fitted positions), the track is removed from that vertex.
- 429 3. Otherwise, the two vertices are merged and refit.
- 430 4. Return to step 1.
- 431 5. Once the process has converged such that there are no tracks shared between vertices, a final merging  
432 step is performed where pairs of vertices separated by less than 1 mm are merged, and the  
433 combined vertex is refit.

### 434 3.3. Final event selection

435 On top of the event pre-selection criteria discussed in Section 3.1, the final event selection requires a  
436 large amount of missing transverse momentum. We use the recommended final calibrated offline  $E_T^{\text{miss}}$ ,  
437 calculated with the METMaker tool using calibrated jets, leptons and photons as input. Figure 12 shows  
438 the efficiencies of passing the  $E_T^{\text{miss}}$  trigger and the MET\_LocHadTopo requirement as a function of final  
439 offline  $E_T^{\text{miss}}$ . To not rely on the modeling of the turn-on curves in the MC, the final event selection  
440 requires final offline  $E_T^{\text{miss}} > 250$  GeV, in order to be in the plateau of the turn-on curves. Figure 13  
441 shows the efficiency for passing both the trigger and the MET\_LocHadTopo requirements as a function of  
442 offline  $E_T^{\text{miss}}$ , and the turn-on curves for MET\_LocHadTopo requirements with various threshold values.  
443 In principle, different  $E_T^{\text{miss}}$  cuts could be used depending the DRAW\_RPVLL filter and trigger used during  
444 the various data-taking periods in order to gain sensitivity for low- $E_T^{\text{miss}}$  signal scenarios. However we  
445 choose to keep the same value regardless the data-taking period in order to simplify the event selection.  
446 The loss in signal efficiency due to this choice is tiny (see details in Appendix C).

### 447 3.4. Vertex selection

448 Reconstructed vertices found by the algorithm described above have the following selection requirements  
449 applied in turn:

- 450 • The vertex position should be in the fiducial volume  $r_{\text{DV}} < 300$  mm and  $|z_{\text{DV}}| < 300$  mm.
- 451 • The vertex fit should have  $\chi^2/d.o.f. < 5$ .
- 452 • The vertex should be separated by at least 4mm in the  $(x, y)$  plane from all reconstructed primary  
453 vertices in the event.
- 454 • The vertex should not be in a region of dense material, as defined by the material map described in  
455 Section 3.5.
- 456 • The **Signal Region** for vertex candidates is then defined as  $N_{\text{trk}} \geq 5$ , and  $m_{\text{DV}} > 10$  GeV (where  
457  $m_{\text{DV}}$  is the invariant mass of the vertex calculated using the charged pion mass hypothesis for  
458 the tracks, i.e. instead of assuming massless tracks when calculating the invariant mass of the  
459 combination, it is assumed that all tracks have the mass of a charged pion).

Not reviewed, for internal circulation only

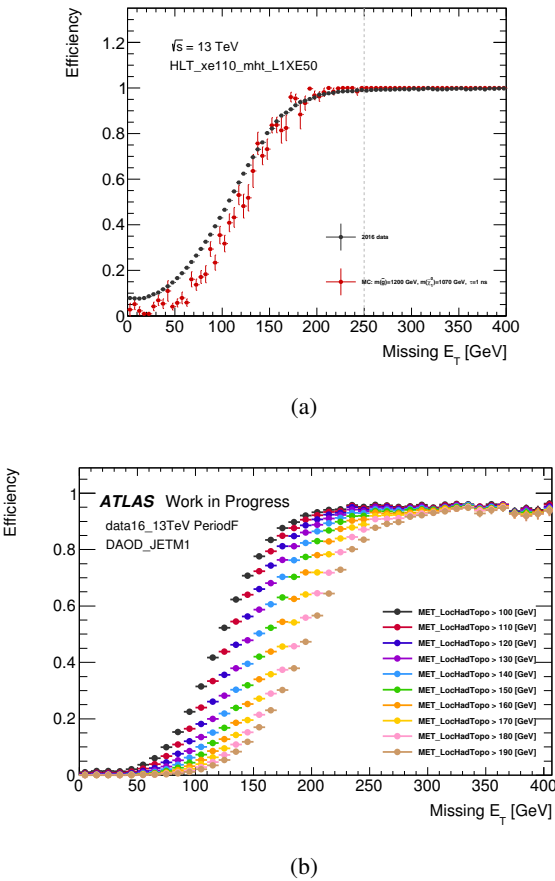


Figure 12: (a) Turn-on curve of HLT\_xe110\_mht\_L1XE50 trigger in MC signal and 2016 data from Period F. (b) Turn-on curve of the MET\_LocHadTopo cut.

460 Note that the analysis is agnostic regarding whether the vertex comes from the decay of a charged or  
 461 neutral particle. Firstly, if the decay occurs before the first pixel layer, or indeed anywhere inside the third  
 462 pixel layer, there is no way of telling if the particle was charged or neutral as no track from the primary  
 463 vertex to the DV could be reconstructed. Secondly, although the first stage of the vertexing algorithm  
 464 rejects “seed” vertices if either of their tracks have silicon hits “inside” the vertex radial position, it  
 465 should be noted that the tracks here are required to have  $|d_0| > 2 \text{ mm}$ , so the track of a charged LLP  
 466 would not be considered by this cut.

467 The full selection described above is referred to as the “FULL” vertex selection. Removing the signal  
 468 region-like vertex requirements  $N_{\text{trk}} \geq 5$  and  $m_{\text{DV}} > 10 \text{ GeV}$  defines the “BASE” vertex selection.

### 469 3.5. Material map

470 Nuclear interactions with the material in the inner detector are the largest source of background vertices  
 471 with high track multiplicities. Distinguishing this type of background vertices from displaced decays of  
 472 long-lived particles is challenging. Any vertex found in the volume of the detector occupied by dense

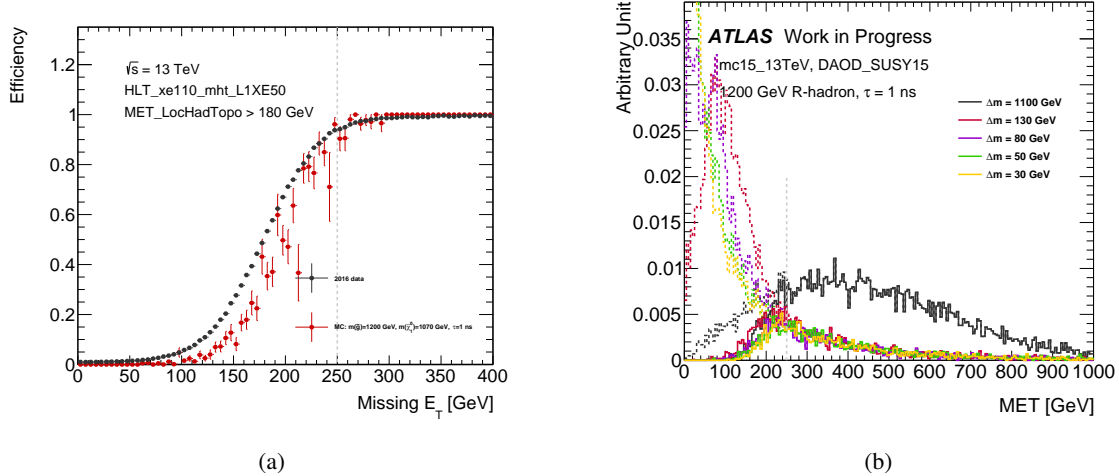


Figure 13: (a) Turn-on curve of efficiency for events passing the xe110 2016 triggers and MET\_LocHadTopo > 180 GeV cut in some MC signal and 2016 data of Period F. (b) Normalized MET distributions of a few selected MC signals. The dashed lines shows the  $E_T^{\text{miss}}$  distributions before any selections and solid lines show the  $E_T^{\text{miss}}$  spectra after requiring trigger and MET\_LocHadTopo > 180 GeV.

material therefore needs to be vetoed. A scheme to perform the veto is to construct a simplified map of these detector regions. In previous iterations of this analysis [9–11], a three-dimensional map was constructed and used as a map to veto material interaction vertices. A three-dimensional map of the material vetoes as little as possible of the total fiducial volume, thereby retaining as much as possible of the signal acceptance. The map covers the whole fiducial volume of  $r < 300 \text{ mm}$ ,  $|z| < 300 \text{ mm}$  and in the full  $2\pi$  in  $\phi$ . This is an extension of the radial region as the old two-dimensional map only covered  $r < 180 \text{ mm}$ .

There are two methods used in the construction of the different parts of the map. The more complex structures of e.g. the pixel modules are extracted from vertices reconstructed in minimum bias data<sup>2</sup>, whilst geometrical approximations are made for the more uniform shapes such as support rings.

These non-data-driven support masks have the caveat that while the beam pipe is coupled to the LHC ring, the majority of ATLAS is coupled to the floor of the experimental cavern. As a result of the excavation, the floor of the cavern is slowly rising with respect to the LHC at a small but significant rate. As a result, the material veto must account for this offset when approximating the position of the beam pipe, for example. The position of these approximations have then been validated in the 2016 dataset to ensure their positions are appropriate for the analysis described in this note. The exact positions of the geometry augmented by this effect can be found in Table 5.

It should be noted that the material map is not perfect. Even if it were, there would be a chance that vertices arising from hadronic interactions with material in a vetoed region could be reconstructed in the wrong location and survive the veto. However, as a cut, it is effective in drastically reducing high-track-multiplicity background vertices, and the same veto is used in the background estimation method, so any vertices that survive will be accounted for in the background estimation.

<sup>2</sup> A mass veto is applied to remove  $\gamma$ -conversions and  $K_S^0$  vertices.

Not reviewed, for internal circulation only

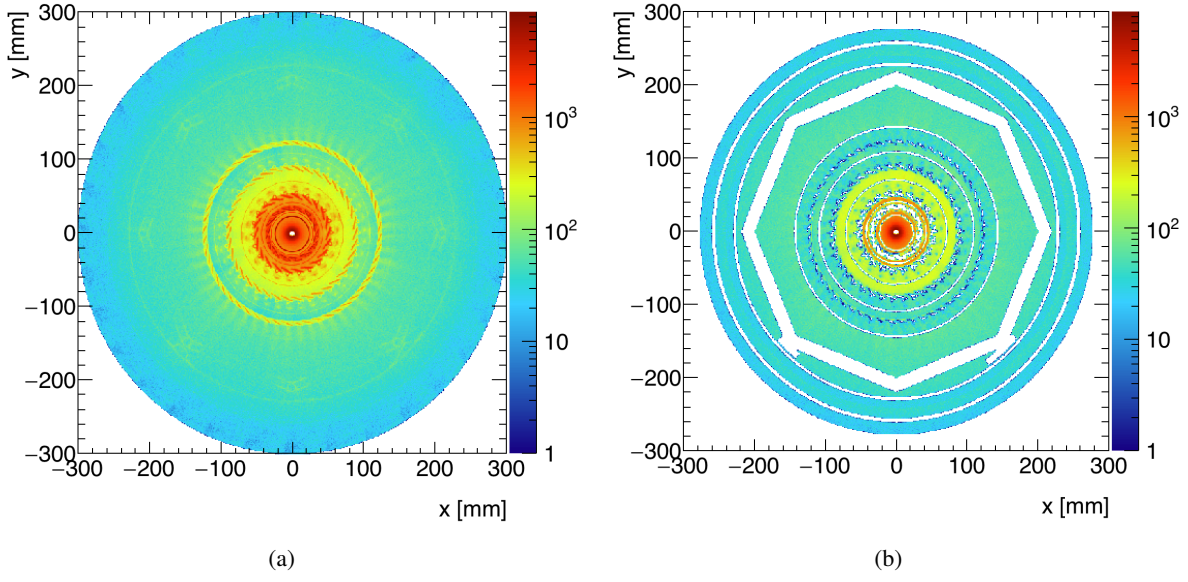


Figure 14: Two-dimensional maps of the number of vertices in the 2016 DAOD\_SUSY15 data (a) before material veto and (b) after veto.

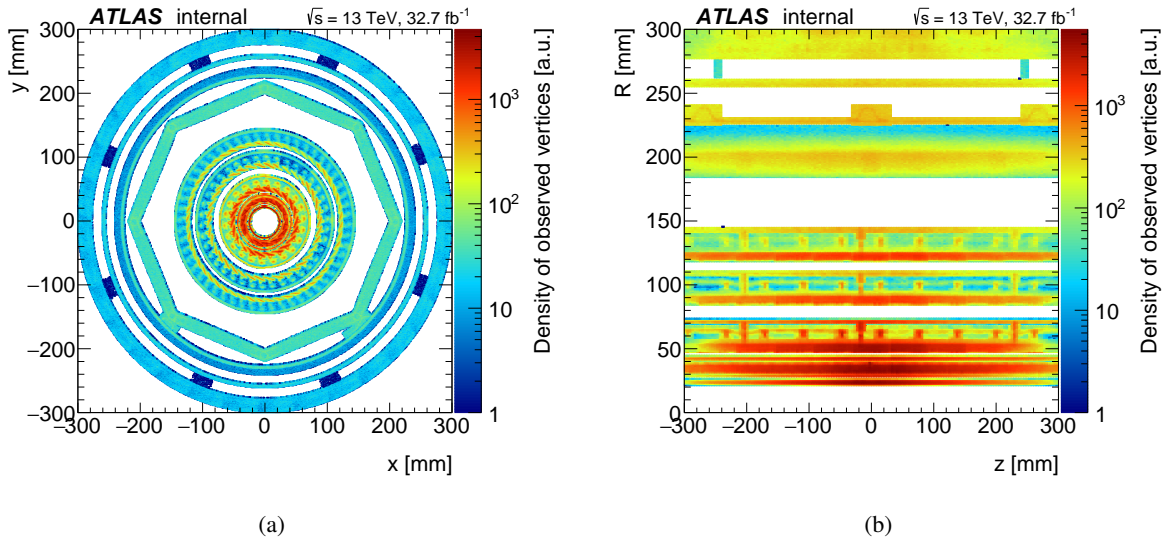


Figure 15: Validation of the new material map. Two-dimensional maps of the number of vertices which do not pass the material veto, projected in the (a)  $x$ - $y$  plane and (b)  $r$ - $z$  plane.

Table 5: Approximations of uniform shapes augmented by the offsets created by the decoupling of the beam pipe from the ATLAS cavern.

Material layer	Radius	Thickness	$x$ offset	$y$ offset
Beam pipe	24 mm	3 mm	0 mm	-1.5 mm
Pixel support 1	29 mm	1.6 mm	-0.3 mm	-0.5 mm
Pixel support 2	42.5 mm	2.4 mm	-0.2 mm	-1 mm
Pixel support 3	68.5 mm	4.5 mm	-0.1 mm	-0.5 mm

495 The volume vetoed by the material map is 42% of our fiducial volume ( $\pi r^2 z \simeq 3.14 \cdot 300^2 \cdot 600 \text{ mm}^3$ ) in  
 496 total.

## 4. Selection efficiency

### 4.1. Event and vertex yields

Figure 16 shows event and vertex yields at the various selection stages for a signal MC sample with decaying 1200 GeV gluino  $R$ -hadrons and a 100 GeV neutralino (DSID 402074). The corresponding yield numbers for data can be seen in Table 6. Appendix B contains similar yield tables for 1200 GeV gluino  $R$ -hadron samples with neutralino masses ranging from 100 GeV to 1170 GeV. It can be seen that after the material veto cut, around a 50%<sup>3</sup> of the remaining signal vertices survive, due to the fact that a significant fraction of the fiducial volume is vetoed. Because of the exponential lifetime distribution, many decays happen at a small radial distance from the primary vertex where there is little or no material.

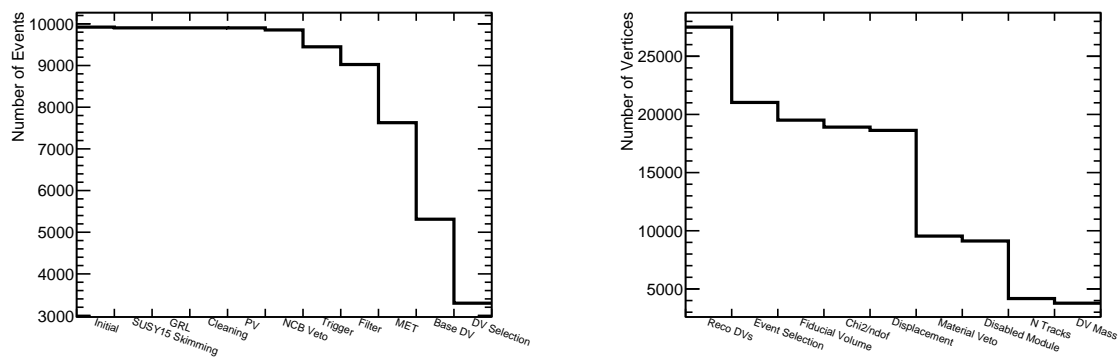


Figure 16: Cut flow for a signal scenario with 1200 GeV gluino with the lifetime of 1 ns, and 100 GeV neutralino. Left plot is showing the event selection cut flow, while the plot on the right contains the details of the vertex selection, which corresponds to the transition from the “MET cut” to “DV selection” bin of the left plot, times the number of vertices per event.

Figure 17 shows the final acceptance times efficiency ( $\mathcal{A} \times \epsilon$ ) for many of the signal samples used in this search, and scaled by their cross sections to the luminosity of the data to show their expected yields.

### 4.2. Vertex reconstruction efficiency as a function of radial position

Right plot on Figure 19 shows the vertex reconstruction efficiency (defined as the number of truth-matched reconstructed vertices, divided by the number of true signal vertices) vs radial position  $r_{\text{DV}}$ , for the  $R$ -hadron samples. In common with all efficiency-vs- $r_{\text{DV}}$  plots that will be shown in this note, three notable features are apparent:

- There are drops in efficiency at radial distances roughly corresponding to the Pixel barrel layers. The lower efficiency here is as a result of the *maximum shared hits* requirement: tracks from DVs very close to the silicon sensors are likely to have hits shared between more than one track, and will therefore fail the maximum number of shared hit cut. A detailed study of this effect can be found in the previous note [3], appendix G.

<sup>3</sup> In average, it depends on the masses and lifetimes of the model.

Not reviewed, for internal circulation only

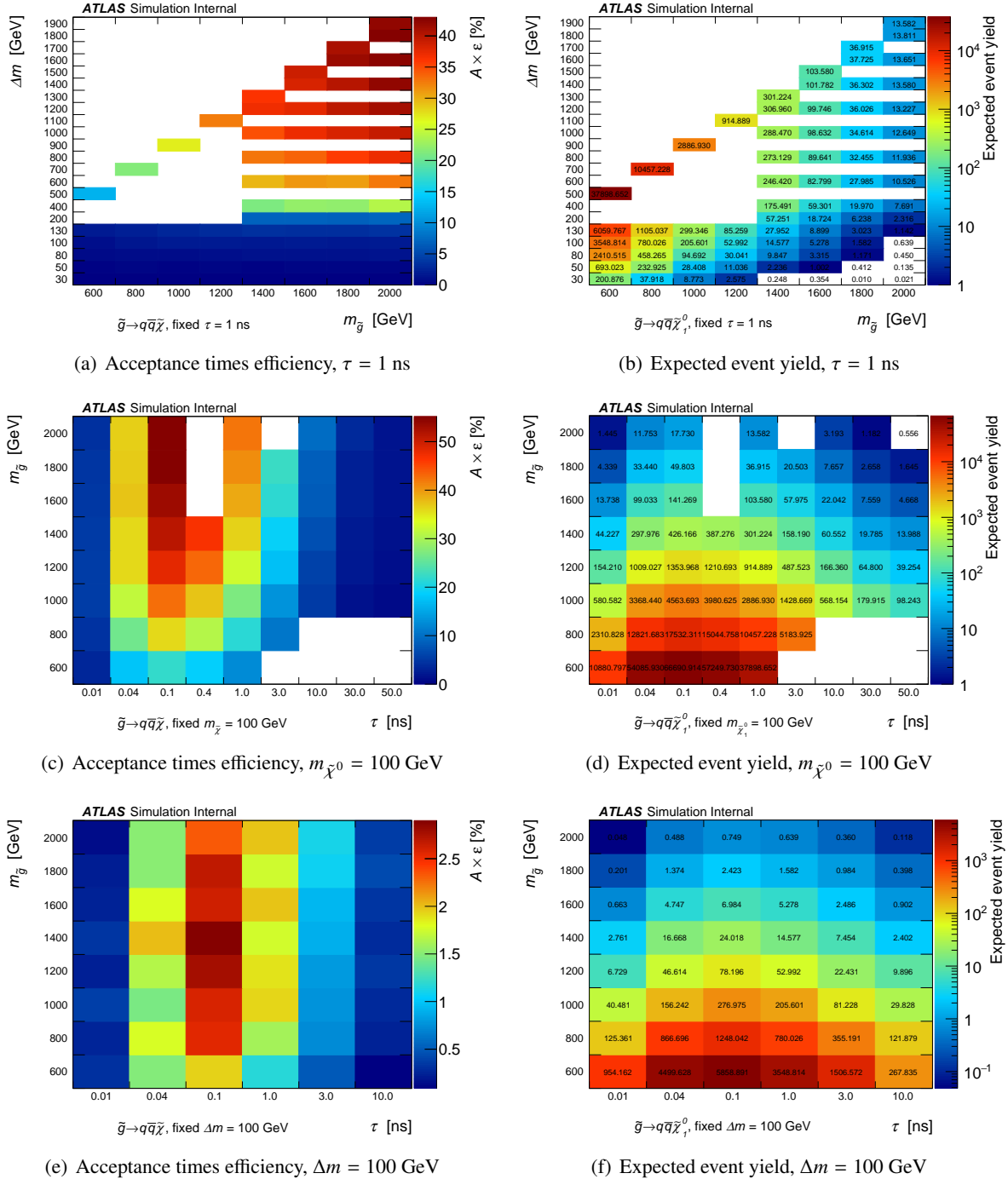


Figure 17: Acceptance times efficiency (left) and expected yields (right) for many signal scenarios. The rows show planes with fixed parameter values in our sample grid,  $\tau = 1 \text{ ns}$  (top),  $m_{\tilde{\chi}^0} = 100 \text{ GeV}$  (middle),  $\Delta m = 100 \text{ GeV}$  (bottom).

Table 6: Cut flow table for 2016 data of the DAOD\_SUSY15 stream for DV+ $E_T^{\text{miss}}$  channel.

Event Selection Cuts			
	Number of Events	Relative Efficiency [%]	Overall Efficiency [%]
Initial Events	75439504	100	100
SUSY15 Skimming	75439504	100.0	100.0
Good Runs List	73374312	97.3	97.3
Event cleaning	73019704	99.5	96.8
Primary vertex	73018496	100.0	96.8
NCB veto	47801448	65.5	63.4
MET Trigger	28580256	59.8	37.9
MET Filter	2855625	10.0	3.8
Offline MET cut	294614	10.3	0.39
Base DV selection	45734	15.5	$6.1 \cdot 10^{-2}$
Full DV selection	0	0.0	0.0
Vertex Selection Cuts			
	Number of DVs	Relative Efficiency [%]	Overall Efficiency [%]
Reco DVs	41243944	100	100
Event cuts	154140	0.37	0.37
Fiducial acceptance	130087	84.4	0.32
DV displacement	129886	99.8	0.31
Fit quality	128491	98.9	0.31
Material veto	53621	41.7	0.13
Disabled module	51876	96.7	0.13
DV nTrk	6	$1.2 \cdot 10^{-2}$	$1.5 \cdot 10^{-5}$
DV mass	0	0.0	0.0

- 518 • There is also an overall decrease in efficiency as a function of  $r_{\text{DV}}$  which is due to the tracking  
 519 efficiency decreasing as a function of  $r_{\text{DV}}$ , as it can be observed in Figure 18.  
 520 • For the scenarios with a lighter neutralino, the efficiency is lower at small radii, as many of the  
 521 tracks have a small angle with respect to the neutralino flight direction, and therefore fail the  $|d_0| >$   
 522  $2\text{mm}$  cut.

523 In short, many of the features we observe in vertex reconstruction efficiency as a function of vertex radius  
 524 are non-trivial combinations of different aspects of the track reconstruction efficiency. Figure 18 shows  
 525 the  $r_{\text{DV}}$  dependence of track-finding efficiency, whilst the right plot on Figure 19 illustrates the gain we  
 526 get from the LRT processing, showing the efficiency after the event-related cuts with LRT processing and  
 527 with standard processing.

### 528 4.3. Reweighting efficiencies for intermediate lifetimes

529 Our signal MC samples listed from Tables 11 to 17 have fixed values for the average lifetime  $\tau$  of the  
 530 long-lived particle. In order to evaluate the efficiency for any value of  $\tau$ , a simple re-weighting strategy is  
 531 employed. Each event that passes the selection cuts (i.e. event-level cuts and at least one DV passing all  
 532 selection criteria) is re-weighted by the probability that both true long-lived particles would decay where  
 533 they did. Moreover, a correction factor obtained from the probability that the decay is produced inside  
 534 the fiducial region of this analysis, i.e.,  $r_{fr} < 300\text{ mm}$  and  $|z_{fr}| < 300\text{ mm}$ , is also applied to take into

Not reviewed, for internal circulation only

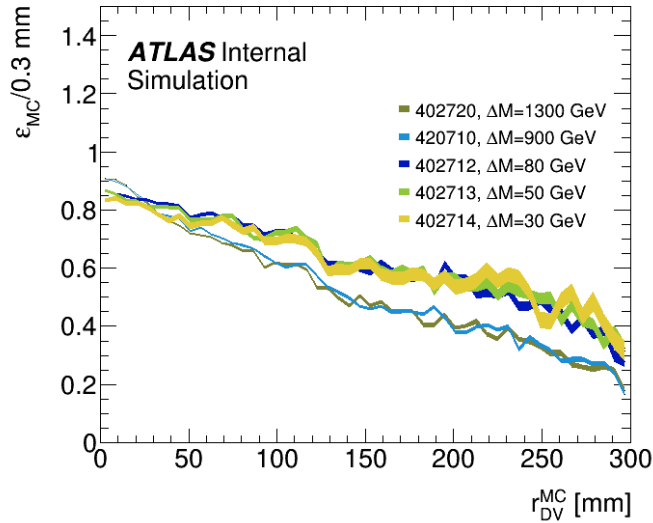


Figure 18: Tracking reconstruction efficiency vs.  $r_{DV}$  for several  $m_{\tilde{g}} = 1200 \text{ GeV}$   $R$ -hadron signal samples.

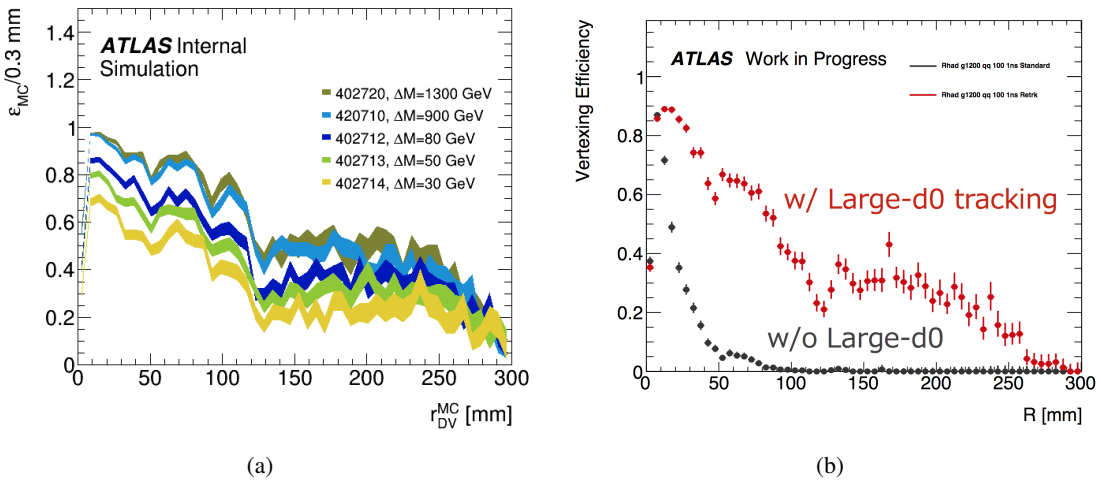


Figure 19: (a) Vertex reconstruction efficiency vs  $r_{DV}$ , using several  $m_{\tilde{g}} = 1200 \text{ GeV}$   $R$ -hadron signal samples, and (b) with and without LRT processing, after the event-related cuts. Both plots describe the number of reconstructed vertices matched with a true signal vertex.

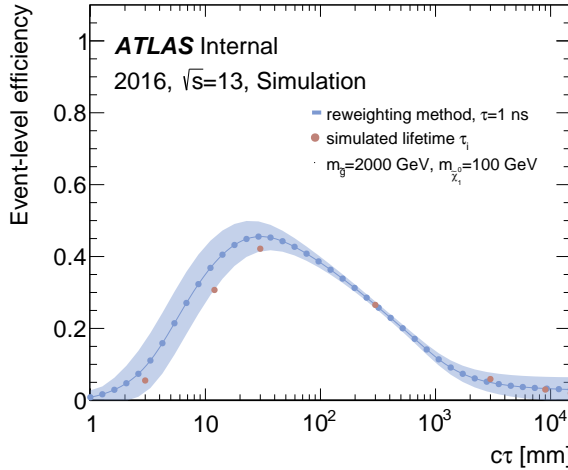


Figure 20: Closure test for the efficiency re-weighting procedure. A sample generated with  $\tau = 1$  ns ( $c\tau \approx 300$  mm) is re-weighted to give the blue curve (statistical uncertainty considered only). This is compared with several samples with the same mass spectrum but generated at different  $\tau = 0.01, 0.04, 0.1, 1, 10, 30$  and  $50$  ns, (corresponding to  $c\tau = 3.0, 12.0, 30.0, 300, 3000, 9000$  and  $15000$  mm), which are represented as the red points. The figure shows closure to within statistical uncertainty in all the points considered.

535 account effects on limited statistics (see Appendix I). The weight assigned for a given value of the average  
 536 lifetime in our MC sample  $\tau_{MC}$  (as listed from Table 11 to 17) and given true decay lifetimes  $t_1^{\text{true}}$  and  
 537  $t_2^{\text{true}}$  is,

$$w(t_1^{\text{true}}, t_2^{\text{true}}) = \left( \frac{\tau_{MC}}{\tau_{\text{goal}}} \right)^2 \prod_{i=1}^2 \exp \left( \frac{t_i^{\text{true}}}{\tau_{MC}} - \frac{t_i^{\text{true}}}{\tau_{\text{goal}}} \right) \quad (1)$$

538 in order to mimic a sample with lifetime  $\tau_{\text{goal}}$ .

539 Figure 20 shows a comparison between the efficiency-vs-lifetime curve from this re-weighting method,  
 540 for an  $R$ -hadron sample (402735) with 2 TeV gluino and 100 GeV neutralino) at 1 ns, and different  
 541 samples simulated with different lifetimes: 402777 (0.01 ns), 402785 (0.04 ns), 402793 (0.1 ns), 402145  
 542 (10 ns), 402146 (30 ns) and 402147 (50 ns). The method shows closure to within the statistical uncer-  
 543 tainty.

544 In theory, equation (1) should hold for all lifetimes, but in practice, with finite-sized MC samples there is  
 545 not enough statistics in the tails of the input distributions. This leads to an underestimate of the resulting  
 546 efficiency for the target lifetime, as it is likely that the input MC sample would not contain any of the  
 547 events with one DV in our fiducial region and one at large distance, which ought to receive a large weight  
 548 at high  $\tau_{\text{goal}}$ . Therefore with the available MC samples, the considered range of  $c\tau$  goes up to  $\sim 10$  m.

## 549 5. Background estimation

550 One of the powerful features of this search for new physics via displaced vertices with high visible vertex  
 551 masses and high track multiplicities, is the low level of background. In fact, there are no SM physics  
 552 processes giving rise to this signature. However, there are three sources of instrumental backgrounds  
 553 which can produce massive displaced vertices with large track multiplicities.

- 554 • **Hadronic interactions:** Particles interacting with the detector material can produce secondary  
 555 vertices, which are difficult to differentiate from displaced vertices arising from long-lived particle  
 556 decays. These can potentially be massive and have a high track multiplicity to fall into the signal  
 557 region.
- 558 • **Merged vertices:** The last step in the vertexing algorithm are to merge vertices if they are within  
 559 1 mm from each other. Therefore, it is possible that two vertices from two different decays are  
 560 merged when they shouldn't be, producing a displaced vertex with a high track multiplicity and  
 561 large invariant mass.
- 562 • **Randomly crossing tracks:** A track, from any source, which crossing a real vertex might be  
 563 reconstructed as a part of the vertex. Thereby, increasing the number of tracks associated to the  
 564 vertex as well as increasing the invariant mass of the vertex. The larger the angle at which the track  
 565 crosses the vertex, the larger the invariant mass will become.

566 In all of these background estimation techniques, the “*BASE*” event selection defined in 3 is used. In  
 567 addition, the result of these estimations is at the *vertex* level. The final estimate of the signal region yield  
 568 therefore requires an additional step to account for the “*FULL*” event selection efficiency difference, as well  
 569 as obtaining the number of expected signal region *events*. This is explained in detail in Section 5.6.

570 The following sections detail the different sources of background and the data-driven methods used to  
 571 estimate them.

### 572 5.1. Overview of control, validation and signal regions

573 Table 7 contains a summary of the requirements that define the samples of events (and vertices considered  
 574 within those events) used to derive the background estimates and validate the estimation methods.

### 575 5.2. Hadronic Interaction

576 The large number of vertices from hadronic interactions is significantly reduced thanks to the material  
 577 veto applied using the data-driven material map. However, a small fraction of them could survive the  
 578 material veto and leak into the signal region, due to imperfections either in the material map or the  
 579 vertex position determination. The number of such vertices is estimated by taking advantage of the fact  
 580 that the low-mass peak in the vertex invariant mass distribution is dominated by vertices from hadronic  
 581 interaction, whereas the high-mass tail is dominated by vertices with a random track crossing the vertex  
 582 by chance (see e.g. Figure 21(a)). A simple exponential function is used to fit the tail of the low-mass  
 583 peak in the  $m_{DV}$  distribution, and then is extrapolated to the high-mass region, i.e.  $m_{DV} > 10$  GeV,  
 584 to assess the contributions from this process there. Appendix F confirms and quantifies the validity of

Table 7: Definitions of the control, validation and signal regions in the analysis.

Not reviewed, for internal circulation only

<b>Control Region (CR):</b>	
Event-level requirements:	see description of event pre-selection in Section 3.1
DRAW_RPVLL filter:	see description in Section 2.1.1
DAOD_SUSY15 filter:	see description in Section 2.1.2
Event cleaning	Rejection of bad/corrupted events (LAr, Tile, TTC restart, ...)
Good Runs List	Removal of bad lumi blocks based on data quality assessment
Primary vertex	At least 1 good PV, with $N_{\text{PV}}^{\text{tracks}} \geq 2$ and $ z_{\text{PV}}  < 200$ mm
Non-collision background veto	Reject events where the leading jet satisfies $\text{FracSamplingMax} > 0.8 \text{    EMFrac} > 0.96$
Vertex-level requirements:	
Fiducial region	$R < 300$ mm and $ z  < 300$ mm
Vertex fit quality	$\chi^2/\text{NDOF} < 5$
Displacement from PV (in $x$ - $y$ plane)	$d_{\text{T}}^{\text{PV-DV}} > 4$ mm
Material veto	Not in volume marked as dominated by material
Disabled-module veto	Not in volume affected by disabled Pixel detector modules
<b>Low-<math>E_{\text{T}}^{\text{miss}}</math> Validation Region (VRLM):</b>	on top of CR requirements, see Section 3.3
Additional event-level requirements:	
Upper $E_{\text{T}}^{\text{miss}}$ cut	Offline calibrated $E_{\text{T}}^{\text{miss}} < 150$ GeV
Upper $\Delta\phi_{\min}(E_{\text{T}}^{\text{miss}}, \text{jets})$ cut	$\Delta\phi_{\min}(E_{\text{T}}^{\text{miss}}, \text{jets}) < 0.75$ , using all selected jets with $p_{\text{T}} > 30$ GeV
Additional vertex-level requirements:	
Track multiplicity	$n_{\text{tracks}} = 4$
Invariant mass	$m_{\text{DV}} > 10$ GeV
<b>Material Validation Region (VRM):</b>	(On top of CR def, <i>except material veto!</i> )
Additional vertex-level requirements:	
Material region	The vertices considered are <i>required</i> to be in volume marked as dominated by material
Track multiplicity	$n_{\text{tracks}} = 4$
Invariant mass	$m_{\text{DV}} > 10$ GeV
<b>Signal Region (SR):</b>	(On top of CR requirements)
Additional event-level requirements:	
$E_{\text{T}}^{\text{miss}}$ trigger	Requiring the lowest unprescaled $E_{\text{T}}^{\text{miss}}$ trigger to pass
$E_{\text{T}}^{\text{miss}}$ cut	Offline calibrated $E_{\text{T}}^{\text{miss}} > 250$ GeV
Additional vertex-level requirements:	
Track multiplicity	$n_{\text{tracks}} \geq 5$
Invariant mass	$m_{\text{DV}} > 10$ GeV

Not reviewed, for internal circulation only

585 the assumption of the exponential shape in this analysis by using a data sample enriched with material  
 586 interactions and studies of MC truth information.

587 Figure 21 shows the invariant mass distributions of vertices with four, five, six, or seven or more tracks,  
 588 after basic vertex selections (distance from PV,  $\chi^2$ , material veto and fiducial volume). Each subfigure  
 589 also shows the corresponding fitted exponential function.

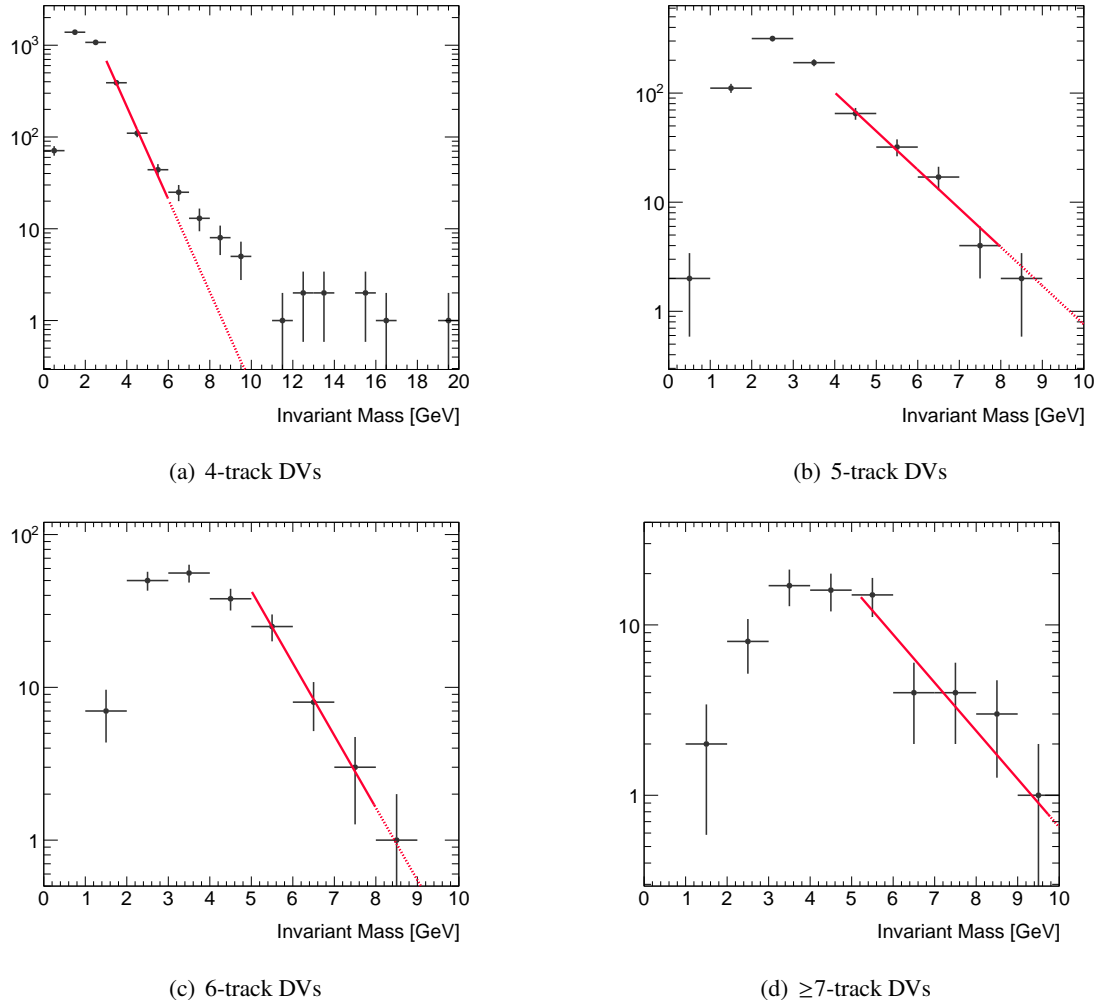


Figure 21: The invariant mass distributions of vertices with more than 3 tracks after basic vertex selections. Red solid lines are fitted exponential functions and Red dashed lines are extrapolation of them.

590 The estimated number of hadronic interaction vertices is  $0.3 \pm 0.10$  for 4-track DVs,  $0.93 \pm 0.56$  for  
 591 5-track DVs,  $0.18 \pm 0.2$  for 6-track DVs and  $1.0 \pm 1.3$  for  $\geq 7$ -track DVs. Note that those estimations  
 592 should be scaled by the event-base scale factor described in Section 5.6, given that the sample is selected  
 593 using the “BASE” vertex selection.

594 The validity of the exponential assumption used in this estimate is tested in a truth-level study using the  
 595 GEANT4-based simulation of hadronic interactions. Using a single slice of PYTHIA8 dijet samples (JZ3W),  
 596 the truth-level mass distributions of hadronic interactions are studied in bins of vertex track multiplicity.  
 597 When fitting the mass distribution to an exponential in the range 5-10 GeV and extrapolating to the

598 region above 10 GeV, a deviation of roughly 300% is seen between the integral of the fit function and the  
 599 truth level distribution. As a result, an additional 300% uncertainty is added to the estimate of hadronic  
 600 interactions. With this additional uncertainty, the hadronic interaction estimates become  $0.3 \pm 0.9$  for 4-  
 601 track DVs,  $0.9 \pm 2.8$  for 5-track DVs,  $0.18 \pm 0.58$  for 6-track DVs and  $1 \pm 3$  for  $\geq 7$ -track DVs. The details  
 602 of this study can be found in Appendix F. While a GEANT4-based study clearly relies on its modelling of  
 603 hadronic interactions, it is currently the only method performed that is protected against the contribution  
 604 of hadronic interactions with an accidental crossing. This contribution is expected to make up much  
 605 of the distribution's tail. Other methods are being explored to quantify the validity of the exponential  
 606 assumption in data.

### 607 5.3. Merged Vertices

608 The vacuum inside the beam pipe reduces the amount of expected hadronic interactions dramatically. Due  
 609 to the proximity to the interaction region, two other sources become more significant.

610 Firstly, due to the high track density, there is a larger probability compared to other regions that two or  
 611 more tracks cross each other and get reconstructed as a displaced vertex. In addition, meta-stable-SM  
 612 particles such as  $B$ -hadrons can give rise to displaced vertices with masses of a few GeV at maximum.  
 613 These are however almost entirely removed by the combination of the  $|d_0| > 2$  mm cut and the require-  
 614 ment that the DV should be at least 4 mm from the PV in the transverse plane.

615 Secondly, because of the high vertex density at small radii and the algorithm used to find secondary  
 616 vertices, it is conceivable that two vertices could get merged into a single vertex with a significantly  
 617 higher mass that could pass the signal region requirements. We quantify this contribution by randomly  
 618 merging vertices in different events, as described below.

619 The “vertex-pair distance method” builds on the fact that the final step of the vertexing algorithm merges  
 620 vertex candidates separated by less than 1 mm. We can view a random combination of four tracks as  
 621 two merged random two-track combinations, and similarly for five-track vertices and up. We plot the  
 622 separation distance between pairs of two-track vertices, or between two-track and three-track vertices, in  
 623 different events, and see how often the vertex pairs are separated by less than 1 mm.

624 In order to normalise the prediction from this estimate, we use the distribution of separation distance  
 625 between vertex pairs in the same event. The aim is to use the  $d < 1$  mm bin of the model to estimate the  
 626 background. This bin will always be empty in the “same event” distance distribution, because any vertex  
 627 pairs here would have been merged into a single vertex. Figure 22(a) shows the modelled distribution  
 628 for pairs of two-track vertices in different events, where the combination of vertices has  $m_{\text{DV}} > 10$  GeV,  
 629 and we can see that it looks slightly different from the distribution of vertex pairs in the same event. This  
 630 motivates the use of a weight, derived from the distributions of the one-dimensional distance in the  $z$   
 631 direction shown in Figure 22(b), to make the model better match the “same-event” distribution. A likely  
 632 reason for the difference in the distributions of distance along the  $z$  direction is correlation between two-  
 633 track vertices in the same event. To correct for this difference, we obtain a weight from the ratio of the  
 634 “different-event” and “same-event”  $z$ -distance distributions, and apply it to the model which then gives  
 635 the final 3D distance distribution.

636 The value of the model at distances  $< 1$  mm after reweighting is taken as an estimate of the number of  
 637 background vertices that could have been formed from merging two separate vertices.

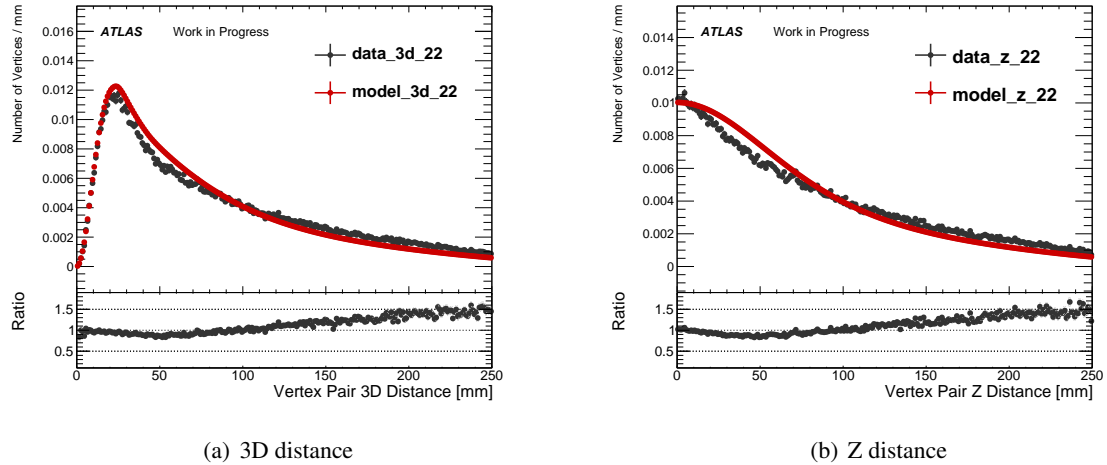


Figure 22: (a) Three-dimensional distance and (b) Z distance between vertex pairs for the DAOD\_SUSY15 datasets before weighting. The black points show the distance between the two-track vertices in the same event. The red points show a model calculated from the distance between two-track vertices in different events. The invariant mass for the combination of the two vertices is required to be  $> 10$  GeV.

638 Figure 23 shows the distributions of 3D distances between vertices in same-event (black markers) and  
 639 different-event (blue histogram) pairs. The top row shows the (2+2)-track estimate with a zoomed-in  
 640 view of the small-distance region, and the bottom row shows the same for the (2+3)-track estimate.

641 The estimated numbers of merged vertices are  $3.69 \pm 3.69$  for (2+2)-track vertices and  $0.01 \pm 0.01$  for  
 642 (2+3)-track vertices. Note, as in the previous section, this background estimate is made using events that  
 643 do not pass all the event cuts, so the estimate have to be scaled by the event-base scale factor described in  
 644 Section 5.4.2.

#### 645 5.4. Randomly crossing tracks

646 Displaced vertices arising from standard model processes, such as meta stable particles or hadronic inter-  
 647 actions, typically have low track multiplicity and mass. However, if a random track gets mis-reconstructed  
 648 as part of the vertex there is a possibility the vertex will attain a track multiplicity and invariant mass high  
 649 enough to fall into the signal region. A data-driven method has been developed, whereby the random  
 650 crossings are simulated by adding a random track to a seed vertex and recalculating the invariant mass of  
 651 the vertex.

652 Before entering into the details of the method, here follows a few definitions. Three regions are defined,  
 653 depending on the number of tracks in the vertices. The *control region* (CR) is made up of vertices with  
 654 three tracks, the *validation region* (VR) is made up of vertices with four tracks (see Table 7), and finally  
 655 vertices with five or more tracks define the *signal region* (SR).

656 Moreover, the geometric fiducial volume is divided into twelve individual regions as shown in Figure  
 657 24.

658 Invariant mass spectra of the vertices are created individually for these twelve regions. This division is  
 659 made in order to include the radial dependence on the reconstructed vertices and the random track. The

Not reviewed, for internal circulation only

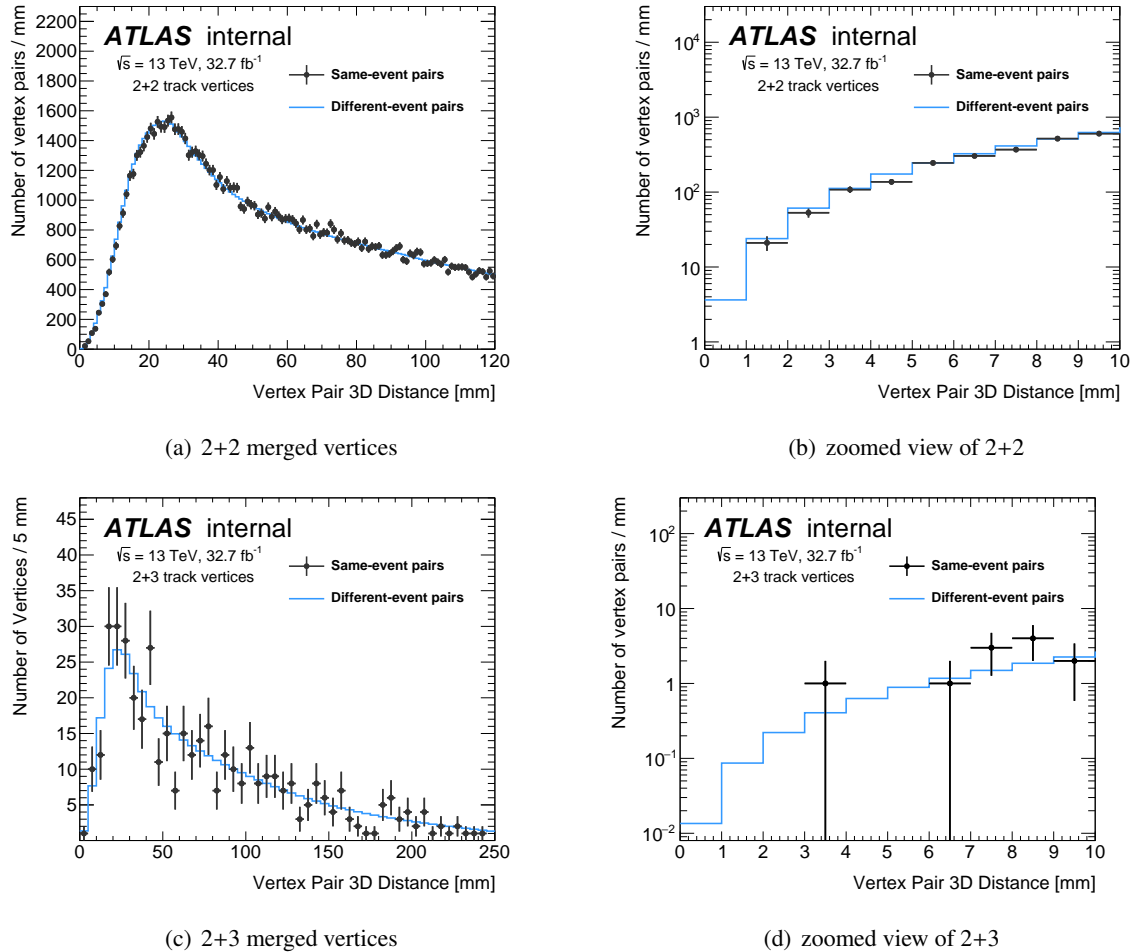


Figure 23: (a) Three-dimensional distance between pairs of two-track vertices, after reweighting. The top right histogram (b) is a close-up view of the left histogram. (c) Three-dimensional distance between two-track and three-track vertex pairs, after weighting. (d) A close-up view of the 3D distance between two-track and three-track vertices, after weighting. The black points show the distance between the vertex pairs in the same event. The blue histograms show the prediction of the model which uses the distance between pairs of vertices in different events. The model prediction for  $d < 1 \text{ mm}$  gives the estimate for the number of high-mass four-track or five-track vertices.

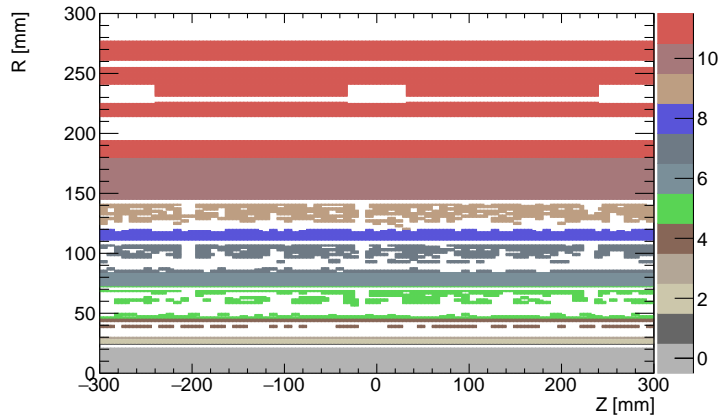


Figure 24: The properties of the displaced vertices changes as a function of  $r_{DV}$ , depending on the track properties. Therefore, to produce a correct background estimation, the fiducial volume is divided into twelve regions.

properties of the tracks associated to vertices varies significantly with at which radial region the vertices were reconstructed in and thereby affecting the mass spectrum of the potential random crossings [10]. This data-driven method relies on the hypothesis that the probability for a track passing nearby a vertex and get associated to it in the vertex reconstruction, is independent of the number of *real* tracks generated in that vertex. Therefore, it can use vertices with  $(n - 1)$  associated tracks, and after properly adding a track to that vertex, it becomes a  $n$ -track, high-mass vertex. Eq. (2) defines the expression for this model concisely and defines the components:

$$N_{DV_n} = f h_n(m_{DV}) \quad (2)$$

Here  $h_n(m_{DV})$  is the high-mass vertex distribution model, built from  $(n - 1)$ -track vertices, adding a random track and recalculating the invariant mass.  $N_{DV_n}$  is the *real*  $n$ -track vertices, data output from the vertex reconstruction algorithm, and  $f$  is the normalization factor, also called a *crossing factor* since it represents the probability that a vertex is randomly crossed by an additional track in the event. This is determined using data in the control region.

#### 5.4.1. Seed vertices and track templates

Seed vertices are defined as  $(n - 1)$ -track vertices, whereby adding random tracks produces  $n$ -track vertices. All reconstructed vertices, passing the initial primary and displaced vertex selection criteria (Section 3.4) with the exception for invariant mass and track multiplicity cuts, are considered seed vertices. Moreover, the seed vertices are divided into the twelve radial regions.

The random tracks are picked from track templates, which are constructed by saving the significant track properties into three-dimensional histograms. All tracks in reconstructed vertices, with the mass above 3 GeV and the number of associated tracks is at least 3, are stored in the track templates. For all radial regions,  $\eta$ , the relative azimuthal angle between the track and the direction of the PV-DV vector ( $\Delta\phi$ ), and the  $p_T$  of the tracks are stored. The relative angle is used instead of the absolute, in order to avoid

Not reviewed, for internal circulation only

682 creating vertices that would not be reconstructed by the vertex algorithm. For example, if the absolute  
 683 angle is used, adding this track to a seed could easily create a vertex with a back-to-back topology. Such  
 684 vertices would not be found in data as they will be removed by the fake removal (Section 3.2.2). A simple  
 685 schematic showing how the relative angles of the track is defined and how the track is added to a seed  
 686 vertex is shown in Figure 25. The properties of template tracks are shown in Figure 26 for all radial  
 687 regions. Only tracks with  $\Delta R > 1.0$  are used to add to any seed vertex. Using tracks with lower  $\Delta R$  in  
 688 building the estimate would be a waste of statistics as these vertices would not have high mass and fall  
 689 outside the SR. Validation of this statement is covered in much greater details in reference [10].

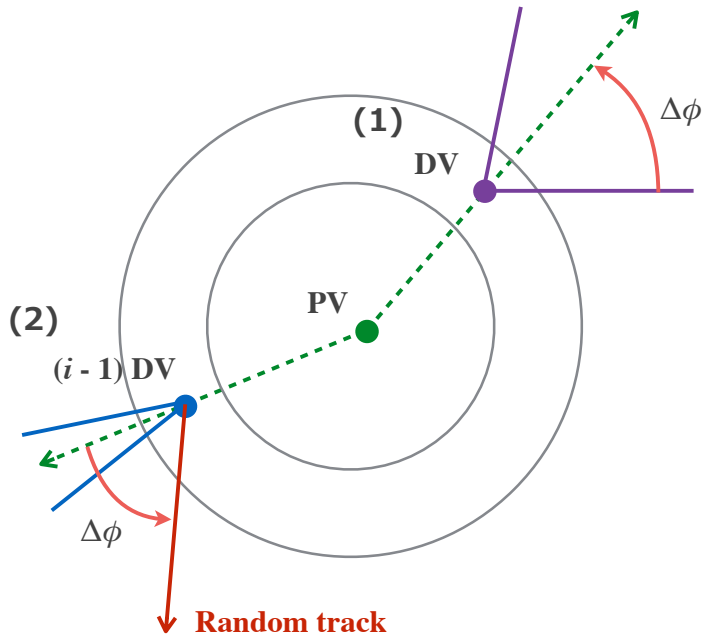


Figure 25: Schematic drawing showing the two steps of the random-track association method. In the vertex labeled 1) the relative azimuthal angle  $\Delta\phi$  (marked with the curved red arrow) to the PV-DV direction (green dashed arrow) for each track in a DV which are filled into the track templates, and templates of  $\eta$  and  $p_T$  are built up in the same way). Part 2) shows how the random track with properties generated from the track templates are added to the  $(n - 1)$ -track seed vertex to construct an  $n$ -track DV, which after repeating the process many times gives a mass template. The concentric circles represent a simplification of a radial region of the fiducial volume.

#### 690 5.4.2. Constructing the invariant mass templates

691 The method consists of three steps.

- 692 1. Construct templates for the vertex mass distributions of possible combinations of  $(n-1)$ -track DV  
 693 plus a random track (e.g. 2+1, 3+1, 4+1 and 5+1 or higher), i.e.,  $h_i(m_{DV})$ . Then add randomly  
 694 generated tracks to seed vertices to create vertex-mass templates for each radial region separately.
- 695 2. Extract the normalization factor  $f$  by scaling the mass template from the random-track association  
 696 method in the control region to the data, i.e. scale the model using (2+1)-track vertices to the

Not reviewed, for internal circulation only

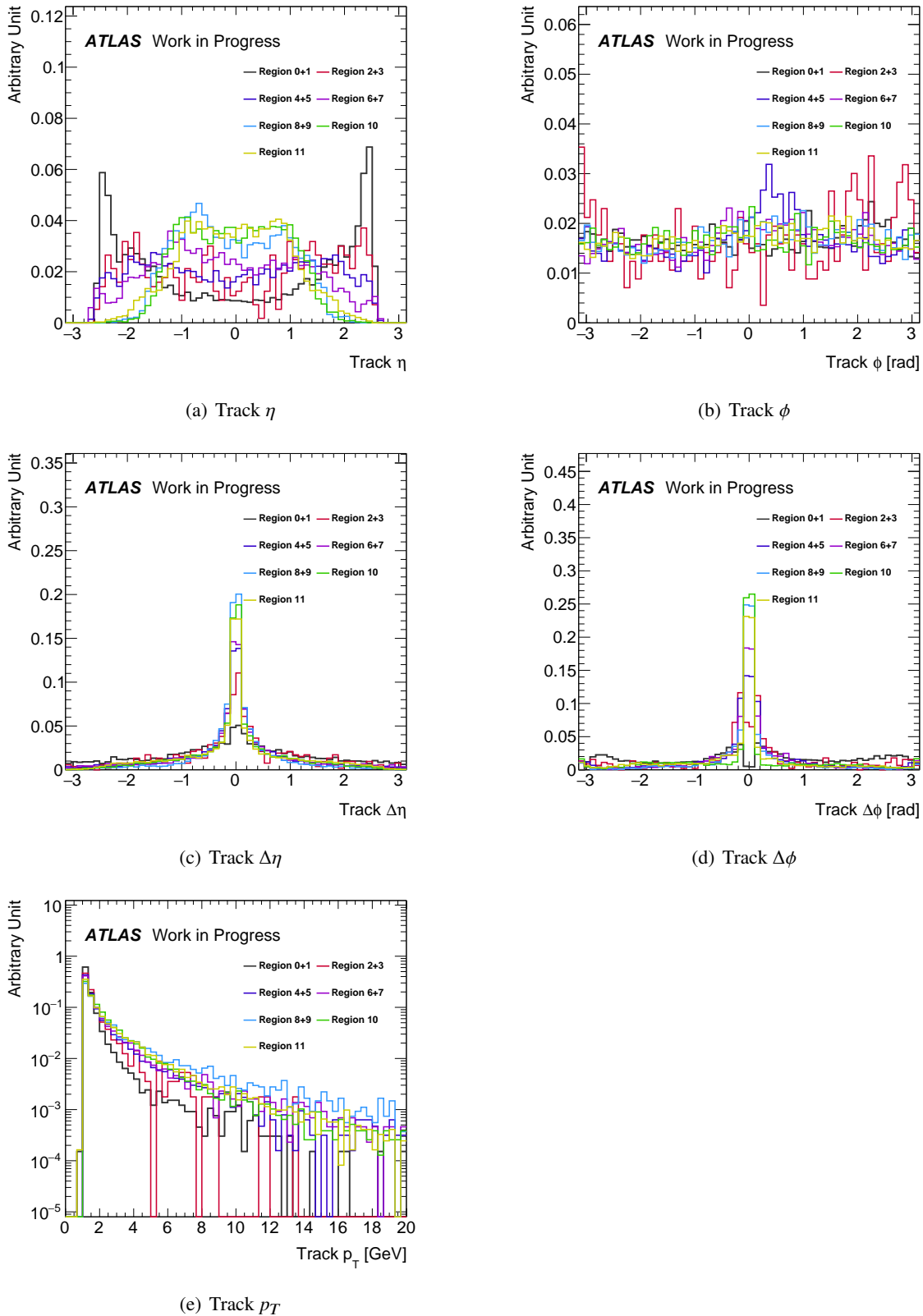


Figure 26: The properties  $\eta$ ,  $\phi$ ,  $\Delta\eta$ ,  $\Delta\phi$ ,  $p_T$  of tracks in the track templates for each region ( $\Delta$  means with respect to the PV-DV direction). Several adjacent radial regions are merged because it is too dense to show 12 histograms overlaid. The central dips in  $\Delta\phi$  distributions come from a requirement that only tracks with  $d_0 > 2$  mm are used for secondary vertexing.

Not reviewed, for internal circulation only

697 3-track vertices in the data. This gives a vertex-level estimate at high mass.

$$f = \frac{\int_{m_{\text{DV}}^{\text{min}}}^{+\infty} N_{\text{DV}_{3-\text{trk}}} dm_{\text{DV}}}{\int_{m_{\text{DV}}^{\text{min}}}^{+\infty} h_3 dm_{\text{DV}}} \quad (3)$$

698 3. Scale the estimated number of high-mass vertices with an event-based scale factor accounting for  
 699 the difference in event selection efficiency for the event pre-selection and the final event selection  
 700 which also includes explicit trigger and offline  $E_T^{\text{miss}}$  requirements.

701 The templates are constructed separately for each of the radial regions by looping over the seed vertices  
 702 and adding a random track from the corresponding track template. This is done for all track multiplicities  
 703  $n$  of the seed vertices. For the second step, a simple method is used to estimate the probability of having  
 704 a randomly crossing track, the so-called ‘‘crossing fraction’’. The control region is used to extract this  
 705 factor, i.e. the (2+1)-track  $m_{\text{DV}}$  template is normalised to give the same number of vertices as is seen in  
 706 the high-mass region of the observed 3-track DV spectrum. The extracted crossing fractions are shown  
 707 in Figure 27 for all radial regions separately. The resulting invariant mass spectra, scaled by the extracted  
 708 crossing fractions, are able to reproduce the shape of the high-mass distribution from data in the CR  
 709 (3-track vertices) as shown in Figures 28 and 29.

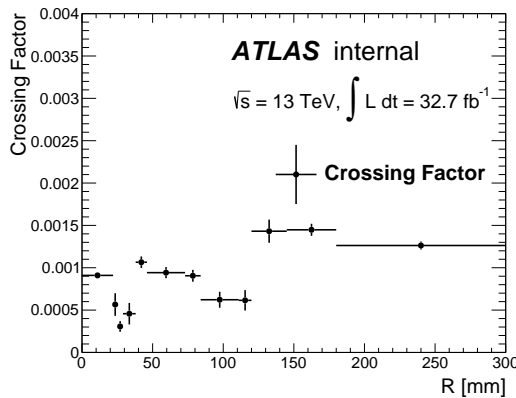


Figure 27: Crossing factor for the twelve radial region for 2016 data. The factors are calculated by normalising the model to data in the control region, for vertices with three tracks and mass larger than 10 GeV. The error bars represent the statistical uncertainties.

## 710 5.5. Validation of the background estimation

711 The background estimation method (including the crossing fractions) is validated in the two VRs. Figure  
 712 42 shows the number of displaced vertices integrating the invariant mass spectra for twelve regions  
 713 for masses larger than 10 GeV in both VRLM and VRM. Data and the prediction agree well within the  
 714 uncertainties. The two following subsections discuss the considerations that went into the design of these  
 715 regions and how they are used to test the validity of the background estimation techniques.

716 A region differing from the SR only in the track multiplicity, i.e. looking at 4-track vertices only instead  
 717 of 5-track vertices and higher, has a high signal acceptance. With significant signal contamination, this

Not reviewed, for internal circulation only

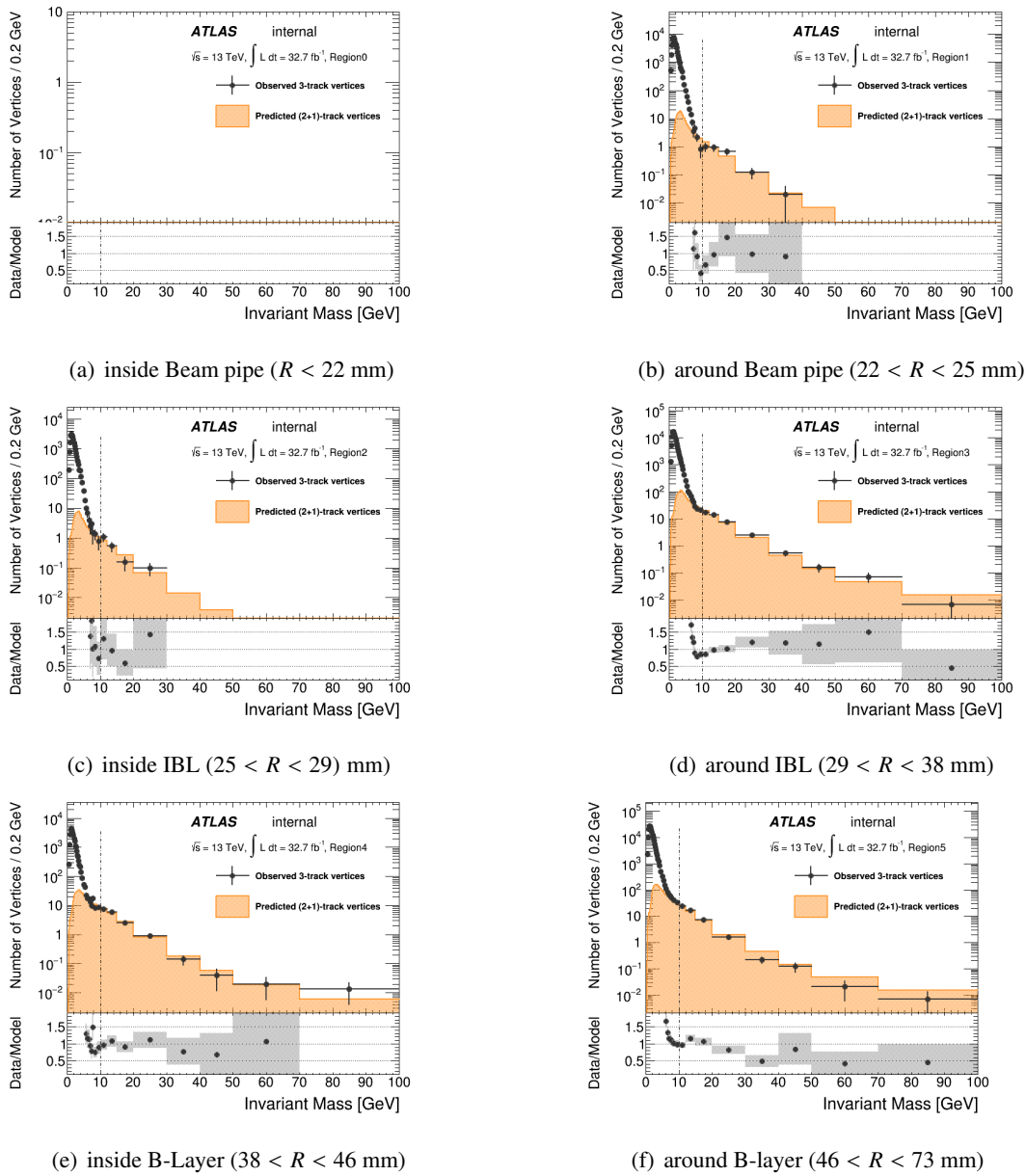


Figure 28: 3-track  $m_{\text{DV}}$  distributions of 2016 data. The modelled distributions are normalised to data by use of the high-mass range e.g.  $m_{\text{DV}} > 10$  GeV. The modelled vertices reproduce the high-mass shape distribution of the data.

Not reviewed, for internal circulation only

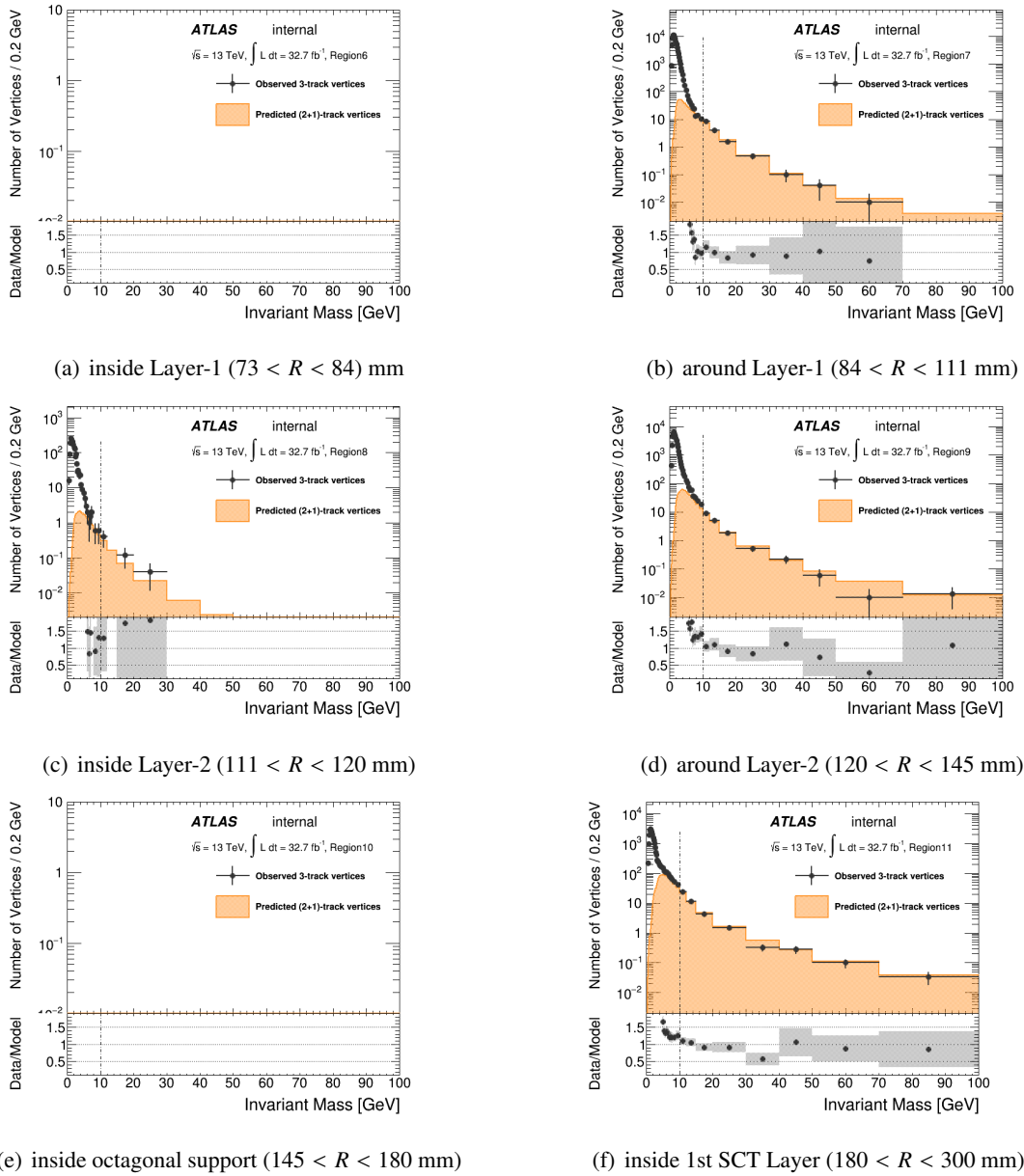


Figure 29: 3-track  $m_{DV}$  distributions of 2016 data. The modelled distributions are normalised to data by use of the high-mass range e.g.  $m_{DV} > 10$  GeV. The modelled vertices reproduce the high-mass shape distribution of the data. The error bars in the mass distributions and the grey bands in the bottom ratio distributions show the statistical uncertainties.

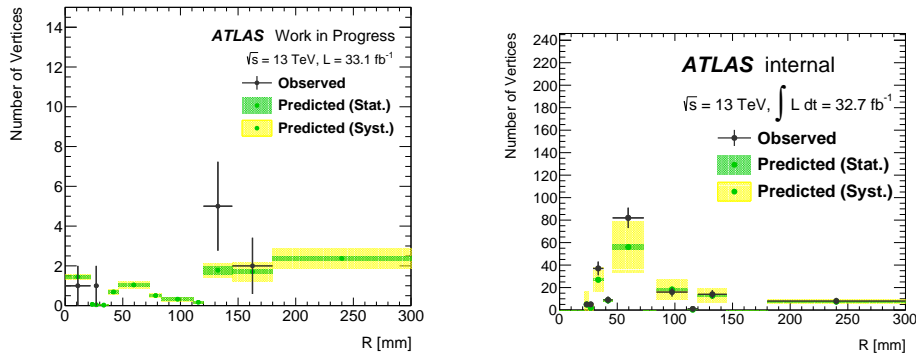


Figure 30: The number of observed events (black points) in the high-mass range,  $m_{\text{DV}} > 10 \text{ GeV}$ , are compared with those predicted by the random-track association model (histogram with uncertainty bands), for the displaced vertices in the 4-track validation region in each radial region separately. The left plot shows how the method performs in the low- $E_{\text{T}}^{\text{miss}}$  region, VRLM, and the right plot shows the same for the material-dominated region, VRM.

718 region can not be used for the validation of the background estimate. This subsection describes the design  
719 and considerations that went into designing the two validation regions used to validate the background  
720 estimation as seen in Figure 42.

721 The first region is a 4-track region efficiently depleted of signal using an upper  $E_{\text{T}}^{\text{miss}}$  cut. This low- $E_{\text{T}}^{\text{miss}}$   
722 VR is denoted “VRLM”.

723 The second region is made up of vertices in regions dominated by material interactions and is denoted  
724 “VRM”. This region is enriched in hadronic interactions by inverting the material veto requirement, ef-  
725 fectively picking out the vertices where we expect to be dominated by vertices from instrumental effects  
726 rather than in-flight decays of long-lived particles. The hadronic interaction vertices are however also  
727 susceptible to randomly crossing tracks and can therefore be used to validate the estimation method for  
728 the backgrounds stemming from this mechanism. So while dissimilar in the inverted material map veto,  
729 the VRM region allows for high-stats validation of the methodology used for the random-track crossing  
730 estimate (i.e. the  $n + 1$  estimate).

### 731 5.5.1. Low- $E_{\text{T}}^{\text{miss}}$ Validation Region - VRLM

732 Because of the significant signal contamination in a simple 4-track vertices region, additional signal-  
733 depleting requirements are placed on the events used in this validation. Placing a maximum requirement  
734 on the  $E_{\text{T}}^{\text{miss}}$  depletes this region of high mass-splitting signals significantly. Signal scenarios with small  
735 mass-splitting unfortunately retain a high signal acceptance due to the low amount of intrinsic  $E_{\text{T}}^{\text{miss}}$  in  
736 these events. Because of this, an additional requirement is made on the smallest azimuthal angle between  
737 the measured  $E_{\text{T}}^{\text{miss}}$  and the reconstructed jets in the event,  $\Delta\phi_{\text{min}}$ . Because much of the background  
738 for this analysis originates from multijet events with mismeasured jets yielding  $E_{\text{T}}^{\text{miss}}$ , the  $\Delta\phi_{\text{min}}$  of these  
739 events is peaked at 0 and  $\pm\pi$ . SUSY signal signatures, even those with low intrinsic  $E_{\text{T}}^{\text{miss}}$  are more  
740 likely to obtain larger values of  $\Delta\phi_{\text{min}}$ . For the current search, this variable is calculated using all jets  
741 with  $p_{\text{T}} > 30 \text{ GeV}$ .

742 Distributions for the  $E_T^{\text{miss}}$  and  $\Delta\phi_{\text{min}}$  quantities are shown in data as well as for various signals in Figure 31 where the discrimination power can be seen.  
 743

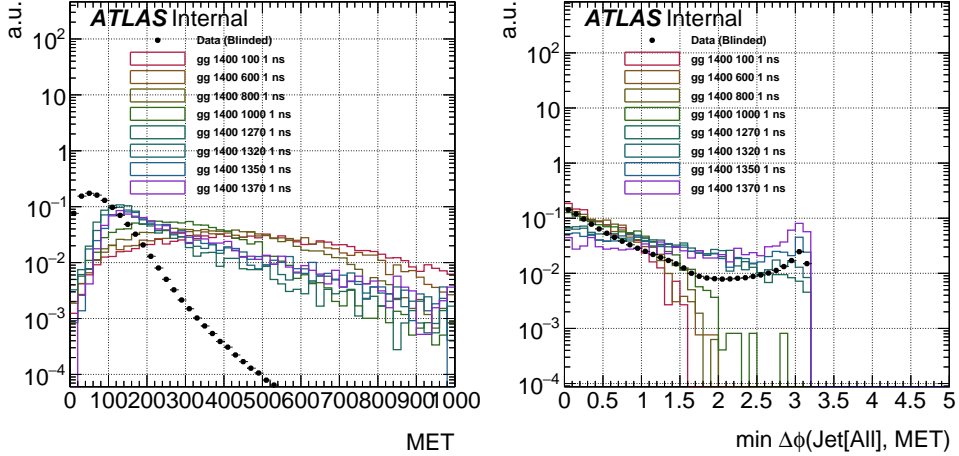


Figure 31: Normalized distributions are shown for data and various signals.

744 In order for a validation in this region to hold in the SR, it must be shown that the DV properties are  
 745 uncorrelated with both of these event quantities. The distributions for the DV mass and track multiplicity  
 746 are shown in slices of  $E_T^{\text{miss}}$  and  $\Delta\phi_{\text{min}}$  in Figure 32. These show a minimal dependence, when the tails  
 747 are normalized to the same integral, on  $E_T^{\text{miss}}$  and  $\Delta\phi_{\text{min}}$ . For this reason, it is reasonable to test the  
 748 background estimation in a portion of the space spanned by  $E_T^{\text{miss}}$  and  $\Delta\phi_{\text{min}}$  that is constructed to be  
 749 free of signal contamination, and trust that it works well also in a more inclusive selection without these  
 750 requirements.

751 It is utilizing this same non-correlation between DV properties and these variables that further allows  
 752 one to scale the 4-track DV estimate described above by the efficiency of passing the VR requirement of  
 753  $E_T^{\text{miss}} < 150 \text{ GeV}$  and  $\Delta\phi_{\text{min}} < 0.75$ , since this efficiency can be measured in the events populating the  
 754 3-track control region. This efficiency is measured in the 3-track region to be  $1709/3049 = 56\%$ . As a  
 755 result, each of the yields from the various background estimations obtained inclusively in the  $E_T^{\text{miss}}, \Delta\phi_{\text{min}}$   
 756 space are scaled by 56%. Accounting for the residual correlation between the  $E_T^{\text{miss}}$  and the DV properties,  
 757 a 10% systematic uncertainty is applied to this. The 4-track estimate in VRLM is  $(16.5 \pm 3.8) \times (56\% \pm$   
 758  $6\%) = 9 \pm 2$  events expected. This is consistent with the observed 9 events. A diagram summarizing how  
 759 the region is defined and where the various quantities are measured is shown in Figure 33.

760 So, by requiring  $E_T^{\text{miss}} < 150 \text{ GeV}$  and  $\Delta\phi_{\text{min}} < 0.75$ , we end up with a VR without significant contam-  
 761 ination from any of the considered signals not yet excluded. The levels of signal contamination expected  
 762 in this region are shown in Figure 34, for varying gluino mass and lifetime. For the portion of signal  
 763 parameter space that is not excluded by Run-1 results, signal contamination for this region is at or below  
 764 the 10% level.

765 Finally, Figure 35 shows the distribution of the azimuthal angle of the measured  $E_T^{\text{miss}}$  in data events  
 766 falling in VRLM. The distribution in data shows no features that are indicative of significant contamination  
 767 from non-collision background processes.

Not reviewed, for internal circulation only

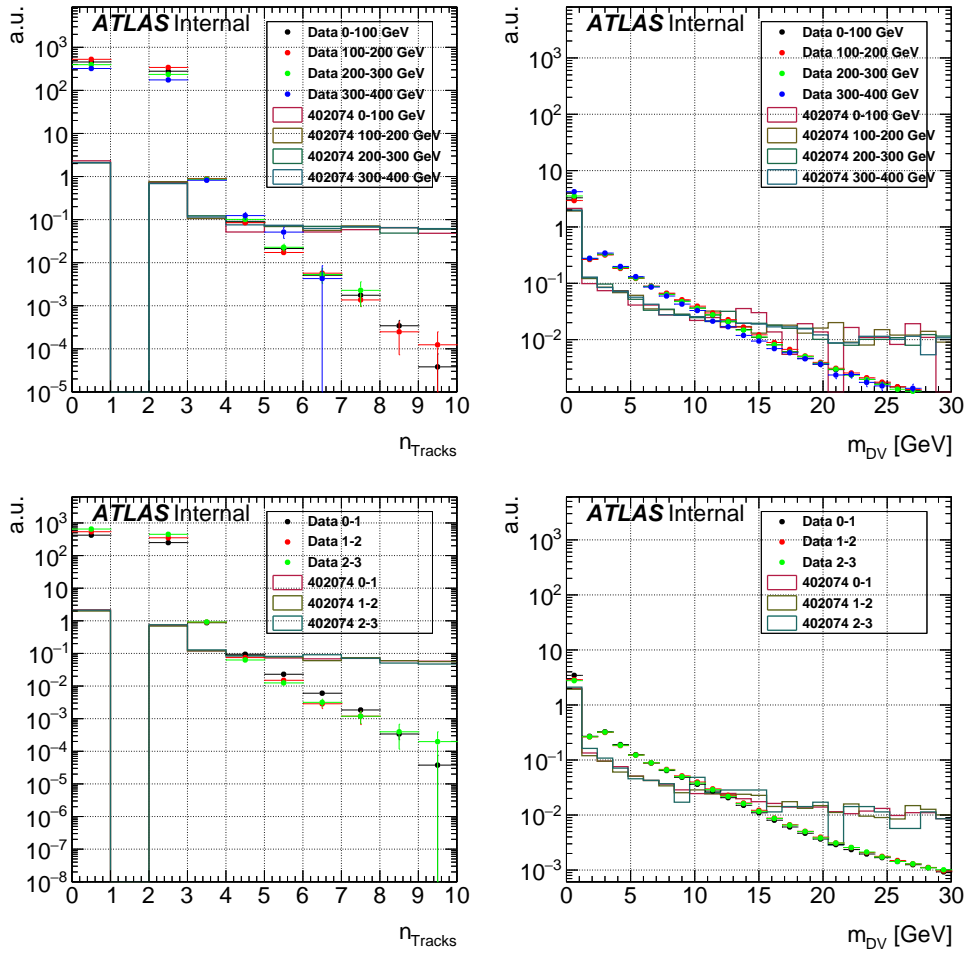


Figure 32: The properties of the DV candidates are shown as a function of  $E_T^{\text{miss}}$  (top) and  $\Delta\phi_{\min}$  (bottom). DV mass (right) and track multiplicity (left) are shown. The track multiplicity plots are normalized to the area above 3 and the mass distributions are normalized to the area above 3 GeV. Note that the 0-bin entry in the track multiplicity distributions is referring to the DV do not pass the  $m_{DV} > 10$  GeV requirement.

Not reviewed, for internal circulation only

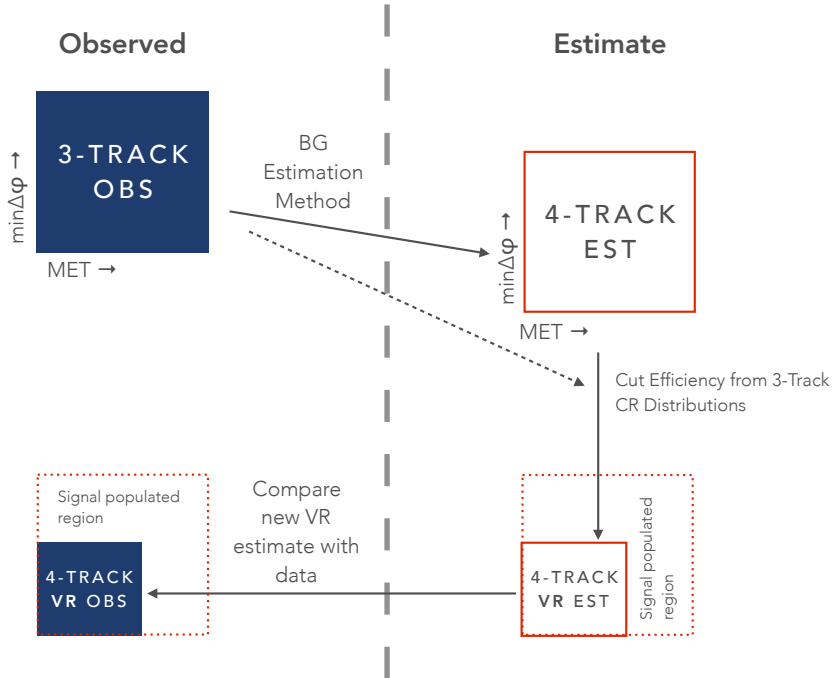


Figure 33: A qualitative diagram of the VRLM design is shown.

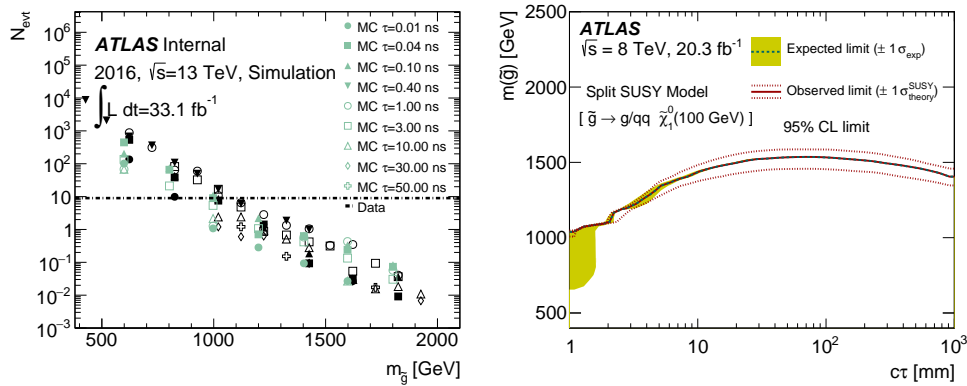


Figure 34: Signal yields are shown (markers) as a function of R-Hadron lifetime (shape) and gluino mass (x-axis). Those signal models with a 100 GeV LSP are shown in black with a slight offset in gluino mass. For reference, the yield in VRLM in data is shown in the dashed black line. For convenience, the Run-1 exclusion limits are shown in the right plot for models with a 100 GeV LSP.

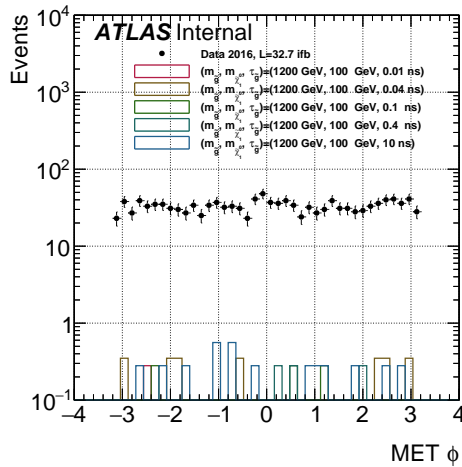


Figure 35: The azimuthal angle of the measured  $E_T^{\text{miss}}$  is shown for events in VRLM. The distribution shows no evidence of significant contribution from beam-induced non-collision background.

Not reviewed, for internal circulation only

### 768 5.5.2. Material-dominated Validation Region - VRM

769 When the material veto requirement is inverted, i.e. only vertices in the dense material-dominated regions  
 770 are selected, the contributions from hadronic interactions increase dramatically. Just like the DVs from in-  
 771 flight decays, these vertices can also be crossed by a random track. The amount of vertices with randomly  
 772 crossing tracks is proportional to not only the track density but also the number of seed vertices. As the  
 773 acceptance has been highly reduced, the contribution from the signal vertices to that region are going to  
 774 be reduced also, allowing to obtain a region with high statistics yet low signal contamination. Figures 36  
 775 and 37 show 3-track  $m_{\text{DV}}$  distributions of 2016 data along with the predictions from the random-track  
 776 model using the inverted material veto requirement. One can see that the predictions agree well with data  
 777 in the material-rich regions as well. Region 0, 6 and 10 are excluded in the plots because the volume  
 778 vetoed by material map in those regions is tiny.

779 In addition, Figures 38 and 39 show the same distributions for 4-track DVs. The high-mass tails are well  
 780 modelled by the orange mass templates.

781 Summary of the observed and expected numbers of 4-track DVs with  $m_{\text{DV}} > 10$  GeV in the regions with  
 782 inverted material veto is shown in Figure 40(a). The agreement between data and estimation is good in this  
 783 region. The observed number of DVs there is 177. The expected number of DVs from randomly crossing  
 784 tracks is  $137.4 \pm 2.9$  (stat.)  $\pm 29.8$  (syst.). The difference between these numbers could be somewhat  
 785 explained by contribution of hadronic interactions.

786 Figure 40(b) shows the summation of the 4-track  $m_{\text{DV}}$  distributions. The number of DVs from hadronic  
 787 interaction is estimated by fitting this using an exponential function and extrapolating it to  $m_{\text{DV}} > 10$  GeV.  
 788 The estimated number of DVs from hadronic interactions is  $15.8 \pm 0.9$  (stat.).

789 Signal contamination in this VR is evaluated in Figure 41. The event yields of signal samples which are  
 790 not excluded yet ( $m_{\tilde{g}} \gtrsim 1$  TeV) are below 10% level of the event yield of data.

Not reviewed, for internal circulation only

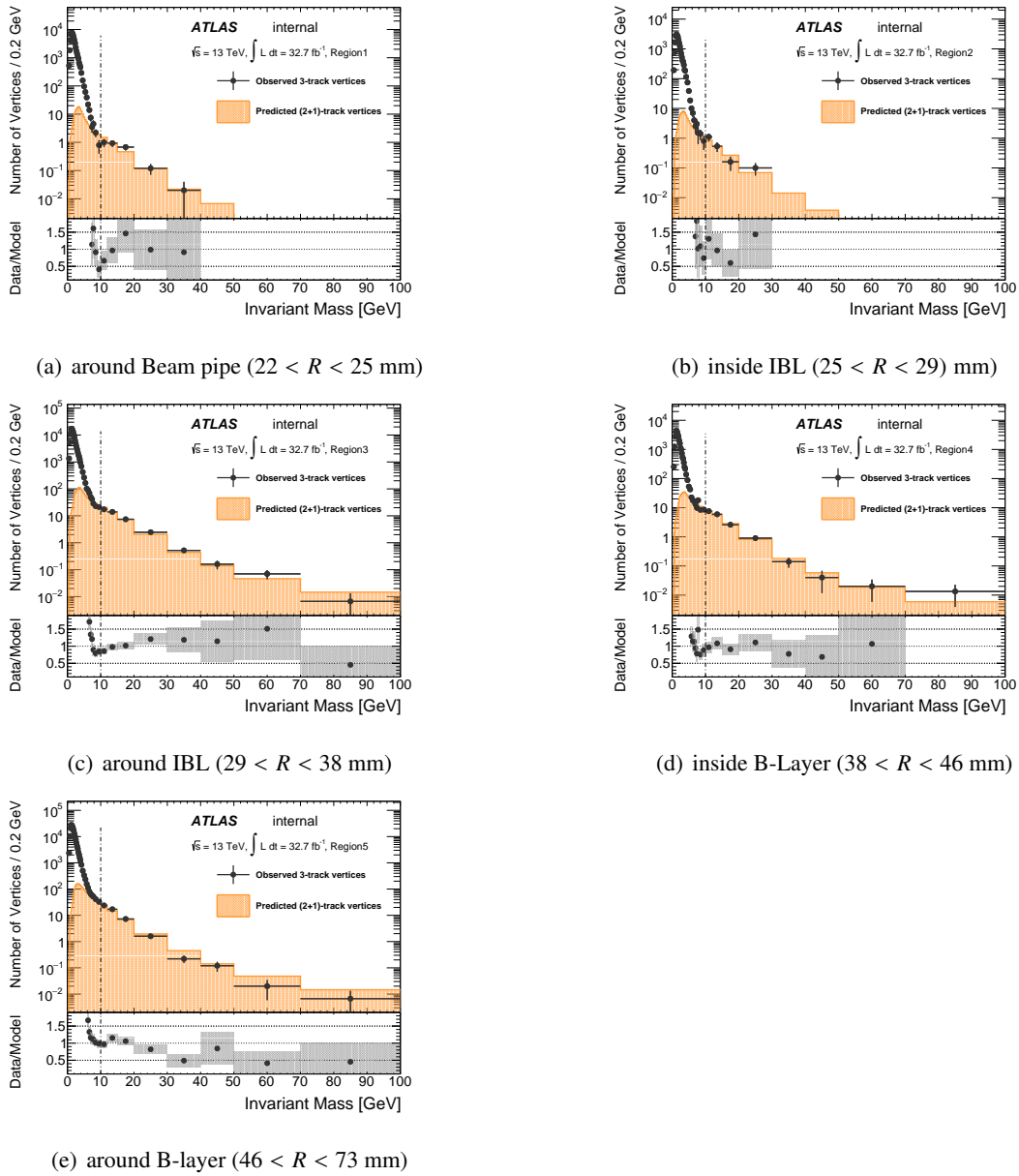


Figure 36: 3-track  $m_{DV}$  distributions of 2016 data with inverted material veto requirement. The modelled distributions are normalised to data by use of the high-mass range e.g.  $m_{DV} > 10$  GeV. The model reproduces shape of the distribution of the data at high mass well.

Not reviewed, for internal circulation only

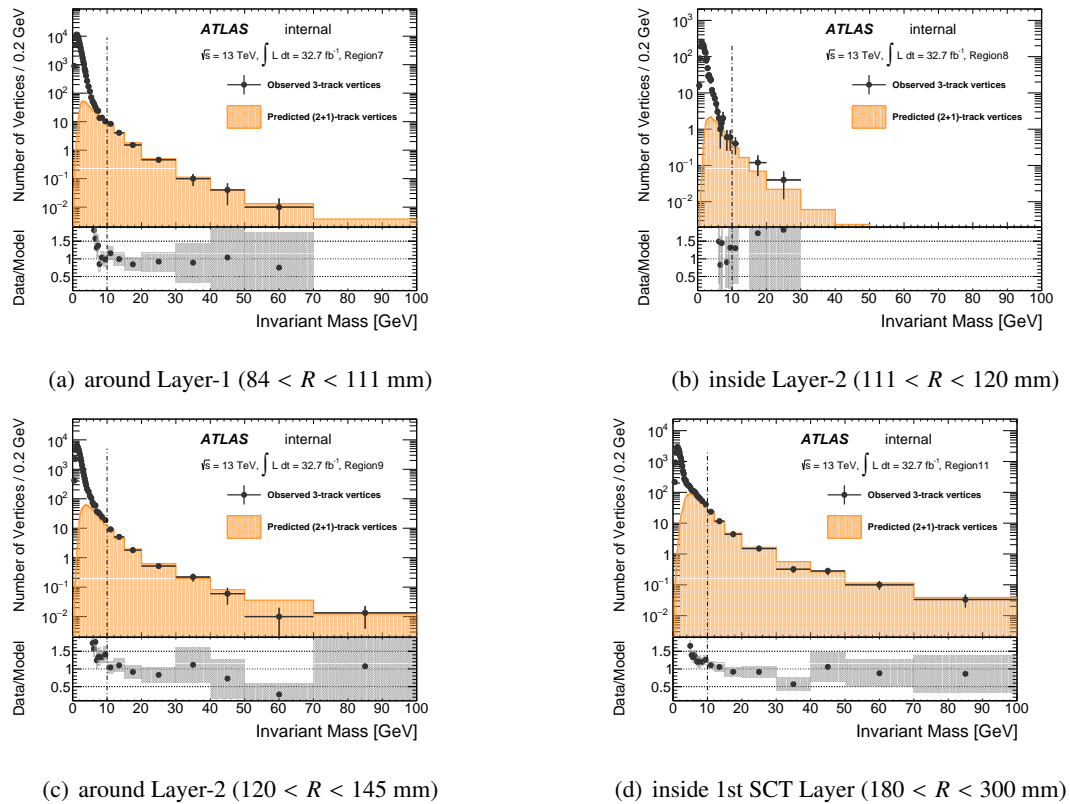


Figure 37: 3-track  $m_{DV}$  distributions of 2016 data with inverted material veto requirement. The modelled distributions are normalised to data by use of the high-mass range e.g.  $m_{DV} > 10. The model reproduces the shape of the high-mass region of the distribution for the data well. The error bars in the mass distributions and the grey bands in the bottom ratio distributions show statistical uncertainties only.$

## 791 5.6. Total background estimate and event-selection transfer factor

792 The output of the background estimation techniques, the total number of vertices, integrating over all  
 793 regions for vertices with a mass larger than 10 GeV, is shown in Tab. 8. These estimates represent the  
 794 expected number of selected vertices (i.e. *not number of events*) given the “BASE” event selection defined  
 795 in Section 3.

796 In order to obtain an estimate for the number of observed signal region events, two conversions must be  
 797 made. One must account for the event selection difference between the “BASE” event selection and the  
 798 “FULL” event selection used for the signal region events. Multiplying the estimate by the ratio of the yields  
 799 for the two selections accounts for this effect.

800 The second consideration is the conversion from a vertex-level estimate to an event-level estimate for  
 801 the sake of interpretations. This is, ideally, the ratio of the number of *vertices* observed in the “FULL”  
 802 event selection to the number of *events* observed in the “FULL” event selection. Unfortunately, this is not  
 803 accessible without unblinding, so a proxy is used: the ratio of the number of *vertices* (passing the “FULL”  
 804 vertex selection) in the “BASE” event selection to the number of *events* (with a vertex passing the “FULL”  
 805 vertex selection) in the “BASE” event selection. The degree to which this is an appropriate proxy will be  
 806 taken as a systematic; the procedure for this is defined in Section 6.

Not reviewed, for internal circulation only

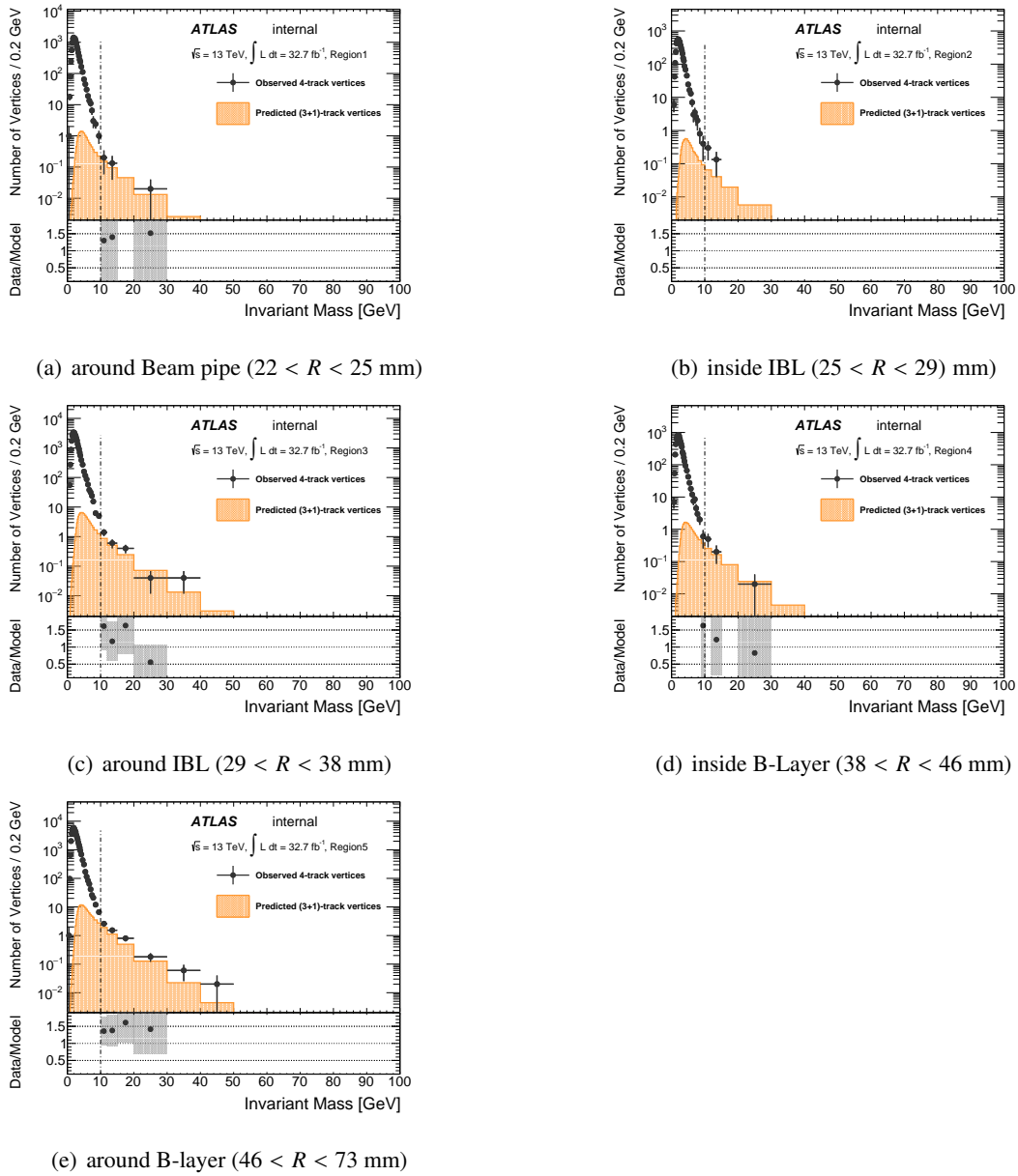


Figure 38: 4-track  $m_{DV}$  distributions of 2016 data with inverted material veto requirement. The modelled distributions are normalised to data by use of the high-mass range e.g.  $m_{DV} > 10$  GeV. The model reproduces the shape of the high-mass region of the distribution for the data well.

Not reviewed, for internal circulation only

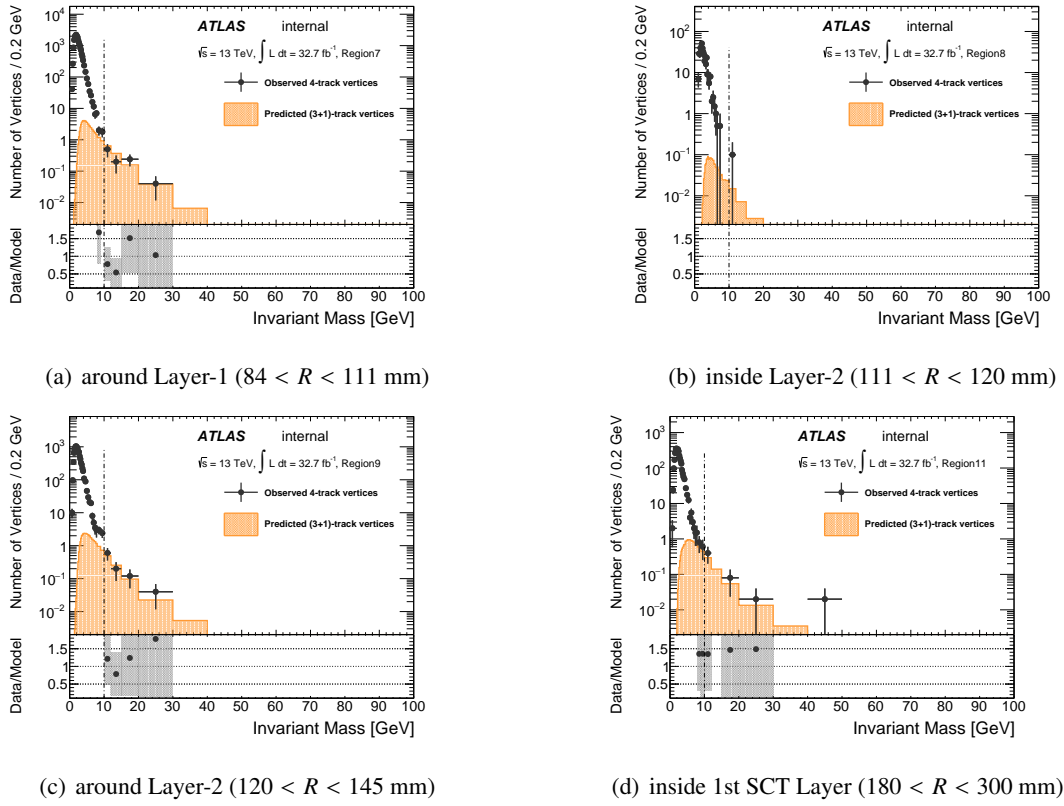


Figure 39: 4-track  $m_{DV}$  distributions of 2016 data with inverted material veto requirement. The modelled distributions are normalised to data by use of the high-mass range e.g.  $m_{DV} > 10$  GeV. The model predictions match the shape of the high-mass region of the distribution for the data well. The error bars in the mass distributions and the grey bands in the bottom ratio distributions show statistical uncertainties only.

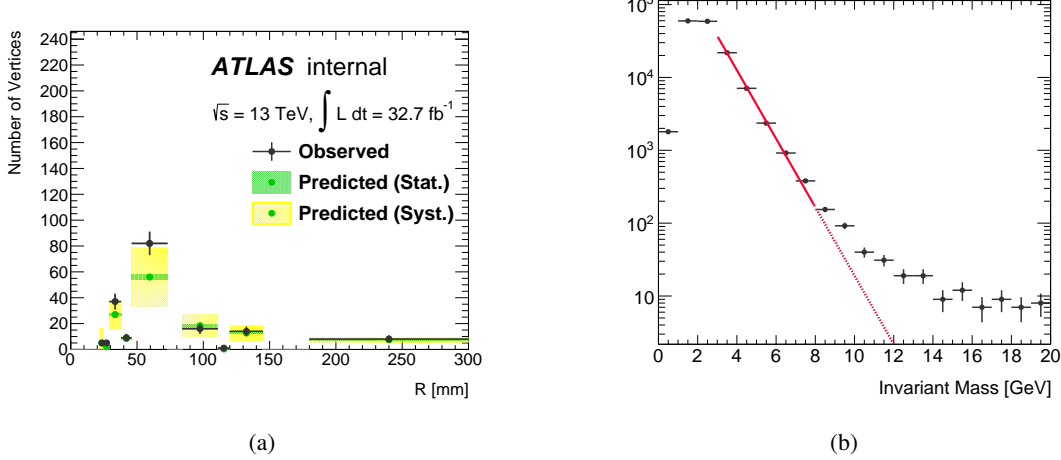


Figure 40: (a) Summary of the observed and expected numbers of 4-track DVs with mass above 10 GeV in the regions with inverted material veto. Region 0, 6 and 10 are excluded in this figure because too tiny volume is vetoed by material map there. (b) The summation of the 4-track  $m_{DV}$  distributions in Figure 38 and 39. The red line represents a fitted exponential function.

Not reviewed, for internal circulation only

Table 8: Total number of estimated background vertices with a mass  $m_{\text{DV}} > 10 \text{ GeV}$  for the vertex selections used in the control, validation and signal regions, using the 2016 full integrated luminosity of  $32.7 \text{ fb}^{-1}$ . The  $(i+1)$  contribution is estimated using the random crossing fraction method, whilst the  $(i+2)$  contribution is obtained from the merged vertices, and the *Pure-N* tracks estimation is evaluated using the hadronic interactions. *Except for the last row, the numbers shown are obtained before applying the event scale factors.*

Vertex Selection	Sub-Region	Background component	Estimated	Observed
CR, 3-track		(2 + 1)-track	$3093 \pm 2$	3093
VRMs, 4-track	VRLM	(3 + 1)-track	$12.6 \pm 0.3 \pm 1.1$	
		(2 + 2)-track	$3.64 \pm 3.64$	
		Pure 4-track	$0.3 \pm 0.9$	
		<i>Sub-Total</i>	$16.5 \pm 3.9$	
		<i>Selection Eff. Corr.</i>	$\cdots \times (56\% \pm 6\%)$	
		<b>Total</b>	<b><math>9 \pm 2</math></b>	<b>9</b>
VRM	VRM	(3 + 1)-track	$137.4 \pm 2.9 \pm 29.8$	
		Pure 4-track	$16 \pm 47$	
		<b>Total</b>	<b><math>153 \pm 55.7</math></b>	<b>177</b>
SR-Like, $\geq 5$ -track	5-tracks	(4 + 1)-track	$1.3 \pm 0.07 \pm 0.12$	
		(2 + 3)-track	$0.01 \pm 0.01$	
		Pure 5-track	$0.9 \pm 2.8$	
		<b>Total</b>	<b><math>2.2 \pm 2.8</math></b>	<b>1</b>
	6-tracks	(5 + 1)-track	$0.37 \pm 0.03 \pm 0.04$	
$\geq 7$ -tracks	$\geq 7$ -tracks	Pure 6-track	$0.18 \pm 0.58$	
		<b>Total</b>	<b><math>0.55 \pm 0.58</math></b>	<b>1</b>
		( $i+1$ )-track	$0.37 \pm 0.03 \pm 0.04$	
		Pure $\geq 7$ -track	$1 \pm 3$	
		<b>Total</b>	<b><math>1.4 \pm 3</math></b>	<b>3</b>
<b>Total</b>			<b><math>4.2 \pm 4.1</math></b>	<b>5</b>
<b>Full SR event &amp; Vertex selection</b>	<i>Event selection transfer factor</i>		$\cdots \times [4.77 \pm 2.39] \times 10^{-3}$	
	<b>Total</b>		<b><math>0.02 \pm 0.02</math></b>	<b>0</b>

Not reviewed, for internal circulation only

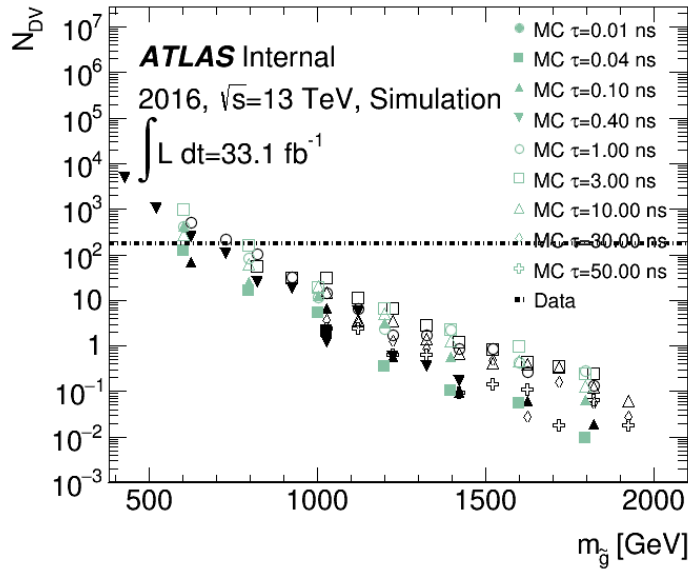


Figure 41: Yields of data and  $R$ -hadron pair production events in the additional VR with inverted material veto requirement. The horizontal dashed line represents the yield of data. The black markers show event yield of each sample with the neutralino mass of 100 GeV. The green markers show event yield of each sample but the neutralino mass is not 100 GeV.

807 The steps above are summarized in Eq. 4.

$$\begin{aligned}
 N_{SR}^{Events} &= N_{Base}^{DV} \times \frac{N_{Full}^{Event}}{N_{Base}^{Event}} \times \left( \frac{N_{Full}^{DV}}{N_{Full}^{Event}} \right)^{-1} \\
 &\approx N_{Base}^{DV} \times \frac{N_{Full}^{Event}}{N_{Base}^{Event}} \times \left( \frac{N_{Base}^{DV}}{N_{Base}^{Event}} \right)^{-1}
 \end{aligned} \tag{4}$$

808 The second factor in Eq. 4 is found to be  $4.77 \times 10^{-3} (\pm 0.02 \times 10^{-3}$  [stat.]). The final factor is found to  
 809 be 1.0. This gives a total scaling factor of  $4.77 \times 10^{-3}$ . The uncertainty on this number is determined to  
 810 be 50% and is discussed in Sect. 6.

811 With this, the final nominal estimate for the number of events in the signal region is

$$\begin{aligned}
 N_{SR}^{Events} &= [4.2 \pm 4.1] \times [4.77 \times 10^{-3} \pm 2.39 \times 10^{-3}] \\
 &= 0.02 \pm 0.02
 \end{aligned} \tag{5}$$

## 812 5.7. Systematic uncertainties on the background estimation

813 Three systematic uncertainties need to be evaluated. These are:

Not reviewed, for internal circulation only

- 814 The crossing fraction: There might enter a source of uncertainty depending on the interval used to estimate  
 815 the crossing fractions. Currently the number of vertices with the mass above 10 GeV is used to normalise  
 816 the CR spectra to the spectra in data for all the twelve regions.
- 817 The shape of the modelled mass spectra: If the shape doesn't perfectly agree with data, an uncertainty on  
 818 the model will enter into the estimation. Both these can be estimated by varying the interval  $\pm 5$  GeV used  
 819 to estimate the crossing fraction. This gives an estimate of how stable the crossing fraction is as well as  
 820 giving an uncertainty of the shape of the model.

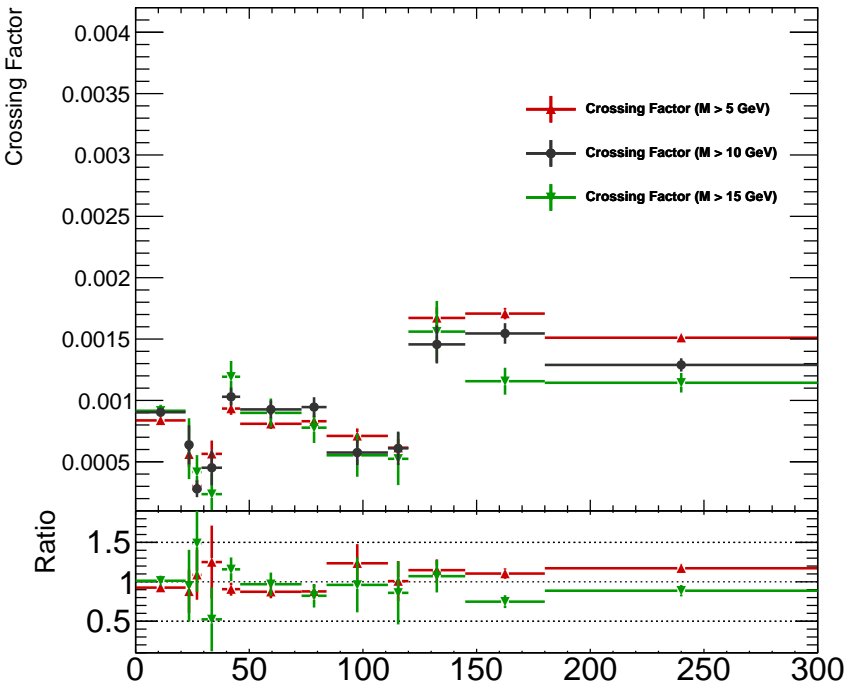


Figure 42: Crossing factors which are derived from different mass intervals for fitting mass template to data in each region in 2016. Black dots show the crossing factors in nominal setting (using data points in  $m_{DV} > 10$  GeV for fitting, red dots are those with  $m_{DV} > 5$  GeV cut, and green dots are those with  $m_{DV} > 15$  GeV cut).

- 821 The last source of uncertainty comes from the event scale factor. Observing how the number of displaced  
 822 vertices per event changes with applied selection gives an estimate of the systematic uncertainty on the  
 823 event scale factor. The degree to which the approximation in Eq. 4 is valid can be quantified by studying  
 824 the double ratio

$$\frac{\frac{N_{Full}^{DV}/N_{Full}^{Event}}{N_{Base}^{DV}/N_{Base}^{Event}}}{\frac{N_{Full}^{DV}/N_{Base}^{Event}}{N_{Full}^{Event}/N_{Base}^{Event}}} = \frac{N_{Full}^{DV}/N_{Base}^{DV}}{N_{Full}^{Event}/N_{Base}^{Event}}. \quad (6)$$

- 825 This double ratio as a function of the amount of the event selection that differs is shown in Figure 43 for  
 826 different DV track multiplicities. The deviation from unity suggests that a 50% uncertainty accounts for  
 827 the degree to which the assumption holds.

Not reviewed, for internal circulation only

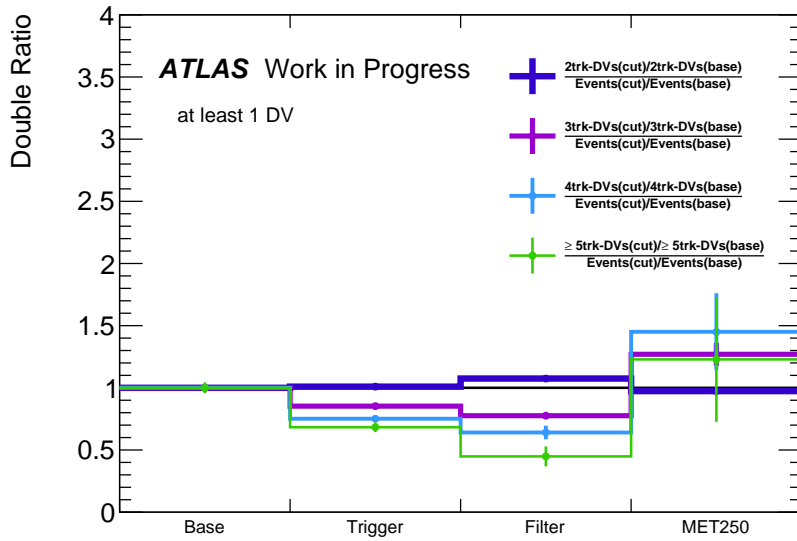


Figure 43: Cut flow showing how the number of displaced vertices per event changes with applied selection.

828 An additional uncertainty comes from the dependence of the third factor in Eq. 4 on the properties of the  
 829 reconstructed DVs. The number of vertices per event as a function of the mass and track multiplicity of  
 830 the vertices is shown in Figure 44.

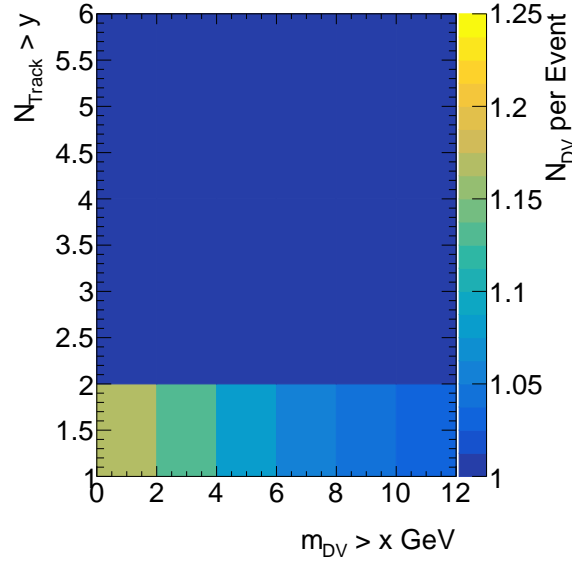


Figure 44: Number of DVs per event as a function of DV mass and track multiplicity.

## 831 6. Systematic uncertainties

### 832 6.1. Uncertainty on tracking and vertexing efficiencies

833 To estimate the systematic uncertainty from the track reconstruction efficiency on the vertex reconstruction, the ratio of  $K_S^0$  yields are compared for a few intervals of decay radii. A deviation from unity for  
 834 this ratio can be used to approximate the uncertainty in the track reconstruction efficiency in MC. From  
 835 the maximum discrepancy a track-killing factor is derived which is then applied to MC and the vertexing  
 836 algorithm is re-run, to estimate the effect on the vertex reconstruction efficiency. The efficiency-vs- $c\tau$  and  
 837 efficiency-vs- $R$  estimates are then made for the signal samples with the track-killing fraction applied.  
 839

840 The data selected for this study has been obtained from the DRAW\_RPVLL 2016 data sample described  
 841 in section 2.1, in particular runs 297447 and 303201 corresponding to  $6.8 \text{ fb}^{-1}$ . The MC samples used  
 842 are dijet samples presented in section 2.2.2. In order to fairly compare simulation with experimental data,  
 843 the event cuts described in section 3 are applied also in the simulated data. The selection vertex-level  
 844 criteria described in Ref. [33] are used to select the final  $K_S^0$  candidates. After the DRAW selection, zero  
 845 events from the JZ1W and JZ2W samples survive.

846 A fundamental assumption for this method to work is that the data and MC samples are topologically  
 847 and kinematically comparable. Figure 45 shows the transverse momentum and  $\eta$  distribution for the  
 848  $K_S^0$ , as well as the primary vertex  $z$ -distribution. The difference in the distributions are corrected in  
 849 the MC samples by applying a simple 2D weight, to correct for the  $p_T$  and  $\eta$ -distributions, and a 1D  
 850 weight to correct according to the primary vertex  $z$ -distribution in data. After weighting the samples are  
 851 comparable.

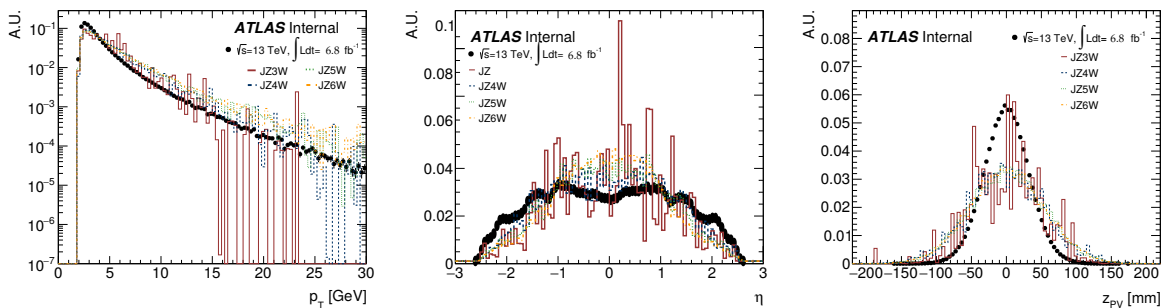


Figure 45: The transverse momentum (left),  $\eta$  (center), and primary vertex  $z$  (right) distributions of the  $K_S$  for the different JZ\*W samples and data. The weights used to re-weight the MC samples are derived from these distributions.

852 The number of  $K_S^0$  candidates found in each interval of decay length, 5-10 mm, 10-15 mm, 15-25 mm  
 853 and 25-40 mm, are counted using a fit. The fit function is a combination of a double Gaussian for the  
 854 signal and a polynomial function for the background. Figure 46 show the fit for MC and data in the barrel  
 855 region and for the interval 5-10 mm.

856 Since the  $K_S^0$  production rate is not known in MC and data, the samples are individually normalised to the  
 857 amount of  $K_S^0$  seen at the smallest decay lengths. The maximum discrepancy then taken as the maximum

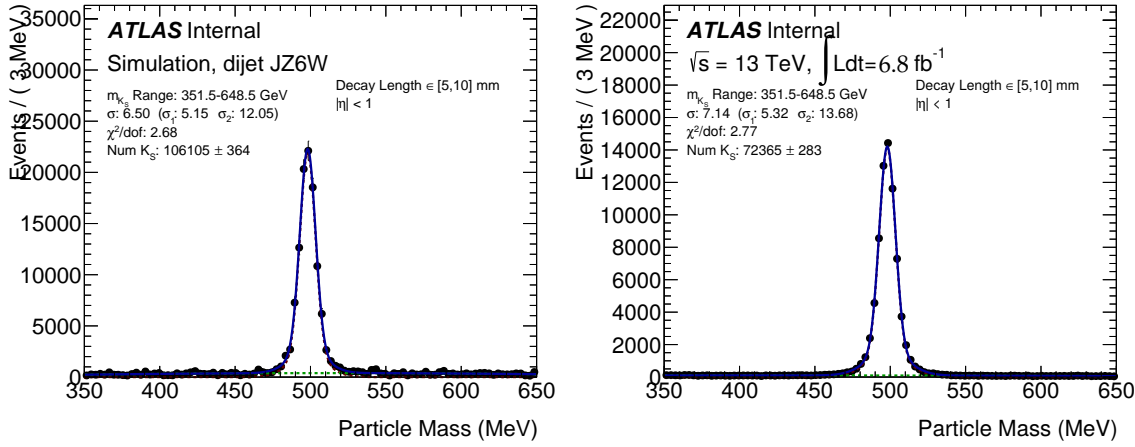


Figure 46: An example of the double Gaussian fit used to count the number of signal  $K_S^0$  on the barrel for the decay length interval 5-10 mm, for MC (left) and data (right). The green line corresponds to the background-function, the red line is the fit for the signal while the blue lines are the combined fit. Using a simultaneous fit, the number of  $K_S^0$  candidates are extracted.

deviation of the double ratio  $\frac{Data_i/MC_i}{Data_0/MC_0}$ . Figure 47 shows the final result with the ratio for the barrel region ( $|\eta| < 1$ ) and the endcap region ( $|\eta| \geq 1$ ), the maximum discrepancy is taken to be 10% in the barrel and 20% in the endcap. The inefficiency to reconstruct  $K_S^0$  as a function of the inefficiency in tracking can be calculated as following:

$$(1 - \epsilon_{K_S}) = 2 * (1 - \epsilon_{trk}) - (1 - \epsilon_{trk})^2 \quad (7)$$

The track-killing factor is estimated to the first order as half the value of the maximum deviation from one yielding 5% for  $|\eta| < 1$  and 10% for  $|\eta| \geq 1$ . The signal MC samples are then re-reconstructed, using these values to randomly remove a fraction of tracks before the vertexing step. The analysis is repeated on these ‘‘Track-Killed’’ samples, and the difference between the ‘‘Nominal’’ and ‘‘Track-Killed’’ efficiency-vs-lifetime curves (as described in Section 4.3) is taken as a systematic uncertainty. Figure 48 shows the track killing factor effect over the vertex reconstruction efficiency as a function of the radial position of the displaced vertex for a couple of signal samples.

## 6.2. Uncertainty on $E_T^{\text{miss}}$ selection

We consider the ‘‘standard’’ set of  $E_T^{\text{miss}}$  uncertainties, recommended by the Jet/Etmis CP group. It is possible to obtain the  $E_T^{\text{miss}}$  variations by scaling up and down the contributions from the individual objects, using the METMaker tool. With this we can obtain the standard systematic uncertainty on the new correctly recalculated  $E_T^{\text{miss}}$ . We consider four sources of uncertainties : JES, JER, scale for the soft term and resolution for the soft term. We evaluate the number of events passing our  $E_T^{\text{miss}} > 250$  GeV cut considering the different uncertainties. Since we have an up and down variation for the four of them, we choose the largest contribution between up and down, and the total standard  $E_T^{\text{miss}}$  uncertainty is given by the sum in quadrature of all four contributions. [FIXME: give the results]

Not reviewed, for internal circulation only

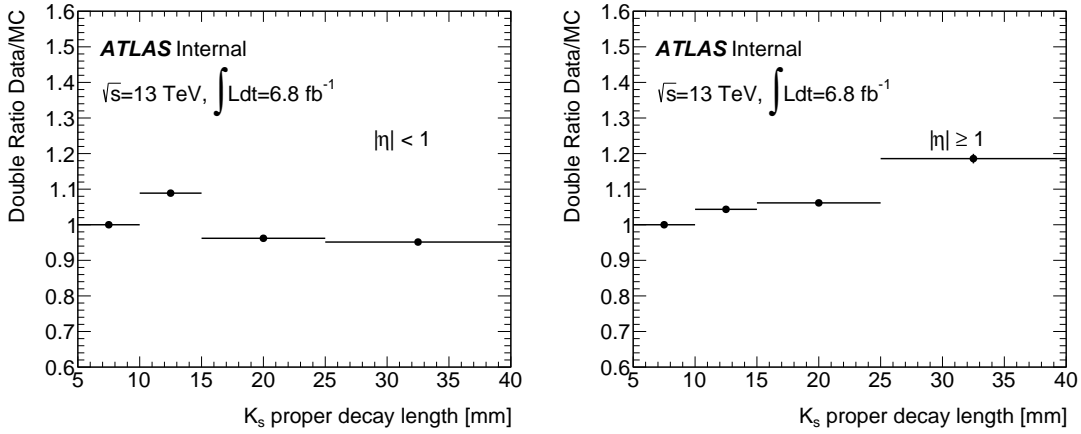


Figure 47: Double ratio of number of  $K_S^0$  found in MC and data individually normalised to the number found at the smallest interval, for the barrel region (left) and endcap (right). The maximum deviation from one is taken as a conservative estimate of the systematic uncertainty from the tracking efficiency.

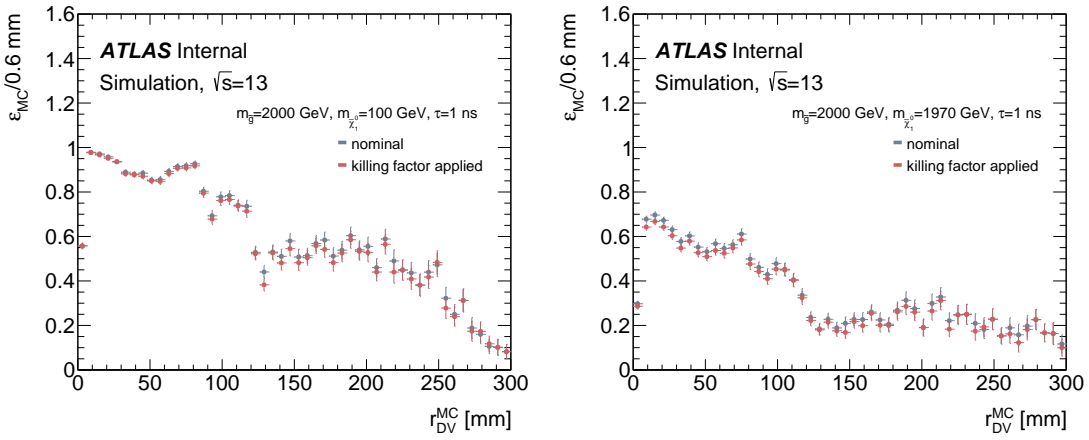


Figure 48: Vertex reconstruction efficiency for two MC signal samples, 402735 (left) and 402739 (right). The blue markers shows the efficiency distribution without the track-killing factor and the red markers are with the track-killing factor applied.

### 878 6.3. Uncertainty on jet selection

879 In order to correct for the fact that some of the jets in our signal samples originate from displaced vertices,  
 880 we apply a systematic uncertainty on the jet  $p_T$ . This uncertainty is obtained by extracting an uncertainty  
 881 on the jet response as a function of the vertex displacement, similarly to what was done for the Run-1  
 882 round of this search [34].

883 **TODO:** The rest of this subsection needs updating. In Run I the jet response varied by  $O(1\%)$  with  
 884 displacement, so this is a subdominant uncertainty for the signal efficiency. We don't expect significantly  
 885 different results for Run II.

886 Figure 49 shows the  $p_T$  response to matched jets against  $r_{DV}$  and  $z_{DV}$ , including a linear polynomial fit.  
 887 The fit function is given by

$$f(x) = p_0 + p_1 x \quad (8)$$

888 where  $x$  can refer to  $r_{DV}$  or  $z_{DV}$ . The parameters of the function for the response against  $r_{DV}$  are  $p_0 =$   
 889  $1.02 \pm 0.001$ ,  $p_1 = 3.89 \times 10^{-5} \pm 1.03 \times 10^{-5}$ , and the ones for the plot against  $z_{DV}$  are  $p_0 = 1.02 \pm 0.002$ ,  
 890  $p_1 = 2.63 \times 10^{-5} \pm 1.56 \times 10^{-5}$



Figure 49: Mean ratio of truth jet  $p_T$ /jet  $p_T$  for matched jets vs  $r_{DV}$  and  $z_{DV}$  for sample 177573, including a linear fit. **TODO:** Need figure (current is only placeholder!).

891 We apply a relative systematic uncertainty to the  $p_T$  of each jet that is matched to a true displaced vertex.  
 892 This uncertainty is given by  $\frac{p_1}{p_0} * r_{DV}$ , where  $r_{DV}$  refers to the true  $r_{DV}$ . In this way we can re-scale such  
 893 that the response would be 1 at zero  $r_{DV}$ .

### 894 6.4. Uncertainty related to ISR

895 Initial State Radiation (ISR) has a direct effect on the signal efficiency. As MadGraph simulate a more  
 896 accurate description of radiative effects, our Pythia6 samples are reweighted to reproduce the distribution  
 897 of  $p_T(\tilde{g}\tilde{g})$  from equivalent MadGraph samples. The difference between the two generators is then used as  
 898 a (most likely conservative) estimate of the uncertainty on the modelling of ISR. The seven MC samples  
 899 listed in 2.2.2 are compared to signal  $R$ -hadron samples: 372451, 372453, 372456, 372460, 372466,  
 900 372472 and 372478. Each setup have a gluino mass of 600, 800, 1000, 1200, 1400, 1600 or 1800 GeV,

901 respectively. To estimate the systematic uncertainties, the vector sum of the  $p_T$  of the gluino-gluino  
 902 system in both the  $R$ -hadron and the MadGraph samples are compared as can be seen in the left plot of  
 903 Figure 50 for a gluino mass of 1400 GeV. This shows that Pythia predicts less radiation. The right figure  
 904 shows a weight function extracted by taking the ratio of the left plot (done separately for all mass points).  
 905 The event weights are then applied to the Pythia6  $R$ -hadron signal MC events in the nominal processing.  
 906 The effect of ISR systematic varies between different mass points and goes up to 30%. The efficiency for  
 907 samples with smaller amount of  $E_T^{\text{miss}}$  from the neutralino are more sensitive to the uncertainty on the  
 908 ISR modelling.

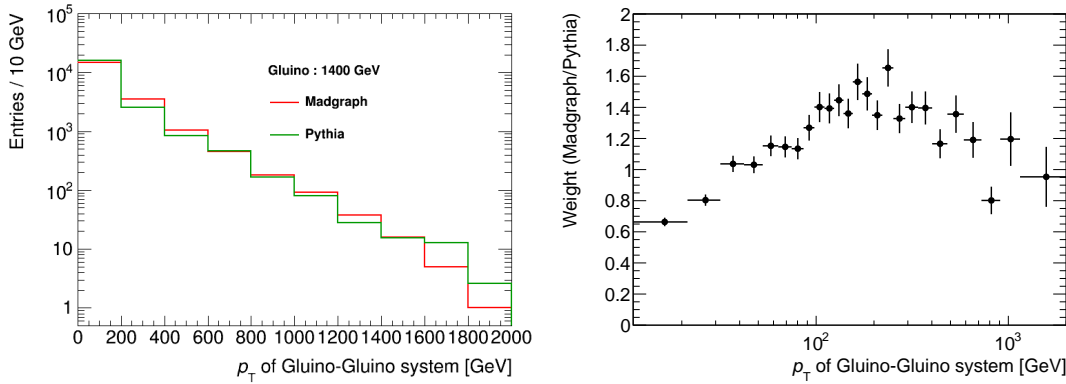


Figure 50: (Left) A vector summation of the transverse momentum for the gluino-gluino system with 1400 GeV  $R$ -hadron for Pythia (402720) in green and a MadGraph sample (372466). (Right) A weight computed taking the ratio of the both samples.

## 909 6.5. Uncertainty due to pileup re-weighting

910 We use the standard ATLAS pileup re-weighting tool to weight MC events such that the distribution of  
 911  $\mu$ , the average number of  $pp$  interactions per bunch crossing, matches that in the data. In this procedure,  
 912 the event weights are obtained from the distributions of the  $\mu$  observed in data. We vary this  $\pm 1\sigma$  around  
 913 the mean value,  $\langle \mu \rangle$ , of the  $\mu$ -distribution in order to obtain distributions for the up and down variations.  
 914 The re-weighting procedure is applied using those distributions, taking the yield differences with respect  
 915 to the nominal  $\mu$ -distribution as systematic of the pileup re-weighting.

## 916 6.6. Summary of uncertainties on the efficiency

917 Figure 52 shows the different contributions to the uncertainty on the efficiency-vs- $c\tau$ . The dominant  
 918 uncertainty at small lifetimes is statistical, as a result of our re-weighting procedure (only events with  
 919 DVs decaying at small  $ct_{true}$  have significant contributions). Note that in our simulated  $R$ -hadron signals  
 920 samples, we only have 10k or 20k events per sample. [N.B. extracted from Run-1, we expect similar  
 921 behaviour].

922 Since many of the systematic uncertainties (such as that associated with changing the scale factor for the  
 923 pileup re-weighting) are evaluated by looking at the difference between the “nominal” efficiency-vs- $c\tau$   
 924 and the efficiency-vs- $c\tau$  curve after some change (e.g. JES variation), there is a statistical component to

Not reviewed, for internal circulation only

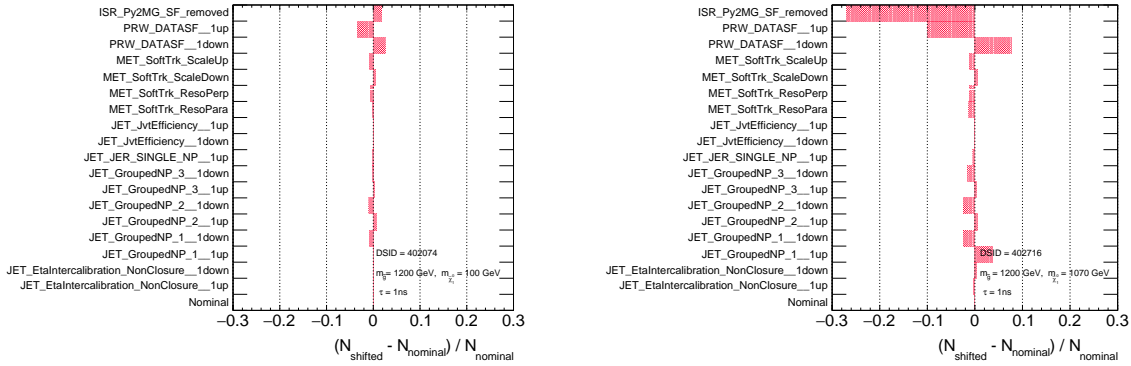


Figure 51: Pulls of the number of events passing the whole selections between nominal and shifted  $1\sigma$  of each systematic source. The left plot is of a signal sample of DSID= 402074 with gluino mass of 1200 GeV, the LSP mass of 100 GeV, R-hadron life time of 1 ns, while the right plot is of that of DSID= 402716 with gluino mass of 1200 GeV, the LSP mass of 1070 GeV, R-hadron life time of 1 ns. Since the efficiency of a compressed scenario is significantly gained by ISR effect, the dominant uncertainty source is ISR weighting from Pythia to MadGraph when the mass difference between gluino and the LSP is small.

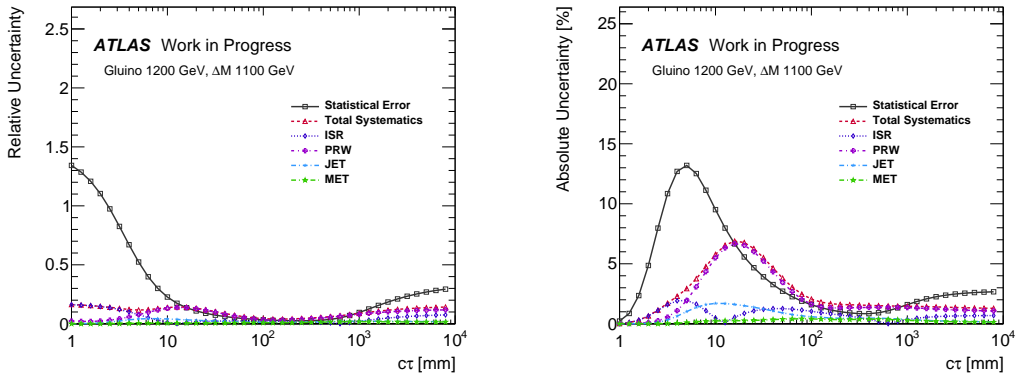


Figure 52: Contributions to the uncertainty on efficiency vs lifetime for a sample with 1200 GeV gluino and 100 GeV LSP. The left plots are the relative uncertainties and the right plots are the absolute uncertainties. **TODO: Need to add tracking uncertainty.**

925 these systematic uncertainties, again, particularly at very small or very large lifetimes where individual  
926 events can have large weights.

927 In addition to the statistical uncertainty which dominates at small lifetimes, the ISR-related uncertainty  
928 is also large in some cases, as a larger boost arising from the recoil against an ISR jet can increase the  
929 fraction of events passing the jet or  $E_T^{\text{miss}}$  cuts. At large lifetimes, the uncertainty associated with the  
930 lifetime re-weighting can also be seen in Figure 52.

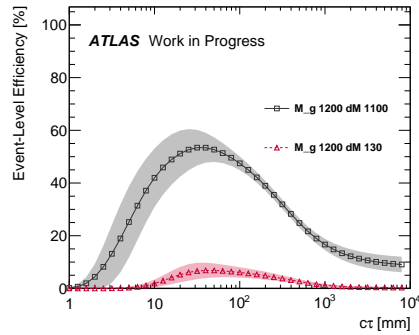


Figure 53: Efficiency vs proper decay length for the  $qq$   $R$ -hadron samples with 1200 GeV gluino and 100 GeV or 1070 GeV neutralinos. All systematic corrections and uncertainties are included. **TODO: Need to add tracking uncertainty.**

**931 6.7. Signal efficiency vs lifetime including all systematic uncertainty**

**932** Figures 53 show the efficiency-vs-proper-decay-length distribution for all  $R$ -hadron samples. All system-  
**933** atic uncertainties are included.

## 934 7. Results

935 This section is a bit sparse for now, but it contains the main results.

### 936 7.1. Final yields

937 With an estimated background of  $0.02 \pm 0.02$  events in the signal region, 0 events are observed in the  
938 data. The observation is consistent with the background-only hypothesis.

### 939 7.2. Distributions

940 1D distributions of the vertex mass and track multiplicity are shown in Figure 54 for vertices in events  
941 that pass the event selection. These vertices are required to have all the final selection criteria except for  
942 the mass and track multiplicity requirements.

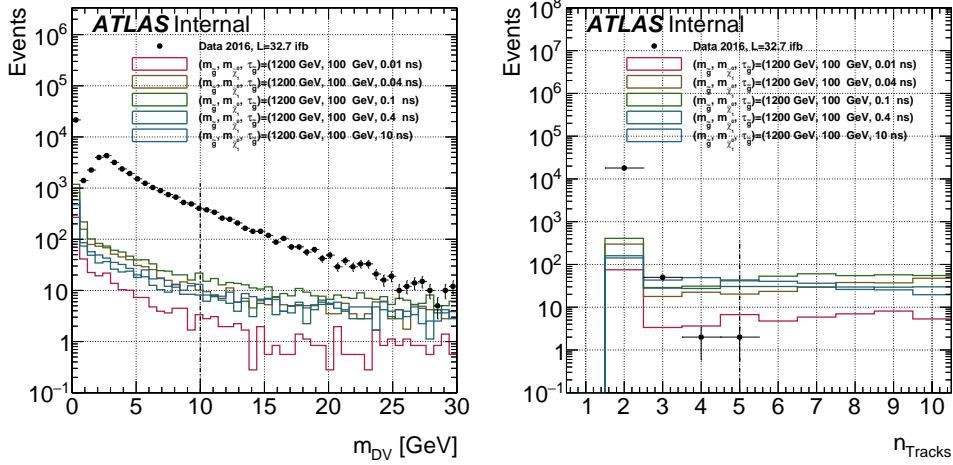


Figure 54: The distributions of vertex mass and track multiplicity are shown for various signals and data. Values are normalized to  $32.7 \text{ fb}^{-1}$ . The values of the signal region requirements are shown in the dashed lines. The track multiplicity distribution requires vertices to have a mass of at least 3 GeV.

943 2D distributions of the vertex mass and track multiplicity observed in data and expected from various  
944 signal models are shown in Figure 55 for various signal lifetimes and Figure 56 for various mass split-  
945 tings.

946 The spatial distributions of the vertex candidates are shown in Figure 58 for those events that fall in VRLM  
947 as well as for the signal region excluding the requirement on the vertex mass and track multiplicity. This  
948 loosened selection is shown since the signal region for this search yields 0 events.

Not reviewed, for internal circulation only

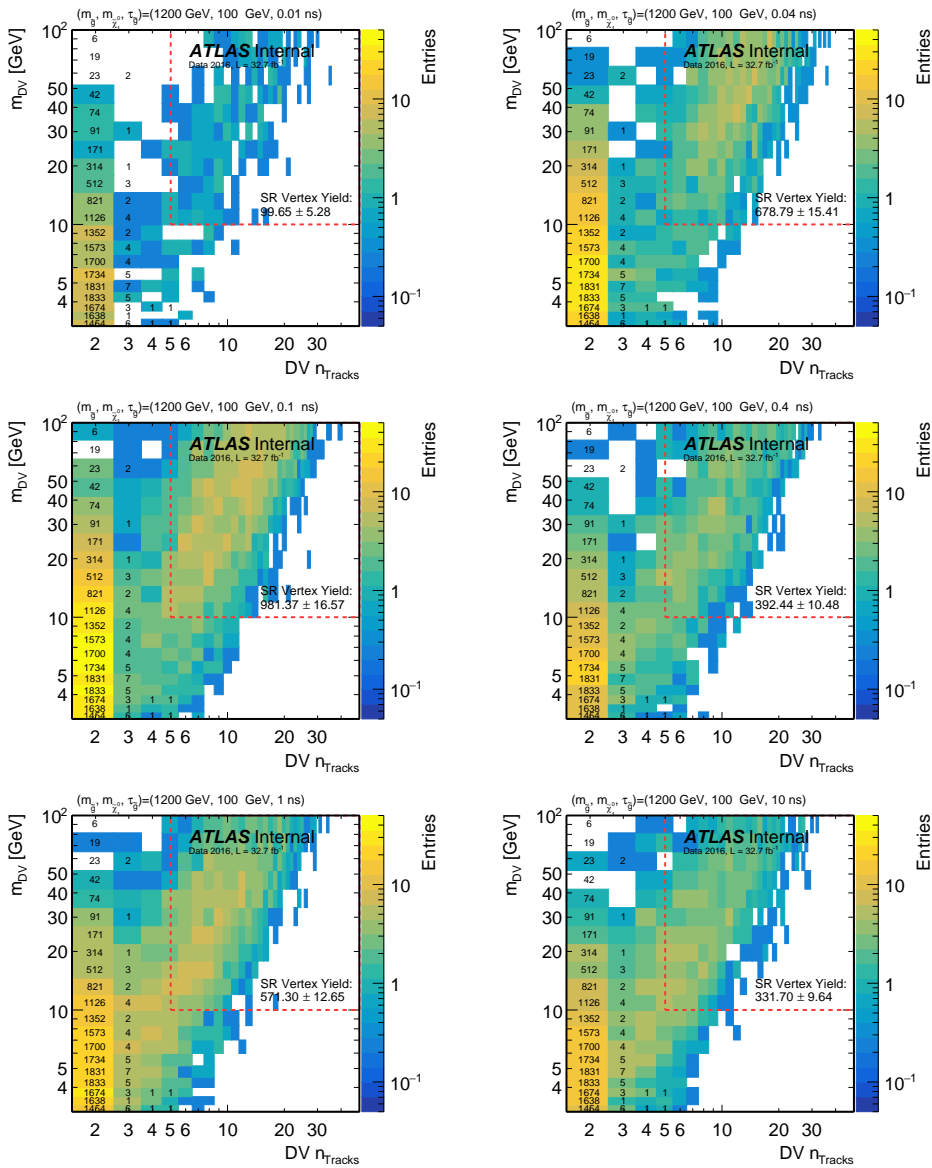


Figure 55: The distribution of vertex mass vs. track multiplicity is shown for various  $R$ -hadron lifetimes. The observed yields in data are overlaid. The yields are normalized to  $32.7 \text{ fb}^{-1}$ .

Not reviewed, for internal circulation only

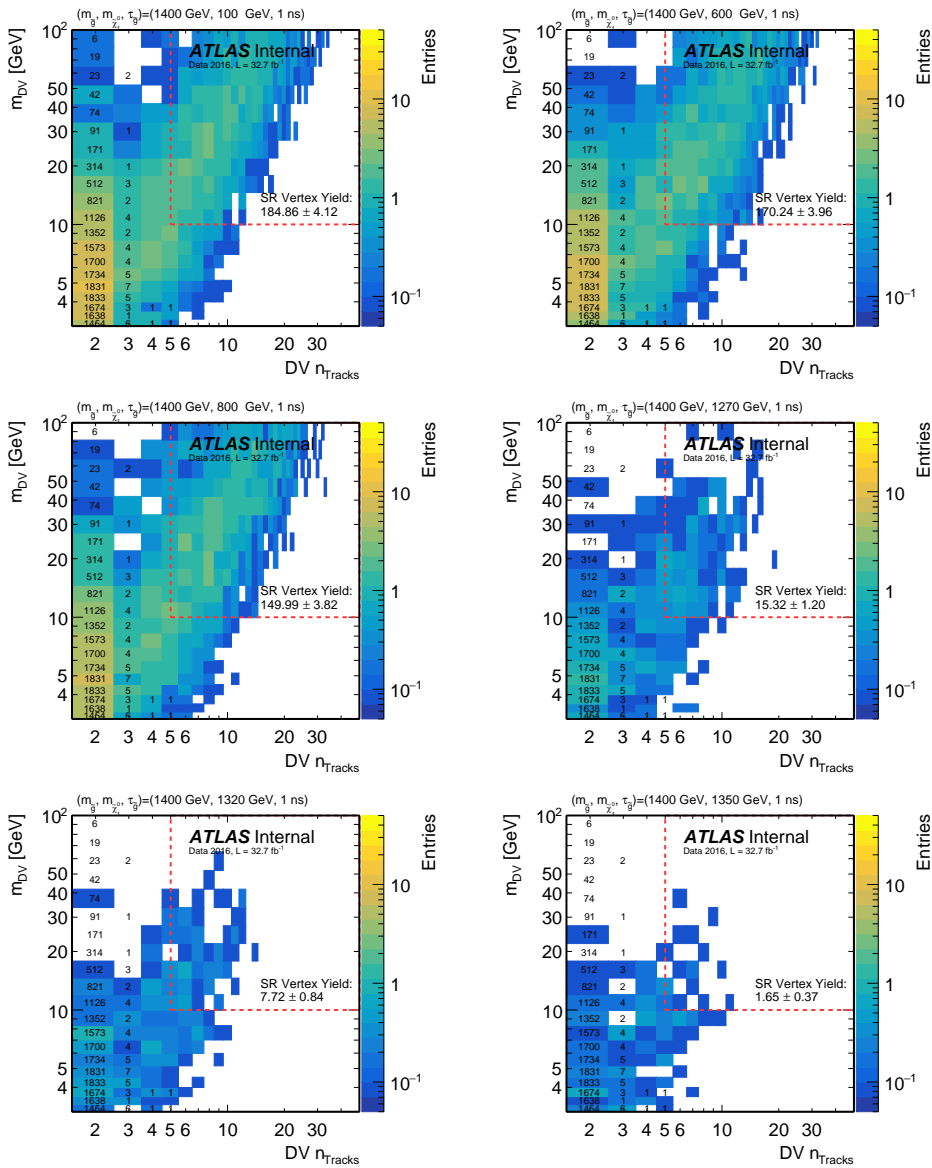


Figure 56: The distribution of vertex mass vs. track multiplicity is shown for various gluino-neutralino mass splittings. The observed yields in data are overlaid. The yields are normalized to  $32.7 \text{ fb}^{-1}$ .

Not reviewed, for internal circulation only

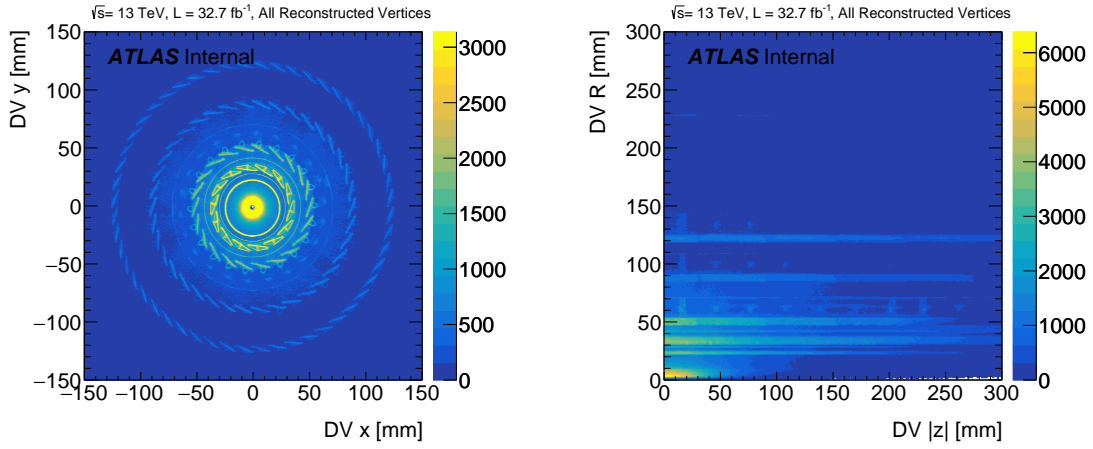


Figure 57: The positions of reconstructed vertices shown in data. Only the vertex fit quality requirements are applied. On the left, a projection to the transverse plane is shown, while on the right, a projection to the  $z$ - $R$  plane is shown. Regions dominated by detector material are clearly visible.

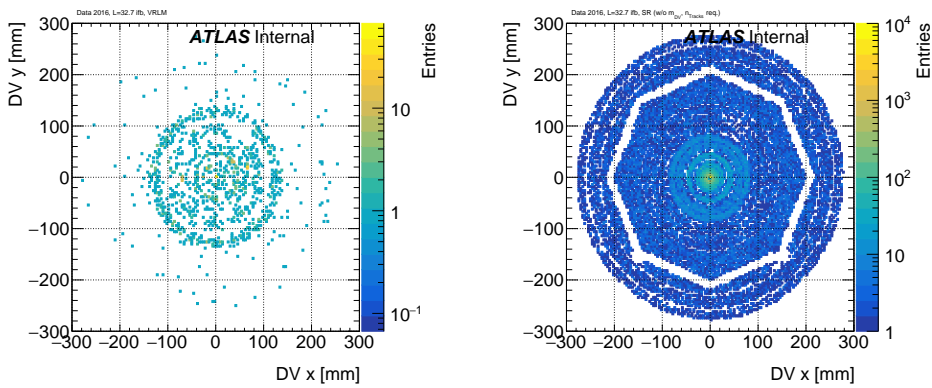


Figure 58: The spatial distributions of displaced vertex candidates are shown in data for the VRLM validation region (left) as well as for the signal region (right) excluding the requirements on the vertex mass and track multiplicity.

## 949 8. Interpretation of results

950 Model independent limits are shown in Table 9.

951 The results are interpreted in the context of the Split-SUSY models (see Section. 1). At the moment there  
 952 is work ongoing to finalize these plots, but what's shown here at the moment is already representative and  
 953 indicative of the main results.

954 The final yields for all regions used in this analysis can be found in Table 10. The observed yields are  
 955 consistent with the background expectation for the validation regions where vrlm contains 9 vertices  
 956 ( $9 \pm 2$  expected) and vrm contains 177 vertices ( $150 \pm 60$  expected). The two-dimensional distribution of  
 957  $m_{\text{DV}}$  and track multiplicity is shown for events that satisfy the full event-level selection in Fig. 59. The  
 958 final SR yields are highlighted, with 0 events observed ( $0.02 \pm 0.02$  expected) in  $32.7 \text{ fb}^{-1}$  of data from  
 959 2016.

960 In the absence of a statistically significant excess in the data, exclusion limits are placed on  $R$ -hadron mod-  
 961 els. These 95% confidence-level (CL) upper limits are calculated using the  $CL_s$  prescription [0954-3899-28-10-313]  
 962 with the profile likelihood used as the test statistic, using the HistFitter [Baak:2014wma] framework with

Signal channel	$\langle \epsilon \sigma \rangle_{\text{obs}}^{95} [\text{fb}]$	$S_{\text{obs}}^{95}$	$S_{\text{exp}}^{95}$	$CL_B$	$p(s = 0) (Z)$
SR	0.09	3.072	$3.015^{+0.017}_{-0.009}$	0.14	0.32 (0.46)

Table 9: Left to right: 95% CL upper limits on the visible cross section ( $\langle \epsilon \sigma \rangle_{\text{obs}}^{95}$ ) and on the number of signal events ( $S_{\text{obs}}^{95}$ ). The third column ( $S_{\text{exp}}^{95}$ ) shows the 95% CL upper limit on the number of signal events, given the expected number (and  $\pm 1\sigma$  excursions on the expectation) of background events. The last two columns indicate the  $CL_B$  value, i.e. the confidence level observed for the background-only hypothesis, and the discovery  $p$ -value ( $p(s = 0)$ ).

Table 10: The observed number of vertices for the control and validation regions are shown along with the back-  
 ground expectations for the  $32.7 \text{ fb}^{-1}$  of data. The last row shows the expected and observed signal region event  
 yields.

Selection	Sub-Region	Estimated	Observed
<i>Event pre-selection</i> $n_{\text{trk}} = 3, m_{\text{DV}} > 10 \text{ GeV}$			3093
<i>Event pre-selection</i> $n_{\text{trk}} = 4, m_{\text{DV}} > 10 \text{ GeV}$	VRLM	<b><math>9 \pm 2</math></b>	<b>9</b>
	VRM	<b><math>150 \pm 60</math></b>	<b>177</b>
	5-tracks	<b><math>2.2 \pm 2.8</math></b>	<b>1</b>
<i>Event pre-selection</i> $n_{\text{trk}} \geq 5, m_{\text{DV}} > 10 \text{ GeV}$	6-tracks	<b><math>0.6 \pm 0.6</math></b>	<b>1</b>
	$\geq 7$ -tracks	<b><math>1 \pm 3</math></b>	<b>3</b>
	<b>Total</b>	<b><math>4.2 \pm 4.1</math></b>	<b>5</b>
<b>Full SR selection</b>	<b>Total</b>	<b><math>0.02 \pm 0.02</math></b>	<b>0</b>

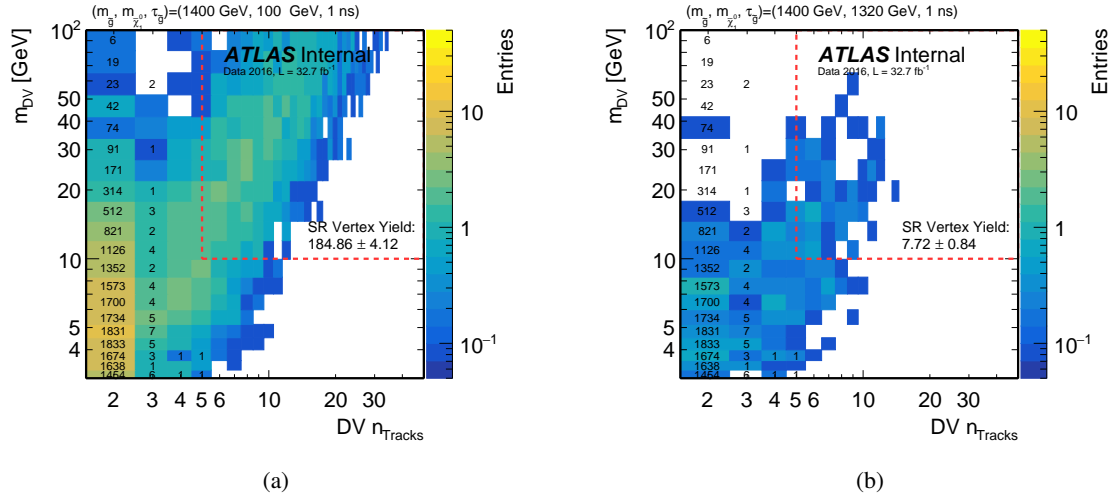


Figure 59: Two-dimensional distributions of  $m_{DV}$  and track multiplicity are shown for DVs in events that satisfy all signal region event selection criteria. Drawn numbers correspond to the observations in data, while the colour-representation shows example distributions for two  $R$ -hadron signals used as benchmark models in this search. The dashed line represents the boundary of the signal region requirements.

963 pseudo-experiments. Upper limits on the cross section for gluino pair-production as a function of gluino  
 964 lifetime are shown in Fig. 60 for some example values of  $m_{\tilde{g}}$  and  $m_{\tilde{\chi}_1^0} = 100$  GeV. Also shown are  
 965 the signal production cross sections for these gluino masses. Reduced signal selection efficiencies for  
 966 low- $\Delta m$  samples result in less stringent cross section limits. For  $\Delta m = 100$  GeV, the limits are shown  
 967 in Fig. 61. Upper limits on the gluino mass are also shown as a function of gluino lifetime in Figs. 60  
 968 and 61. DV-level fiducial volume and PV-distance requirements reduce the exclusion power in the high  
 969 and low extremes of gluino lifetime. Similarly, for a fixed gluino lifetime of  $\tau = 1$  ns, 95% CL exclusion  
 970 curves are shown as a function of  $m_{\tilde{g}}$  and  $m_{\tilde{\chi}_1^0}$  in Fig. 62. For  $m_{\tilde{\chi}_1^0} = 100$  GeV, gluino masses are excluded  
 971 below 2.29 TeV at  $\tau = 1$  ns and below 2.37 TeV at around  $\tau = 0.17$  ns.

Not reviewed, for internal circulation only

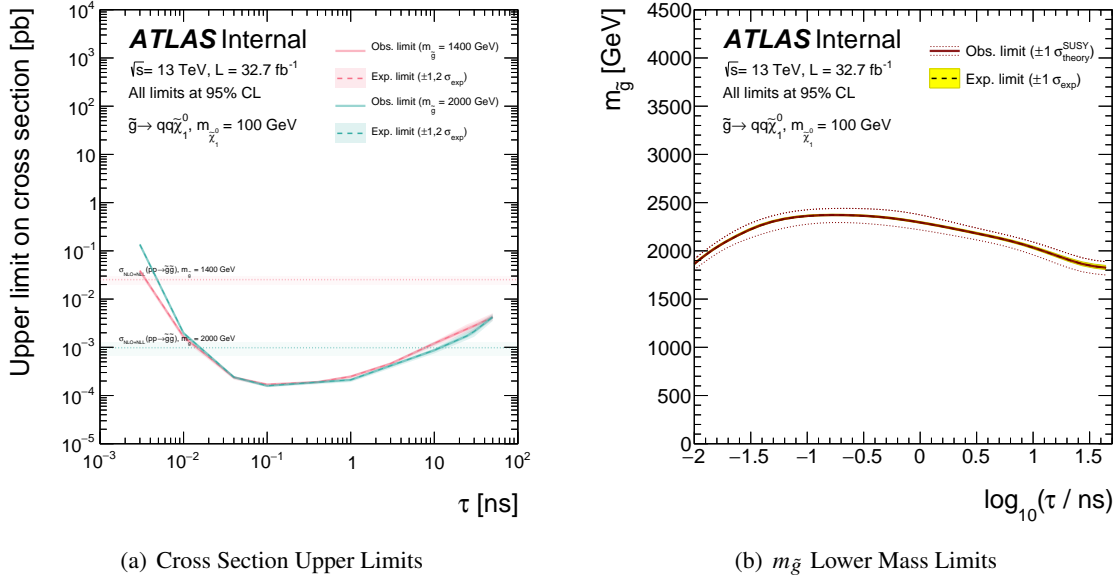


Figure 60: 95% CL upper limits on the signal cross section are shown in (a) for fixed  $m_{\chi_1^0} = 100 \text{ GeV}$  as a function of lifetime  $\tau$ . Horizontal lines denote the  $\bar{g}\bar{g}$  production cross section for various values of  $m_{\bar{g}}$ . The lower limit on  $m_{\bar{g}}$  for fixed  $m_{\chi_1^0} = 100 \text{ GeV}$  as a function of lifetime  $\tau$  is shown in (b).

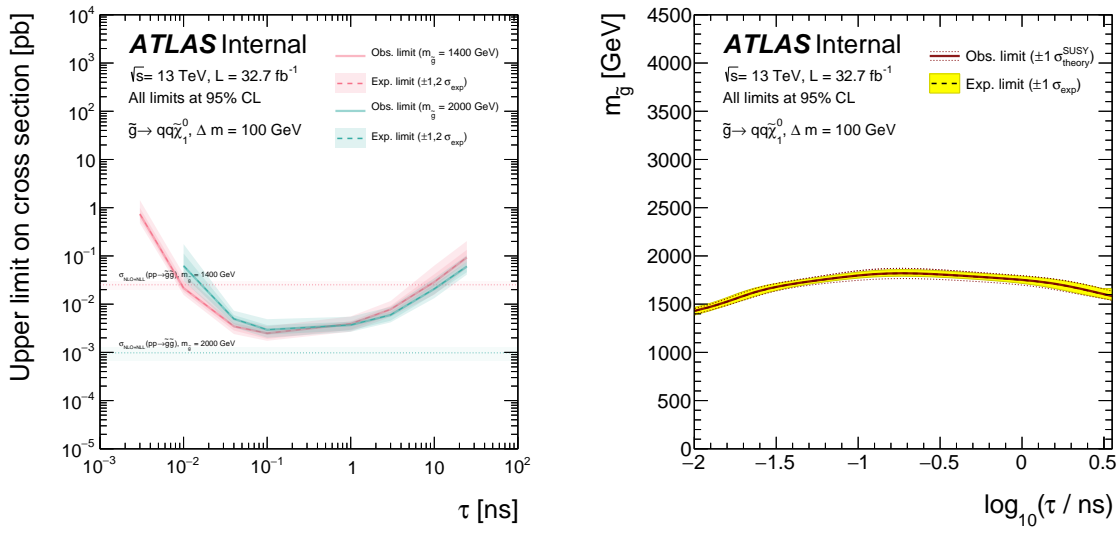


Figure 61: 95% CL upper limits on the signal cross section are shown in (a) for fixed  $\Delta m = 100 \text{ GeV}$  as a function of lifetime  $\tau$ . Horizontal lines denote the  $\bar{g}\bar{g}$  production cross section for various values of  $m_{\bar{g}}$ . The lower limit on  $m_{\bar{g}}$  for fixed  $\Delta m = 100 \text{ GeV}$  as a function of lifetime  $\tau$  is shown in (b).

Not reviewed, for internal circulation only

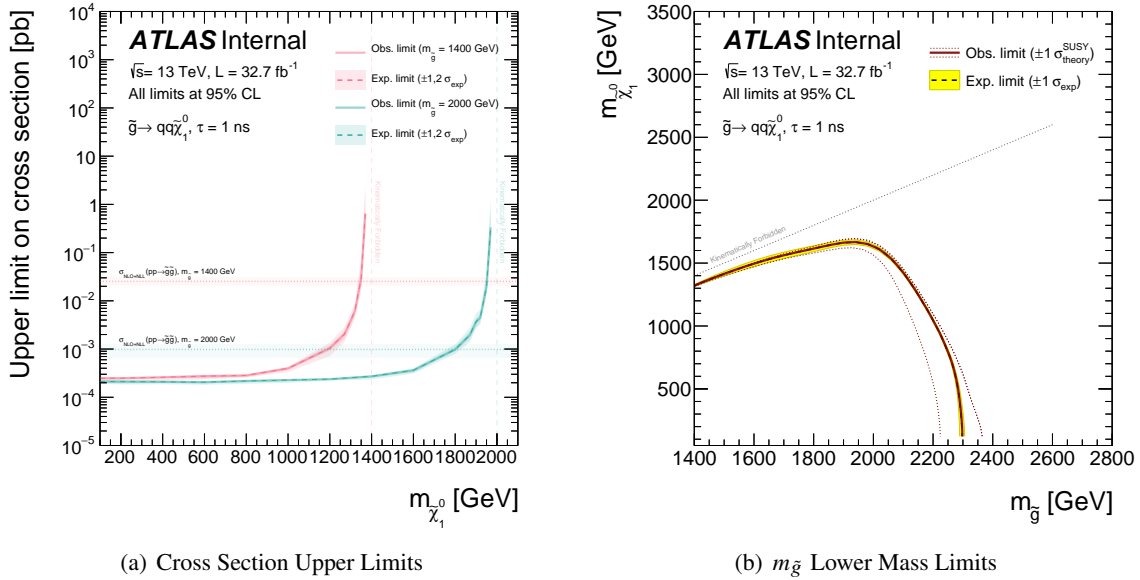


Figure 62: 95% CL upper limits on the signal cross section are shown in (a) for fixed  $\tau = 1$  ns as a function of  $m_{\tilde{\chi}_1^0}$ . Horizontal lines denote the  $\tilde{g}\tilde{g}$  production cross section for various values of  $m_{\tilde{g}}$ . The 95% CL limit as a function of  $m_{\tilde{g}}$  and  $m_{\tilde{\chi}_1^0}$  is shown in (b) for fixed  $\tau = 1$  ns.

## 9. Conclusions

A search for physics beyond the Standard Model with displaced-vertex signatures has been performed using the 2016  $pp$  dataset at  $\sqrt{s} = 13$  TeV corresponding to an integrated luminosity of  $33.1 \text{ fb}^{-1}$ . The search is sensitive to signals producing vertices with  $n_{\text{track}} \geq 5$  and  $m_{\text{DV}} > 10 \text{ GeV}$  inside the fiducial volume defined by  $r_{\text{DV}} < 300 \text{ mm}$ ,  $|z_{\text{DV}}| < 300 \text{ mm}$ . With an expected background of  $0.2 \pm 0.2$  events, 0 events were observed in the signal region. The observation was therefore found to be consistent with the background-only hypothesis, and exclusion limits were calculated for the sought signals.

979 **Appendix**

[Not reviewed, for internal circulation only]

980 **A. Samples details**

[Not reviewed, for internal circulation only]

Table 11: The parameter values for the decaying  $R$ -hadron signal MC samples from  $m_{\tilde{g}} = 600$  GeV to 1200 GeV used in this work to obtain the gluino-neutralino mass plane at fixed  $\tau = 1$  ns. Production cross section (calculated following the prescription in [35]).

DS number	Model	Production mass [GeV]	Produced particle mass [GeV]	LLP decay channel	LSP mass [GeV]	$\tau$ [ns]	$<\beta\gamma>$	$\sigma$ [pb]	Num generated
402700	Split SUSY	$\tilde{g}$	600	$\tilde{g} \rightarrow qq + \chi_1^0$	100	1	1.15	9.22	9k
402701	Split SUSY	$\tilde{g}$	600	$\tilde{g} \rightarrow qq + \chi_1^0$	470	1	1.14	9.22	9k
402702	Split SUSY	$\tilde{g}$	600	$\tilde{g} \rightarrow qq + \chi_1^0$	520	1	1.16	9.22	9k
402703	Split SUSY	$\tilde{g}$	600	$\tilde{g} \rightarrow qq + \chi_1^0$	550	1	1.15	9.22	10k
402704	Split SUSY	$\tilde{g}$	600	$\tilde{g} \rightarrow qq + \chi_1^0$	570	1	1.15	9.22	9k
402705	Split SUSY	$\tilde{g}$	800	$\tilde{g} \rightarrow qq + \chi_1^0$	100	1	0.98	1.49	10k
402706	Split SUSY	$\tilde{g}$	800	$\tilde{g} \rightarrow qq + \chi_1^0$	670	1	1.01	1.49	9k
402707	Split SUSY	$\tilde{g}$	800	$\tilde{g} \rightarrow qq + \chi_1^0$	720	1	1.00	1.49	10k
402708	Split SUSY	$\tilde{g}$	800	$\tilde{g} \rightarrow qq + \chi_1^0$	750	1	1.00	1.49	9k
402709	Split SUSY	$\tilde{g}$	800	$\tilde{g} \rightarrow qq + \chi_1^0$	770	1	1.01	1.49	9k
402710	Split SUSY	$\tilde{g}$	1000	$\tilde{g} \rightarrow qq + \chi_1^0$	100	1	0.89	0.325	10k
402711	Split SUSY	$\tilde{g}$	1000	$\tilde{g} \rightarrow qq + \chi_1^0$	870	1	0.90	0.325	10k
402712	Split SUSY	$\tilde{g}$	1000	$\tilde{g} \rightarrow qq + \chi_1^0$	920	1	0.89	0.325	9k
402713	Split SUSY	$\tilde{g}$	1000	$\tilde{g} \rightarrow qq + \chi_1^0$	950	1	0.90	0.325	9k
402714	Split SUSY	$\tilde{g}$	1000	$\tilde{g} \rightarrow qq + \chi_1^0$	970	1	0.90	0.325	8.5k
402715	Split SUSY	$\tilde{g}$	1200	$\tilde{g} \rightarrow qq + \chi_1^0$	100	1	0.82	0.0856	10k
402716	Split SUSY	$\tilde{g}$	1200	$\tilde{g} \rightarrow qq + \chi_1^0$	1070	1	0.83	0.0856	9.8k
402717	Split SUSY	$\tilde{g}$	1200	$\tilde{g} \rightarrow qq + \chi_1^0$	1120	1	0.82	0.0856	9.8k
402718	Split SUSY	$\tilde{g}$	1200	$\tilde{g} \rightarrow qq + \chi_1^0$	1150	1	0.82	0.0856	9.4k
402719	Split SUSY	$\tilde{g}$	1200	$\tilde{g} \rightarrow qq + \chi_1^0$	1170	1	0.82	0.0856	9.8k

Not reviewed, for internal circulation only

Table 12: The parameter values for the decaying  $R$ -hadron signal MC samples  $m_{\tilde{g}} = 1400$  GeV to 2000 GeV used in this work to obtain the gluino-neutralino mass plane at fixed lifetime of  $\tau = 1 \text{ ns}$ . Production cross section (calculated following the prescription in [35]).

DS number	Model	Production mass [GeV]	Produced particle mass [GeV]	LLP decay channel	LSP mass [GeV]	$\tau$ [ns]	$<\beta\gamma>$	$\sigma$ [pb]	Num generated
402720	Split SUSY	$\tilde{g}$	1400	$\tilde{g} \rightarrow qq + \tilde{\chi}_1^0$	100	1	0.75	0.0253	9k
402721	Split SUSY	$\tilde{g}$	1400	$\tilde{g} \rightarrow qq + \tilde{\chi}_1^0$	1270	1	0.75	0.0253	8.8k
402722	Split SUSY	$\tilde{g}$	1400	$\tilde{g} \rightarrow qq + \tilde{\chi}_1^0$	1320	1	0.76	0.0253	9k
402723	Split SUSY	$\tilde{g}$	1400	$\tilde{g} \rightarrow qq + \tilde{\chi}_1^0$	1350	1	0.75	0.0253	10k
402724	Split SUSY	$\tilde{g}$	1400	$\tilde{g} \rightarrow qq + \tilde{\chi}_1^0$	1370	1	0.75	0.0253	10k
402725	Split SUSY	$\tilde{g}$	1600	$\tilde{g} \rightarrow qq + \tilde{\chi}_1^0$	100	1	0.70	0.00809	10k
402726	Split SUSY	$\tilde{g}$	1600	$\tilde{g} \rightarrow qq + \tilde{\chi}_1^0$	1470	1	0.70	0.00809	9k
402727	Split SUSY	$\tilde{g}$	1600	$\tilde{g} \rightarrow qq + \tilde{\chi}_1^0$	1520	1	0.70	0.00809	10k
402728	Split SUSY	$\tilde{g}$	1600	$\tilde{g} \rightarrow qq + \tilde{\chi}_1^0$	1550	1	0.69	0.00809	9k
402729	Split SUSY	$\tilde{g}$	1600	$\tilde{g} \rightarrow qq + \tilde{\chi}_1^0$	1570	1	0.70	0.00809	9k
402730	Split SUSY	$\tilde{g}$	1800	$\tilde{g} \rightarrow qq + \tilde{\chi}_1^0$	100	1	0.65	0.00276	9k
402731	Split SUSY	$\tilde{g}$	1800	$\tilde{g} \rightarrow qq + \tilde{\chi}_1^0$	1670	1	0.65	0.00276	9k
402732	Split SUSY	$\tilde{g}$	1800	$\tilde{g} \rightarrow qq + \tilde{\chi}_1^0$	1720	1	0.64	0.00276	8.8k
402733	Split SUSY	$\tilde{g}$	1800	$\tilde{g} \rightarrow qq + \tilde{\chi}_1^0$	1750	1	0.65	0.00276	9k
402734	Split SUSY	$\tilde{g}$	1800	$\tilde{g} \rightarrow qq + \tilde{\chi}_1^0$	1770	1	0.65	0.00276	9k
402735	Split SUSY	$\tilde{g}$	2000	$\tilde{g} \rightarrow qq + \tilde{\chi}_1^0$	100	1	0.61	0.000980	9.8k
402736	Split SUSY	$\tilde{g}$	2000	$\tilde{g} \rightarrow qq + \tilde{\chi}_1^0$	1870	1	0.61	0.000980	9k
402737	Split SUSY	$\tilde{g}$	2000	$\tilde{g} \rightarrow qq + \tilde{\chi}_1^0$	1920	1	0.61	0.000980	9k
402738	Split SUSY	$\tilde{g}$	2000	$\tilde{g} \rightarrow qq + \tilde{\chi}_1^0$	1950	1	0.61	0.000980	10k
402739	Split SUSY	$\tilde{g}$	2000	$\tilde{g} \rightarrow qq + \tilde{\chi}_1^0$	1970	1	0.61	0.000980	9k

Table 13: The parameter values for the decaying  $R$ -hadron signal MC samples  $m_{\tilde{g}} = 600$  GeV to 1200 GeV and lifetimes between 0.01 ns to 10 ns, used in this work to obtain the gluino mass vs. lifetime plane at fixed  $dM = m_{\tilde{g}} - m_{\tilde{\chi}_1^0} = 100$  GeV. Production cross section (calculated following the prescription in [35]).

DS number	Model	Production mass [GeV]	Produced particle mass [GeV]	LLP decay channel	LSP mass [GeV]	$\tau$ [ns]	$<\beta\gamma>$	$\sigma$ [pb]	Num generated
403049	Split SUSY	600	$\tilde{g} \rightarrow q\bar{q} + \tilde{\chi}_1^0$	500	0.01	1.14	9.22	6k	
403048	Split SUSY	600	$\tilde{g} \rightarrow q\bar{q} + \tilde{\chi}_1^0$	500	0.10	1.14	9.22	9k	
403045	Split SUSY	600	$\tilde{g} \rightarrow q\bar{q} + \tilde{\chi}_1^0$	500	1	1.14	9.22	9k	
403046	Split SUSY	600	$\tilde{g} \rightarrow q\bar{q} + \tilde{\chi}_1^0$	500	3	1.14	9.22	9k	
403047	Split SUSY	600	$\tilde{g} \rightarrow q\bar{q} + \tilde{\chi}_1^0$	500	10	1.11	9.22	9k	
403055	Split SUSY	800	$\tilde{g} \rightarrow q\bar{q} + \tilde{\chi}_1^0$	700	0.01	1.00	1.49	7k	
403056	Split SUSY	800	$\tilde{g} \rightarrow q\bar{q} + \tilde{\chi}_1^0$	700	0.04	1.00	1.49	9k	
403054	Split SUSY	800	$\tilde{g} \rightarrow q\bar{q} + \tilde{\chi}_1^0$	700	0.10	1.01	1.49	10k	
403051	Split SUSY	800	$\tilde{g} \rightarrow q\bar{q} + \tilde{\chi}_1^0$	700	1	1.01	1.49	8k	
403052	Split SUSY	800	$\tilde{g} \rightarrow q\bar{q} + \tilde{\chi}_1^0$	700	3	1.01	1.49	7k	
403053	Split SUSY	800	$\tilde{g} \rightarrow q\bar{q} + \tilde{\chi}_1^0$	700	10	0.99	1.49	8k	
403061	Split SUSY	1000	$\tilde{g} \rightarrow q\bar{q} + \tilde{\chi}_1^0$	900	0.01	0.90	0.325	10k	
403062	Split SUSY	1000	$\tilde{g} \rightarrow q\bar{q} + \tilde{\chi}_1^0$	900	0.04	0.90	0.325	6k	
403060	Split SUSY	1000	$\tilde{g} \rightarrow q\bar{q} + \tilde{\chi}_1^0$	900	0.10	0.90	0.325	9k	
403057	Split SUSY	1000	$\tilde{g} \rightarrow q\bar{q} + \tilde{\chi}_1^0$	900	1	0.91	0.325	10k	
403058	Split SUSY	1000	$\tilde{g} \rightarrow q\bar{q} + \tilde{\chi}_1^0$	900	3	0.90	0.325	8k	
403059	Split SUSY	1000	$\tilde{g} \rightarrow q\bar{q} + \tilde{\chi}_1^0$	900	10	0.89	0.325	10k	
403067	Split SUSY	1200	$\tilde{g} \rightarrow q\bar{q} + \tilde{\chi}_1^0$	1100	0.01	0.81	0.0856	10k	
403068	Split SUSY	1200	$\tilde{g} \rightarrow q\bar{q} + \tilde{\chi}_1^0$	1100	0.04	0.83	0.0856	8k	
403066	Split SUSY	1200	$\tilde{g} \rightarrow q\bar{q} + \tilde{\chi}_1^0$	1100	0.10	0.82	0.0856	9k	
403063	Split SUSY	1200	$\tilde{g} \rightarrow q\bar{q} + \tilde{\chi}_1^0$	1100	1	0.82	0.0856	10k	
403064	Split SUSY	1200	$\tilde{g} \rightarrow q\bar{q} + \tilde{\chi}_1^0$	1100	3	0.82	0.0856	8k	

Table 14: The parameter values for the decaying  $R$ -hadron signal MC samples  $m_{\tilde{g}} = 1400$  GeV to 2000 GeV and lifetimes from 0.01 ns to 10 ns, used in this work to obtain the gluino mass vs. lifetime plane at fixed  $dM = m_{\tilde{g}} - m_{\tilde{\chi}_1^0} = 100$  GeV. Production cross section (calculated following the prescription in [35]).

DS number	Model	Production	Produced particle mass [GeV]	LLP decay channel	LSP mass [GeV]	$\tau$ [ns]	$< \beta \gamma >$	$\sigma$ [pb]	Num generated
403073	Split SUSY	$\tilde{g}$	1400	$\tilde{g} \rightarrow qq + \tilde{\chi}_1^0$	1300	0.01	0.75	0.0253	9k
403074	Split SUSY	$\tilde{g}$	1400	$\tilde{g} \rightarrow qq + \tilde{\chi}_1^0$	1300	0.04	0.75	0.0253	8k
403072	Split SUSY	$\tilde{g}$	1400	$\tilde{g} \rightarrow qq + \tilde{\chi}_1^0$	1300	0.10	0.75	0.0253	9k
403069	Split SUSY	$\tilde{g}$	1400	$\tilde{g} \rightarrow qq + \tilde{\chi}_1^0$	1300	1	0.75	0.0253	10k
403070	Split SUSY	$\tilde{g}$	1400	$\tilde{g} \rightarrow qq + \tilde{\chi}_1^0$	1300	3	0.76	0.0253	10k
403071	Split SUSY	$\tilde{g}$	1400	$\tilde{g} \rightarrow qq + \tilde{\chi}_1^0$	1300	10	0.75	0.0253	10k
403079	Split SUSY	$\tilde{g}$	1600	$\tilde{g} \rightarrow qq + \tilde{\chi}_1^0$	1500	0.01	0.70	0.00809	10k
403080	Split SUSY	$\tilde{g}$	1600	$\tilde{g} \rightarrow qq + \tilde{\chi}_1^0$	1500	0.04	0.70	0.00809	10k
403078	Split SUSY	$\tilde{g}$	1600	$\tilde{g} \rightarrow qq + \tilde{\chi}_1^0$	1500	30	0.70	0.00809	10k
403075	Split SUSY	$\tilde{g}$	1600	$\tilde{g} \rightarrow qq + \tilde{\chi}_1^0$	1500	1	0.70	0.00809	10k
403076	Split SUSY	$\tilde{g}$	1600	$\tilde{g} \rightarrow qq + \tilde{\chi}_1^0$	1500	3	0.70	0.00809	8k
403077	Split SUSY	$\tilde{g}$	1600	$\tilde{g} \rightarrow qq + \tilde{\chi}_1^0$	1500	10	0.70	0.00809	10k
403085	Split SUSY	$\tilde{g}$	1800	$\tilde{g} \rightarrow qq + \tilde{\chi}_1^0$	1700	0.01	0.65	0.00276	9k
403086	Split SUSY	$\tilde{g}$	1800	$\tilde{g} \rightarrow qq + \tilde{\chi}_1^0$	1700	0.04	0.65	0.00276	10k
403084	Split SUSY	$\tilde{g}$	1800	$\tilde{g} \rightarrow qq + \tilde{\chi}_1^0$	1700	0.10	0.65	0.00276	10k
403081	Split SUSY	$\tilde{g}$	1800	$\tilde{g} \rightarrow qq + \tilde{\chi}_1^0$	1700	1	0.64	0.00276	8k
403082	Split SUSY	$\tilde{g}$	1800	$\tilde{g} \rightarrow qq + \tilde{\chi}_1^0$	1700	3	0.64	0.00276	9k
403083	Split SUSY	$\tilde{g}$	1800	$\tilde{g} \rightarrow qq + \tilde{\chi}_1^0$	1700	10	0.65	0.00276	10k
403091	Split SUSY	$\tilde{g}$	2000	$\tilde{g} \rightarrow qq + \tilde{\chi}_1^0$	1900	0.01	0.61	0.000980	10k
403092	Split SUSY	$\tilde{g}$	2000	$\tilde{g} \rightarrow qq + \tilde{\chi}_1^0$	1900	0.04	0.61	0.000980	10k
403090	Split SUSY	$\tilde{g}$	2000	$\tilde{g} \rightarrow qq + \tilde{\chi}_1^0$	1900	0.10	0.61	0.000980	9k
403087	Split SUSY	$\tilde{g}$	2000	$\tilde{g} \rightarrow qq + \tilde{\chi}_1^0$	1900	1	0.61	0.000980	10k
403088	Split SUSY	$\tilde{g}$	2000	$\tilde{g} \rightarrow qq + \tilde{\chi}_1^0$	1900	3	0.61	0.000980	9k
403089	Split SUSY	$\tilde{g}$	2000	$\tilde{g} \rightarrow qq + \tilde{\chi}_1^0$	1900	10	0.61	0.000980	9k

Table 15: The parameter values for the decaying  $R$ -hadron signal MC samples  $m_{\tilde{g}} = 400 \text{ GeV}$  to  $\tilde{\chi}_1^0$  and lifetimes between 0.1 ns to 30 ns, used in this work to obtain the gluino mass vs. lifetime plane at fixed neutralino mass at 100 GeV. Production cross section (calculated following the prescription in [35]).

DS number	Model	Production mass [GeV]	Produced particle mass [GeV]	LLP decay channel	LSP mass [GeV]	$\tau$ [ns]	$<\beta\gamma>$	$\sigma$ [pb]	Num generated
402034	Split SUSY	$\tilde{g}$	400	$\tilde{g} \rightarrow qq + \tilde{\chi}_1^0$	100	0.40	1.37	98.2	10k
402035	Split SUSY	$\tilde{g}$	500	$\tilde{g} \rightarrow qq + \tilde{\chi}_1^0$	100	0.40	1.24	27.5	10k
402770	Split SUSY	$\tilde{g}$	600	$\tilde{g} \rightarrow qq + \tilde{\chi}_1^0$	100	0.01	1.16	9.22	9k
402778	Split SUSY	$\tilde{g}$	600	$\tilde{g} \rightarrow qq + \tilde{\chi}_1^0$	100	0.04	1.16	9.22	8k
402786	Split SUSY	$\tilde{g}$	600	$\tilde{g} \rightarrow qq + \tilde{\chi}_1^0$	100	0.10	1.15	9.22	9k
402036	Split SUSY	$\tilde{g}$	600	$\tilde{g} \rightarrow qq + \tilde{\chi}_1^0$	100	0.40	1.15	9.22	9k
402700	Split SUSY	$\tilde{g}$	600	$\tilde{g} \rightarrow qq + \tilde{\chi}_1^0$	100	1	1.15	9.22	9k
402041	Split SUSY	$\tilde{g}$	700	$\tilde{g} \rightarrow qq + \tilde{\chi}_1^0$	100	0.40	1.07	3.53	9k
402042	Split SUSY	$\tilde{g}$	700	$\tilde{g} \rightarrow qq + \tilde{\chi}_1^0$	100	1	1.06	3.53	9k
402771	Split SUSY	$\tilde{g}$	800	$\tilde{g} \rightarrow qq + \tilde{\chi}_1^0$	100	0.01	1.00	1.49	10k
402779	Split SUSY	$\tilde{g}$	800	$\tilde{g} \rightarrow qq + \tilde{\chi}_1^0$	100	0.04	1.01	1.49	9k
402787	Split SUSY	$\tilde{g}$	800	$\tilde{g} \rightarrow qq + \tilde{\chi}_1^0$	100	0.10	1.01	1.49	8k
402043	Split SUSY	$\tilde{g}$	800	$\tilde{g} \rightarrow qq + \tilde{\chi}_1^0$	100	0.40	1.01	1.49	10k
402044	Split SUSY	$\tilde{g}$	800	$\tilde{g} \rightarrow qq + \tilde{\chi}_1^0$	100	1	1.01	1.49	10k
402045	Split SUSY	$\tilde{g}$	800	$\tilde{g} \rightarrow qq + \tilde{\chi}_1^0$	100	3	1.01	1.49	9k
402049	Split SUSY	$\tilde{g}$	900	$\tilde{g} \rightarrow qq + \tilde{\chi}_1^0$	100	0.40	0.96	0.677	9k
402050	Split SUSY	$\tilde{g}$	900	$\tilde{g} \rightarrow qq + \tilde{\chi}_1^0$	100	1	0.95	0.677	9k
402051	Split SUSY	$\tilde{g}$	900	$\tilde{g} \rightarrow qq + \tilde{\chi}_1^0$	100	3	0.95	0.677	9k
402772	Split SUSY	$\tilde{g}$	1000	$\tilde{g} \rightarrow qq + \tilde{\chi}_1^0$	100	0.01	0.90	0.325	8k
402780	Split SUSY	$\tilde{g}$	1000	$\tilde{g} \rightarrow qq + \tilde{\chi}_1^0$	100	0.04	0.91	0.325	10k
402788	Split SUSY	$\tilde{g}$	1000	$\tilde{g} \rightarrow qq + \tilde{\chi}_1^0$	100	0.10	0.90	0.325	10k
402052	Split SUSY	$\tilde{g}$	1000	$\tilde{g} \rightarrow qq + \tilde{\chi}_1^0$	100	0.40	0.90	0.325	9k
402053	Split SUSY	$\tilde{g}$	1000	$\tilde{g} \rightarrow qq + \tilde{\chi}_1^0$	100	1	0.90	0.325	9k
402054	Split SUSY	$\tilde{g}$	1000	$\tilde{g} \rightarrow qq + \tilde{\chi}_1^0$	100	3	0.90	0.325	9k
402055	Split SUSY	$\tilde{g}$	1000	$\tilde{g} \rightarrow qq + \tilde{\chi}_1^0$	100	10	0.90	0.325	9k
402056	Split SUSY	$\tilde{g}$	1000	$\tilde{g} \rightarrow qq + \tilde{\chi}_1^0$	100	30	0.85	0.325	9k
402057	Split SUSY	$\tilde{g}$	1000	$\tilde{g} \rightarrow qq + \tilde{\chi}_1^0$	100	50	0.80	0.325	9k
402067	Split SUSY	$\tilde{g}$	1100	$\tilde{g} \rightarrow qq + \tilde{\chi}_1^0$	100	0.40	0.85	0.163	9k
402068	Split SUSY	$\tilde{g}$	1100	$\tilde{g} \rightarrow qq + \tilde{\chi}_1^0$	100	1	0.86	0.163	10k
402069	Split SUSY	$\tilde{g}$	1100	$\tilde{g} \rightarrow qq + \tilde{\chi}_1^0$	100	3	0.86	0.163	9k
402070	Split SUSY	$\tilde{g}$	1100	$\tilde{g} \rightarrow qq + \tilde{\chi}_1^0$	100	10	0.86	0.163	9k
402071	Split SUSY	$\tilde{g}$	1100	$\tilde{g} \rightarrow qq + \tilde{\chi}_1^0$	100	30	0.81	0.163	9k
402072	Split SUSY	$\tilde{g}$	1100	$\tilde{g} \rightarrow qq + \tilde{\chi}_1^0$	100	50	0.77	0.163	9k

Not reviewed, for internal circulation only

Table 16: The parameter values for the decaying  $R$ -hadron signal MC samples  $m_{\tilde{g}} = 1200$  GeV to 1500 GeV and lifetimes between 0.01 ns to 50 ns, used in this work to obtain the gluino mass vs. lifetime plane at fixed neutralino mass at 100 GeV. Production cross section (calculated following the prescription in [35]).

DS number	Model	Production mass [GeV]	Produced particle mass [GeV]	LLP decay channel	LSP mass [GeV]	$\tau$ [ns]	$<\beta\gamma>$	$\sigma$ [pb]	Num generated
402773	Split SUSY	$\tilde{g}$	1200	$\tilde{g} \rightarrow q\bar{q} + \tilde{\chi}_1^0$	100	0.01	0.82	0.0856	10k
402781	Split SUSY	$\tilde{g}$	1200	$\tilde{g} \rightarrow q\bar{q} + \tilde{\chi}_1^0$	100	0.04	0.82	0.0856	8k
402789	Split SUSY	$\tilde{g}$	1200	$\tilde{g} \rightarrow q\bar{q} + \tilde{\chi}_1^0$	100	0.10	0.82	0.0856	10k
402073	Split SUSY	$\tilde{g}$	1200	$\tilde{g} \rightarrow q\bar{q} + \tilde{\chi}_1^0$	100	0.40	0.82	0.0856	5k
402074	Split SUSY	$\tilde{g}$	1200	$\tilde{g} \rightarrow q\bar{q} + \tilde{\chi}_1^0$	100	1	0.82	0.0856	10k
402075	Split SUSY	$\tilde{g}$	1200	$\tilde{g} \rightarrow q\bar{q} + \tilde{\chi}_1^0$	100	3	0.83	0.0856	9.8k
402076	Split SUSY	$\tilde{g}$	1200	$\tilde{g} \rightarrow q\bar{q} + \tilde{\chi}_1^0$	100	10	0.82	0.0856	9k
402077	Split SUSY	$\tilde{g}$	1200	$\tilde{g} \rightarrow q\bar{q} + \tilde{\chi}_1^0$	100	30	0.78	0.0856	9k
402078	Split SUSY	$\tilde{g}$	1200	$\tilde{g} \rightarrow q\bar{q} + \tilde{\chi}_1^0$	100	50	0.74	0.0856	9k
402088	Split SUSY	$\tilde{g}$	1300	$\tilde{g} \rightarrow q\bar{q} + \tilde{\chi}_1^0$	100	0.40	0.78	0.0460	9k
402089	Split SUSY	$\tilde{g}$	1300	$\tilde{g} \rightarrow q\bar{q} + \tilde{\chi}_1^0$	100	1	0.79	0.0460	8k
402090	Split SUSY	$\tilde{g}$	1300	$\tilde{g} \rightarrow q\bar{q} + \tilde{\chi}_1^0$	100	3	0.79	0.0460	9k
402091	Split SUSY	$\tilde{g}$	1300	$\tilde{g} \rightarrow q\bar{q} + \tilde{\chi}_1^0$	100	10	0.79	0.0460	9k
402092	Split SUSY	$\tilde{g}$	1300	$\tilde{g} \rightarrow q\bar{q} + \tilde{\chi}_1^0$	100	30	0.75	0.0460	9k
402093	Split SUSY	$\tilde{g}$	1300	$\tilde{g} \rightarrow q\bar{q} + \tilde{\chi}_1^0$	100	50	0.72	0.0460	10k
402774	Split SUSY	$\tilde{g}$	1400	$\tilde{g} \rightarrow q\bar{q} + \tilde{\chi}_1^0$	100	0.01	0.76	0.0253	10k
402782	Split SUSY	$\tilde{g}$	1400	$\tilde{g} \rightarrow q\bar{q} + \tilde{\chi}_1^0$	100	0.04	0.75	0.0253	9k
402790	Split SUSY	$\tilde{g}$	1400	$\tilde{g} \rightarrow q\bar{q} + \tilde{\chi}_1^0$	100	0.10	0.75	0.0253	9k
402094	Split SUSY	$\tilde{g}$	1400	$\tilde{g} \rightarrow q\bar{q} + \tilde{\chi}_1^0$	100	0.40	0.75	0.0253	5k
402720	Split SUSY	$\tilde{g}$	1400	$\tilde{g} \rightarrow q\bar{q} + \tilde{\chi}_1^0$	100	1	0.75	0.0253	9k
402096	Split SUSY	$\tilde{g}$	1400	$\tilde{g} \rightarrow q\bar{q} + \tilde{\chi}_1^0$	100	3	0.75	0.0253	10k
402097	Split SUSY	$\tilde{g}$	1400	$\tilde{g} \rightarrow q\bar{q} + \tilde{\chi}_1^0$	100	10	0.75	0.0253	9k
402098	Split SUSY	$\tilde{g}$	1400	$\tilde{g} \rightarrow q\bar{q} + \tilde{\chi}_1^0$	100	30	0.72	0.0253	9k
402099	Split SUSY	$\tilde{g}$	1400	$\tilde{g} \rightarrow q\bar{q} + \tilde{\chi}_1^0$	100	50	0.69	0.0253	9k
402109	Split SUSY	$\tilde{g}$	1500	$\tilde{g} \rightarrow q\bar{q} + \tilde{\chi}_1^0$	100	1	0.72	0.0142	10k
402110	Split SUSY	$\tilde{g}$	1500	$\tilde{g} \rightarrow q\bar{q} + \tilde{\chi}_1^0$	100	3	0.72	0.0142	9k
402111	Split SUSY	$\tilde{g}$	1500	$\tilde{g} \rightarrow q\bar{q} + \tilde{\chi}_1^0$	100	10	0.72	0.0142	9k
402112	Split SUSY	$\tilde{g}$	1500	$\tilde{g} \rightarrow q\bar{q} + \tilde{\chi}_1^0$	100	30	0.70	0.0142	10k
402113	Split SUSY	$\tilde{g}$	1500	$\tilde{g} \rightarrow q\bar{q} + \tilde{\chi}_1^0$	100	50	0.67	0.0142	10k

Not reviewed, for internal circulation only

Table 17: The parameter values for the decaying  $R$ -hadron signal MC samples  $m_{\tilde{g}} = 1200$  GeV to 1500 GeV and lifetimes between 0.01 ns to 50 ns, used in this work to obtain the gluino mass vs. lifetime plane at fixed neutralino mass at 100 GeV. Production cross section (calculated following the prescription in [35]).

DS number	Model	Production mass [GeV]	Produced particle mass [GeV]	LLP decay channel	LSP mass [GeV]	$\tau$ [ns]	$<\beta\gamma>$	$\sigma$ [pb]	Num generated
402775	Split SUSY	1600	$\tilde{g} \rightarrow qq + \tilde{\chi}_1^0$	100	0.01	0.70	0.00809	10k	
402783	Split SUSY	1600	$\tilde{g} \rightarrow qq + \tilde{\chi}_1^0$	100	0.04	0.70	0.00809	8.5k	
402791	Split SUSY	1600	$\tilde{g} \rightarrow qq + \tilde{\chi}_1^0$	100	0.10	0.70	0.00809	9k	
402725	Split SUSY	1600	$\tilde{g} \rightarrow qq + \tilde{\chi}_1^0$	100	1	0.70	0.00809	10k	
402115	Split SUSY	1600	$\tilde{g} \rightarrow qq + \tilde{\chi}_1^0$	100	3	0.70	0.00809	5k	
402116	Split SUSY	1600	$\tilde{g} \rightarrow qq + \tilde{\chi}_1^0$	100	10	0.69	0.00809	9k	
402117	Split SUSY	1600	$\tilde{g} \rightarrow qq + \tilde{\chi}_1^0$	100	30	0.67	0.00809	10k	
402118	Split SUSY	1600	$\tilde{g} \rightarrow qq + \tilde{\chi}_1^0$	100	50	0.65	0.00809	10k	
402128	Split SUSY	1700	$\tilde{g} \rightarrow qq + \tilde{\chi}_1^0$	100	3	0.68	0.00470	5k	
402129	Split SUSY	1700	$\tilde{g} \rightarrow qq + \tilde{\chi}_1^0$	100	10	0.67	0.00470	10k	
402130	Split SUSY	1700	$\tilde{g} \rightarrow qq + \tilde{\chi}_1^0$	100	30	0.65	0.00470	10k	
402131	Split SUSY	1700	$\tilde{g} \rightarrow qq + \tilde{\chi}_1^0$	100	50	0.62	0.00470	9k	
402776	Split SUSY	1800	$\tilde{g} \rightarrow qq + \tilde{\chi}_1^0$	100	0.01	0.65	0.00276	9k	
402784	Split SUSY	1800	$\tilde{g} \rightarrow qq + \tilde{\chi}_1^0$	100	0.04	0.65	0.00276	10k	
402792	Split SUSY	1800	$\tilde{g} \rightarrow qq + \tilde{\chi}_1^0$	100	0.10	0.65	0.00276	10k	
402132	Split SUSY	1800	$\tilde{g} \rightarrow qq + \tilde{\chi}_1^0$	100	3	0.65	0.00276	5k	
402133	Split SUSY	1800	$\tilde{g} \rightarrow qq + \tilde{\chi}_1^0$	100	10	0.65	0.00276	10k	
402134	Split SUSY	1800	$\tilde{g} \rightarrow qq + \tilde{\chi}_1^0$	100	30	0.63	0.00276	10k	
402135	Split SUSY	1800	$\tilde{g} \rightarrow qq + \tilde{\chi}_1^0$	100	50	0.60	0.00276	10k	
402142	Split SUSY	1900	$\tilde{g} \rightarrow qq + \tilde{\chi}_1^0$	100	10	0.62	0.00163	10k	
402143	Split SUSY	1900	$\tilde{g} \rightarrow qq + \tilde{\chi}_1^0$	100	30	0.61	0.00163	8k	
402144	Split SUSY	1900	$\tilde{g} \rightarrow qq + \tilde{\chi}_1^0$	100	50	0.59	0.00163	9k	
402777	Split SUSY	2000	$\tilde{g} \rightarrow qq + \tilde{\chi}_1^0$	100	0.01	0.61	0.000980	10k	
402785	Split SUSY	2000	$\tilde{g} \rightarrow qq + \tilde{\chi}_1^0$	100	0.04	0.61	0.000980	10k	
402793	Split SUSY	2000	$\tilde{g} \rightarrow qq + \tilde{\chi}_1^0$	100	0.10	0.61	0.000980	10k	
402735	Split SUSY	2000	$\tilde{g} \rightarrow qq + \tilde{\chi}_1^0$	100	1	0.61	0.000980	9.8k	
402145	Split SUSY	2000	$\tilde{g} \rightarrow qq + \tilde{\chi}_1^0$	100	10	0.61	0.000980	5k	
402146	Split SUSY	2000	$\tilde{g} \rightarrow qq + \tilde{\chi}_1^0$	100	30	0.59	0.000980	5k	
402147	Split SUSY	2000	$\tilde{g} \rightarrow qq + \tilde{\chi}_1^0$	100	50	0.57	0.000980	10k	

Table 18: Cut flows are shown for various  $R$ -hadron signal samples normalized to  $32.7 \text{ fb}^{-1}$ .

$(m_{\tilde{g}}, m_{\tilde{\chi}_1^0}, \tau)$ [GeV, GeV, ns]	(1400, 100, 1)	(2000, 100, 1)	(2000, 1800, 1)	(1400, 100, 0.1)
Initial Events	827	32	32	827
Trigger-based data reduction	826	32	27	827
Event cleaning	826	32	27	827
Good Runs List	826	32	27	827
Primary vertex	826	32	27	827
NCB veto	823	32	26	824
$E_T^{\text{miss}}$ trigger	791	31	24	803
$E_T^{\text{miss}}$ filter	760	31	17	717
Offline $E_T^{\text{miss}}$	671	29	7	641
DV fiducial acceptance	620	28	6	625
DV fit quality	615	27	6	621
DV displacement	613	27	6	608
Material veto	493	22	5	544
Disabled module veto	480	22	5	541
DV track multiplicity	331	15	3	455
DV mass	305	14	2	442

Not reviewed, for internal circulation only

981 **B. Monte Carlo signal cut flows**

### 982 C. $E_T^{\text{miss}}$ cut dependence on signal

983 The left plot in Figure 63 shows the offline  $E_T^{\text{miss}}$  distribution for several  $R$ -hadron MC samples before  
 984 and after applying the set of triggers used to select the data. The figure shows how the low dM scenarios  
 985 are more sensitive to a potential cut in high  $E_T^{\text{miss}}$  although they populate the high-tail region. The right  
 986 plot shows the expected significance as a function of offline  $E_T^{\text{miss}}$ , using a background estimate extracted  
 987 following the method outlined in Section 5. Given the trigger requirements, a minimum cut in the offline  
 988  $E_T^{\text{miss}}$  is needed around 200 GeV, however, this figure shows that the sensitivity to 1200 GeV gluino  
 989 scenarios does not depend strongly on the value for the  $E_T^{\text{miss}}$  threshold around the selected value, and it is  
 990 therefore worth cutting in the plateau of the turn-on curves both for the trigger and the MET\_LocHadTopo  
 991 cut applied in the pre-selection filtering.

Not reviewed, for internal circulation only

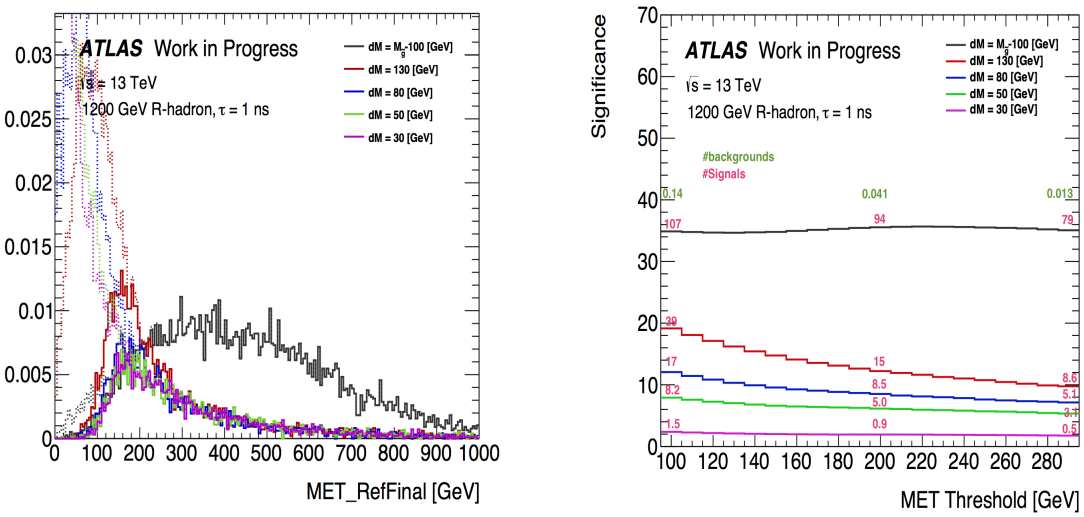


Figure 63: (Left) Offline- $E_T^{\text{miss}}$  distribution for several  $R$ -hadron MC samples: dashed (solid) lines show the distribution before (after) applying the requirement of the 2016 xe100 triggers. (Right) Expected significance as a function of offline  $E_T^{\text{miss}}$  threshold.

Not reviewed, for internal circulation only

## 992 D. SUSY Background Forum analysis checklist items

993 Following the procedure described in the [SUSY Background Forum Analysis Checklist](#), this section  
 994 contains plots and studies with standard diagnostic plots to ensure there are no unexpected, unphysical  
 995 features arising from changing detector conditions, trigger menu, etc.

996 The selection efficiency as a function of the average  $\mu$  and number of primary vertices is shown in Fig-  
 997 ure 64. The luminosity-normalized selection efficiency as a function of Run Number is shown in Fig-  
 998 ure 65. Notice the discontinuity in acceptance expected from the switch in DRAW filters part way through  
 999 2016.

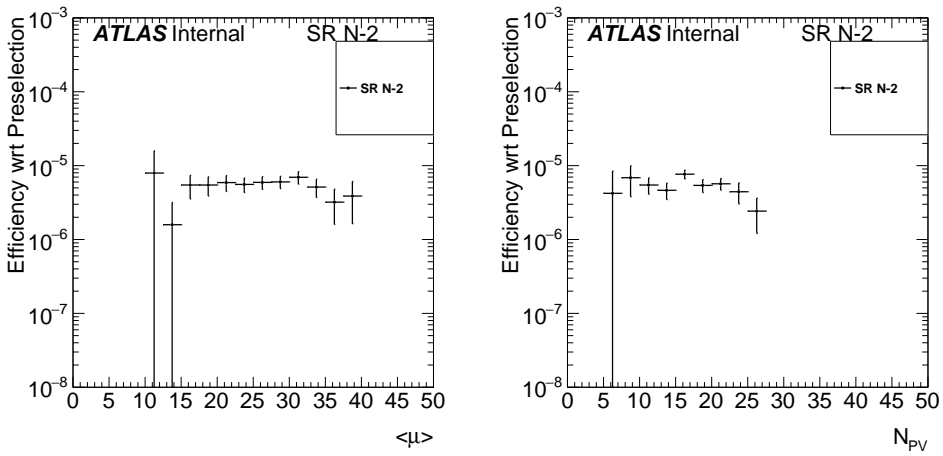


Figure 64: The selection efficiency is shown as a function of the average number of interactions per bunch crossing  $\langle\mu\rangle$  (Left) and the number of reconstructed primary vertices in the event  $N_{PV}$  (Right). [Plots still blinded. To be recreated when unblinded with additional curves.]

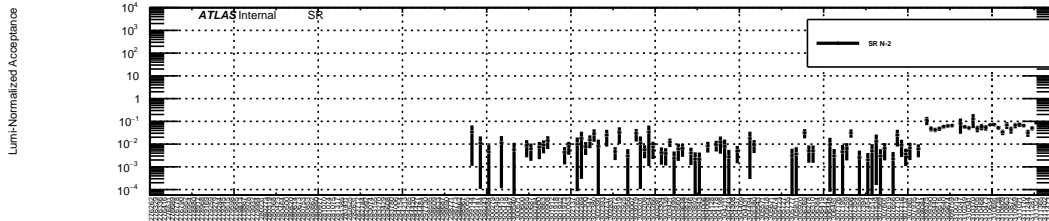


Figure 65: The selection efficiency is shown normalized to per-run integrated luminosity as a function of Run Number. [Plots still blinded. To be recreated when unblinded with additional curves.]

1000 The leading jet and  $E_T^{\text{miss}}$   $\phi$  are shown in Figure 66 given the event selection minus the mass and  $N_{trk}$   
 1001 requirements on the DV. The 2D distribution of the leading jet  $\phi$  and  $\eta$  given the same event selection is  
 1002 shown in Figure 67.

1003 Additional checks were performed in accordance with the Background forum analysis checklist.

Not reviewed, for internal circulation only

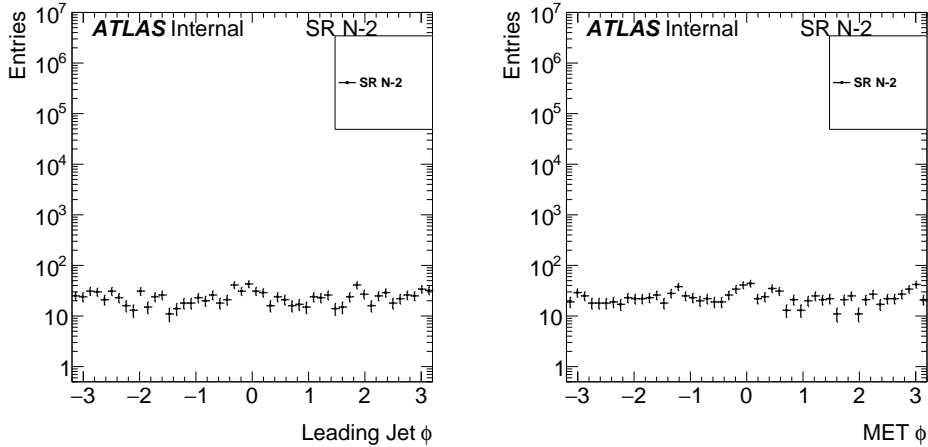


Figure 66: The azimuthal angle  $\phi$  of the leading jet (left) and  $E_T^{\text{miss}}$  (right) of events selected through the entire cutflow except for the  $N_{trk}$  and  $m_{DV}$  requirements on the selected displaced vertices. [Plots still blinded. To be recreated when unblinded with additional curves.]

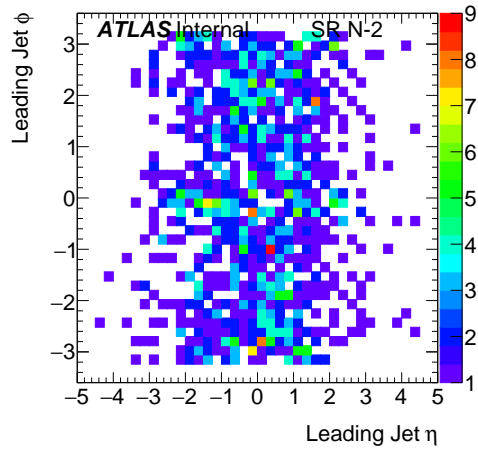


Figure 67: The azimuthal angle  $\phi$  and pseudorapidity  $\eta$  of the leading jet in events selected through the entire cutflow except for the  $N_{trk}$  and  $m_{DV}$  requirements on the selected displaced vertices. [Plots still blinded. Additional plots to be created post unblinding.]

- 
- 1004     • Check for missing data: A small amount missing as described in the note. A modified GRL ac-  
1005       counts for the effect of a small amount of missing data missed in the dedicated reprocessing step.  
1006     • Check for duplicated events: A dedicated check showed no duplicate events.  
1007     • Check sensitivity to treating MC as 2015 or 2016: Only analyzing 2016 data in this search.  
1008     • Debug stream yields in SR and CR: A check of debug stream events yielded no events passing  
1009       SR/CR selections.  
1010     • Pileup reweighting check: Accounted for in analysis with dedicated uncertainty applied. Further  
1011       studies of DV properties as a function of pileup show significant pileup dependence on the mass of  
1012       the displaced vertex candidates.  
1013     • L1Calo timing issue: Search only analyzes 2016 data and is therefore not affected by this issue.

Not reviewed, for internal circulation only

## 1014 E. Large radius tracking validation

1015 A dedicated note for the Large radius tracking is in preparation; meanwhile some studies have been  
 1016 performed in order to assess the performance and the simulation description of the Large radius tracks  
 1017 (LRT).

1018 This study has used data from a low- $\mu$  run, 299390 (Period-A), present in the minimum bias stream [36].  
 1019 The available RAW data have been processed following the same procedure described at Section 2 in  
 1020 order to obtain the LRT. After the reconstruction, the dataset contains slightly below than 1.5M events,  
 1021 and order of 70M of tracks, with an equivalent luminosity of  $12.6 \text{ nb}^{-1}$ :

1022 `data16_13TeV:data16_13TeV.00299390.physics_MinBias.daq.RAW`

1023 The data is compared with a simulation sample generated using Pythia 8.186 [22]. The ATLAS minimum-  
 1024 bias tune A2 [37] is used, which is based on the MSTW2008LO PDF [38]. Again the reconstruction proced-  
 1025 ure for MC samples described at Section 2 is applied. The processed sample contains 1.6M events, with  
 1026 around 30M tracks.

1027 `mc15_13TeV.361203.Pythia8_A2_MSTW2008LO_ND_minbias.merge.HITS.e3639_s2601_s2132`

1028 Tracks are selected on those events that at least one reconstructed primary vertex is present and there is  
 1029 at least one track in the event fulfilling the loose track-quality selection provided by the TrackingCP [39]  
 1030 group. The events in the simulation are weighted in order to reproduce the PV-z distribution, and each  
 1031 track family (standard tracks and LRT separately) are weighted in order to match the kinematic,  $p_T$   
 1032 and  $\eta$ , distributions in data. Note that no further requirements are applied to the tracks. Si-seeded and  
 1033 TRT-standalone tracks have been used as handles to control the standard tracking reconstruction perform-  
 1034 ance [40].

1035 Figure 68 shows the number of hits<sup>4</sup> distributions in data compared with simulation, and Figure 69, the  
 1036 same observables averaged for all tracks at the same  $\eta$ . In both cases, the simulation is reproducing well  
 1037 the data behaviour.

1038 The transverse and longitudinal impact track parameters are shown in Figure 70. The transverse impact  
 1039 parameter distribution reproduces the resolution for the standard, low- $d_0$  tracks, populating the central  
 1040 peak; whilst pure large radius tracks have higher resolutions. The double-horned peaks shape is con-  
 1041 sequence of using the beam spot, with finite resolution, as reference point. For large  $d_0$  tracks, the size  
 1042 of the beam spot abruptly changes the sign of tracks with  $d_0$  close enough to the beam spot radius. As  
 1043 the transversal case, the longitudinal impact parameter for LRT is higher than the standard tracks [40], as  
 1044 consequence of the loosed cuts used in the LRT configuration.

1045 In order to understand the potential of the LRT to reconstruct tracks from particles decayed at significant  
 1046 distance of the interaction point, Figure 71 plot the distribution of the radius of the first measured hit  
 1047 on the track. Conversely to the standard tracks, there is an important population of tracks with high  
 1048 radius first hit, improving the capacity to reconstruct long-lived particle decays, although increasing as  
 1049 well the probability to reconstruct fakes or low- $p_T$  secondary particles. This is being studied by the  
 1050 TrackingCPLargeRadius group [41].

<sup>4</sup> And disable modules in the pixel and SCT cases

Not reviewed, for internal circulation only

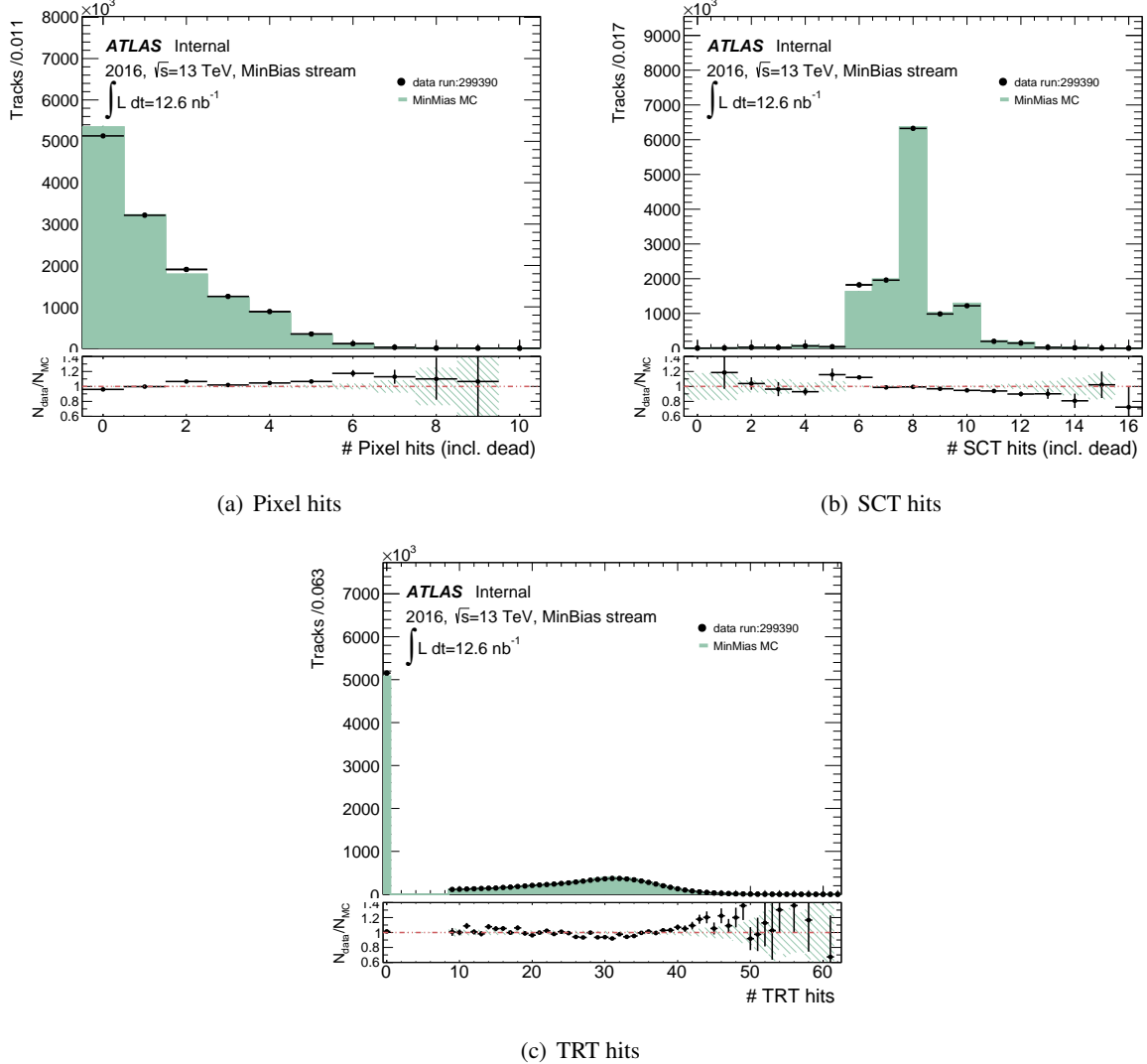


Figure 68: Number of pixel, SCT and TRT hits distributions for data compared with MC. Both pixel and SCT contains also the number holes corresponding to disable-modules. MC is normalize to the number of tracks in data.

Not reviewed, for internal circulation only

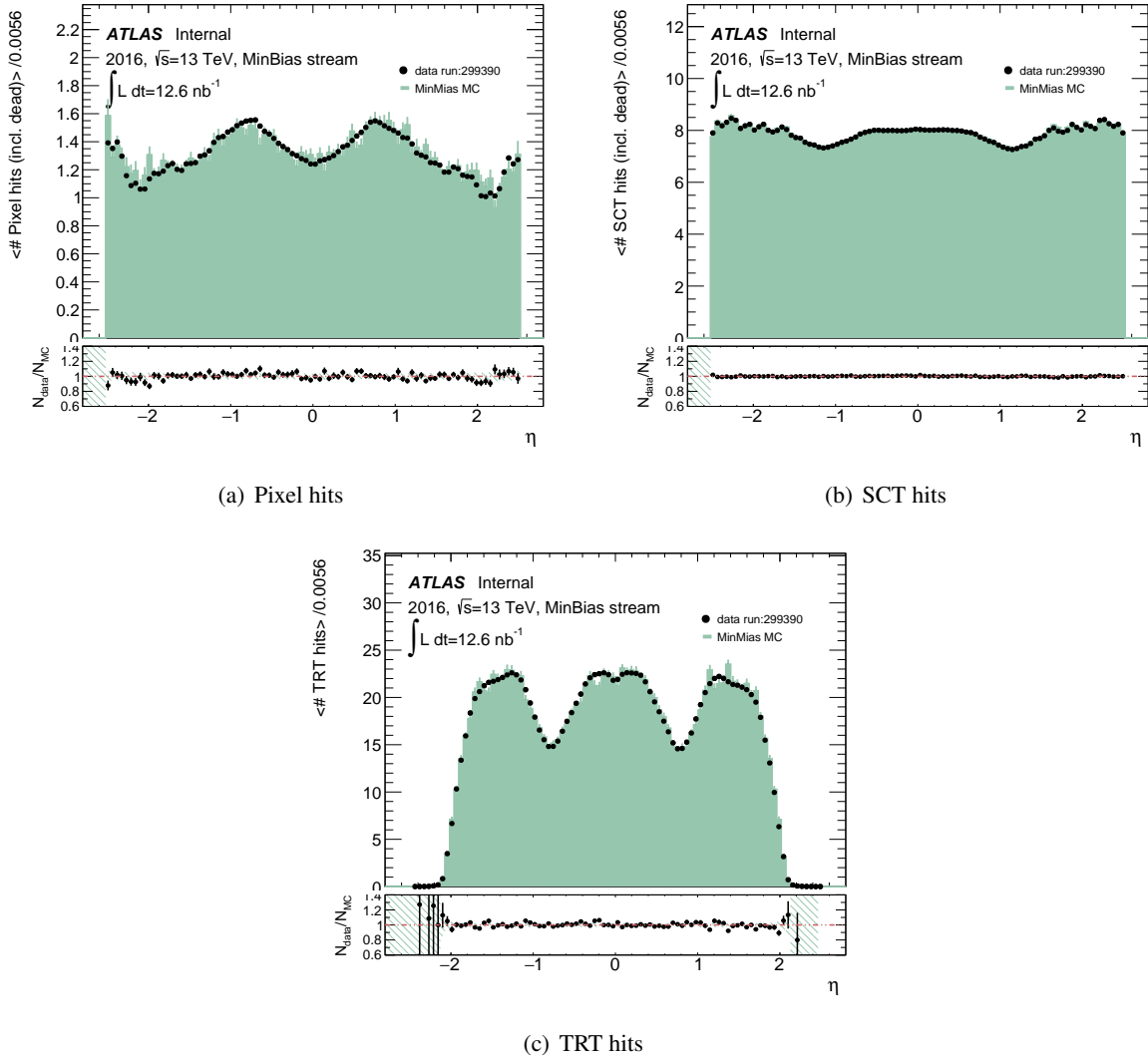


Figure 69: Average number of pixel, SCT and TRT hits distributions in function of the  $\eta$  of the track. Both pixel and SCT contains also the number holes corresponding to disable-modules. MC is normalized to the number of tracks in data.

Not reviewed, for internal circulation only

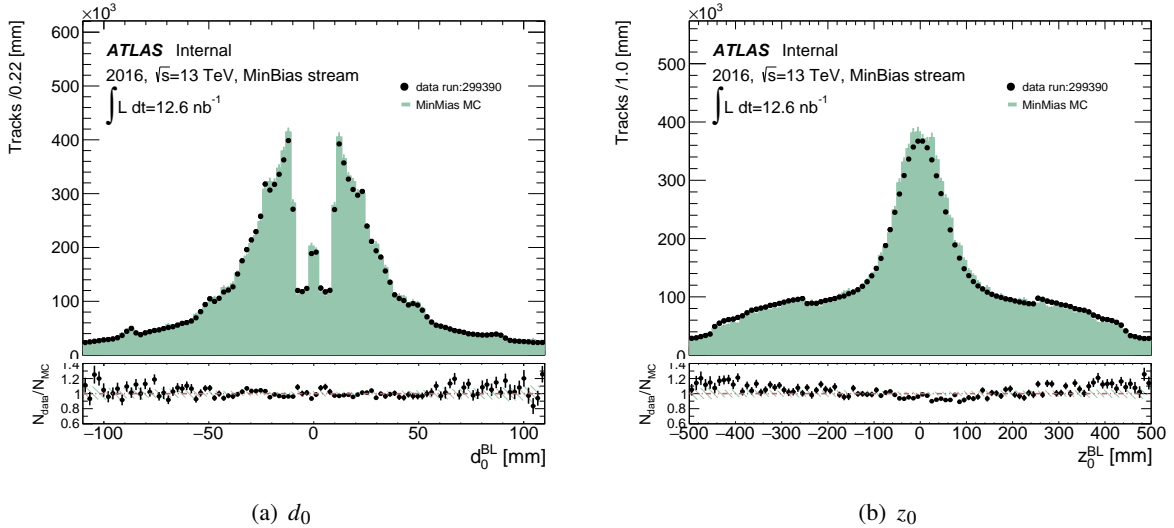


Figure 70: Transverse 70(a) and longitudinal 70(b) impact parameters in data and simulation. The simulated sample has been normalized to the number of tracks in data.

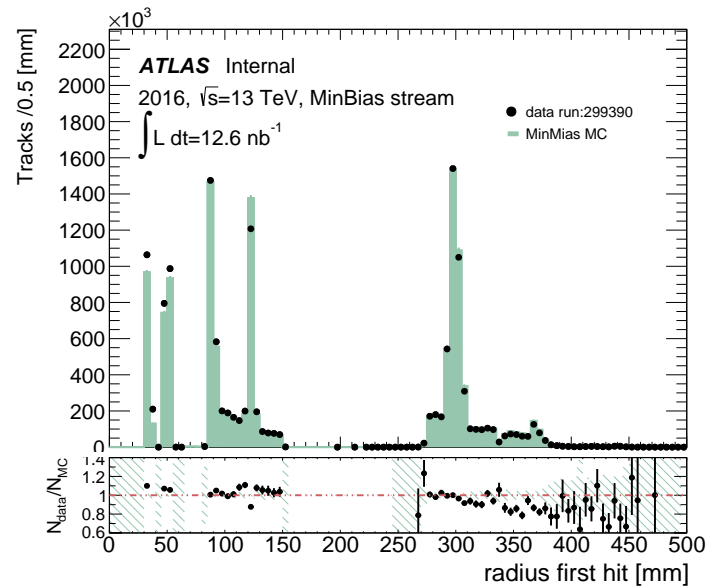


Figure 71: Radius of the first measured hit in the tracks. Note that points near the edges of the detector planes are not reproduced in simulation, as consequence of the mis-alignment not present in the MC, as reveals Figure 72

1051 Although simulation reproduces significantly well the positions of the first hit in data, there are some  
 1052 points that are not present in MC, and therefore some bin migrations are observed. The reason for this  
 1053 disagreement falls on the mis-alignment and disable modules present in data but not fully translated to  
 1054 the simulation. The lack of mis-alignment on simulation becomes evident by using the radius of the first  
 1055 hit combined with the estimated  $\phi_0$  of the tracks to obtain Figure 72, which shows the radial- $\phi$  structure of the four layers of the pixel barrel detector.

Not reviewed, for internal circulation only

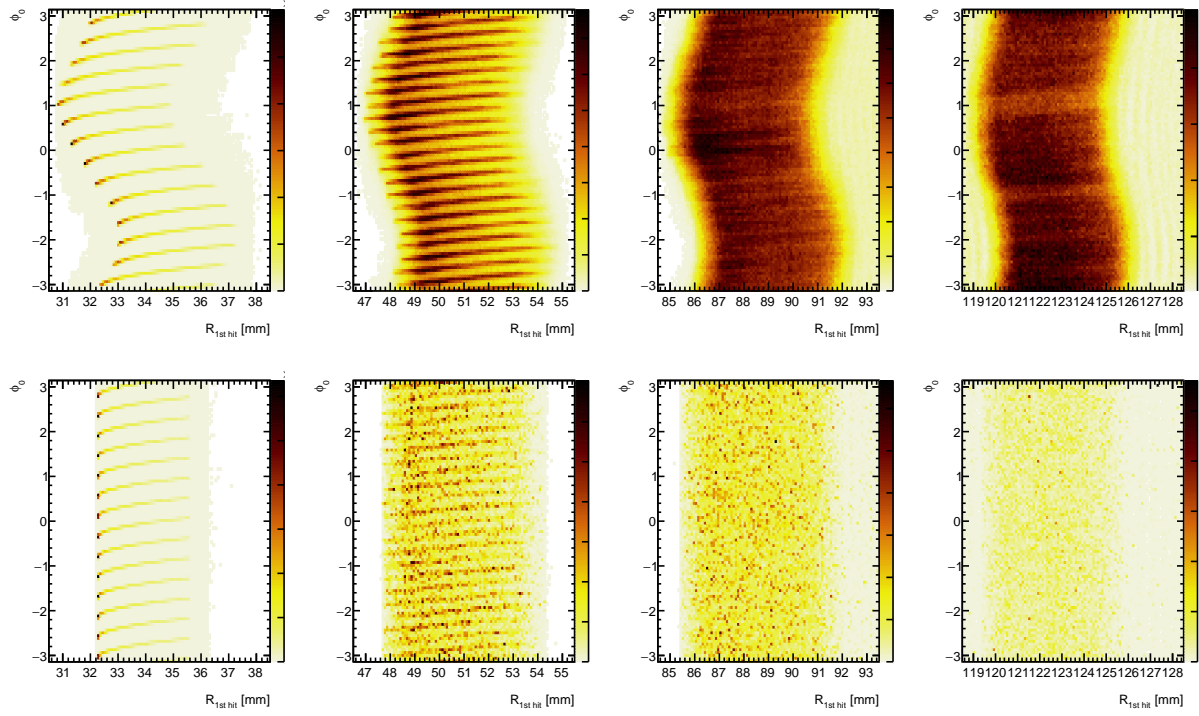


Figure 72: Radius of the first hit of the large radius tracks combined with their estimated  $\phi_0$  in order to obtain the estimated position of the hit in the  $R - \phi$  plane of the detector. From left to right, only the radius corresponding to the near positions of the four pixel barrel layers respectively have been plotted, being the top row data points, and the bottom row MC.

## 1057 F. Hadronic interactions

1058 Section 5.2 describes the method used to estimate the number of vertices produced by hadronic interac-  
 1059 tions which relies in the assumption that the low-mass component of the distribution (given a number of  
 1060 tracks in the vertex) follows an exponential function. This hypothesis is tested in this appendix by using  
 1061 an enriched region of hadronic interaction vertices and studying in there their mass distribution.

### 1062 F.1. Hadronic interactions in material-dominated detector regions

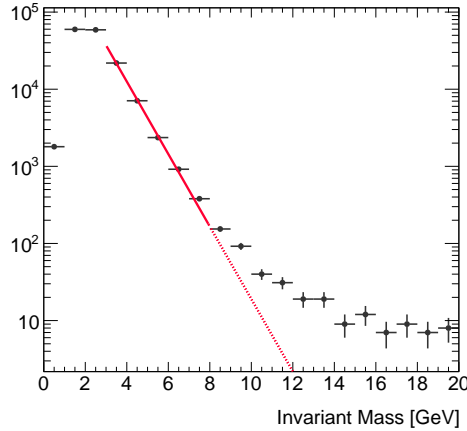
1063 An enriched hadronic interaction vertices is obtained by using the “BASE” vertex selection but the material  
 1064 veto inverted. Figure 73 shows the invariant mass distributions of the vertices reconstructed in that region;  
 1065 an exponential function has been fitted around 5 GeV, after the low mass peak. It can be observed that for  
 1066 the low track multiplicity there is a visible deviation from the exponential curves, which dilutes whenever  
 1067 the track multiplicity is increased. That contribution is supposed to come from the random crossing  
 1068 tracks.

1069 The random crossing probability is highly correlated with the track density, i.e. the probability to attach  
 1070 a random track to a vertex increases whenever more tracks are present. Therefore, the random crossing  
 1071 tracks contribution in the tails of the distributions at Figure 73 can be checked by splitting the sample in  
 1072 high-track density events, i.e. high number of interactions per bunch crossing ( $\mu$ ); and low-track density  
 1073 events, i.e. low- $\mu$ . Figure 74(a) shows several  $\mu$  slices of 3-track DV mass distribution which passed the  
 1074 “BASE” vertex selection but inverting material veto requirement.

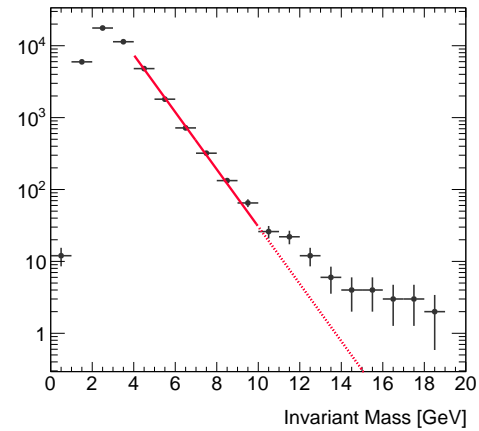
1075 The plot strongly supports that the high-tail mass distribution is produced by random crossing tracks  
 1076 vertices, given that the non-exponential components decrease as  $\mu$  value decreases. Therefore, this sus-  
 1077 tains the factorization of the mass spectrum into a low mass peak which falls off exponentially, and a  
 1078 non-exponential tail from random crossing tracks vertices.

1079 Figure 74(b) shows that the fraction of the number of DVs with mass above 10 GeV for each  $\mu$  slice in  
 1080 Figure 74(a). The  $x$  position of each points represents average  $\mu$  of each slice. Fitting function is simple  
 1081 exponential function  $\exp(p_0 + p_1 \cdot \mu)$ . The fitting results are  $p_0 = -8.95 \pm 0.81$  and  $p_1 = 0.13 \pm 0.03$ .  
 1082 The  $y$ -intercept is  $1.3 \times 10^{-4}$ . This means that, even if contribution from hadronic interaction does not  
 1083 perfectly follow exponential function, its non-exponential component should be  $O(10^{-4})$  of all DVs for  
 1084 3-track DVs. Such component is consistent with zero in the statistical region of the nominal regions  
 1085 (where material veto requirement is not inverted).

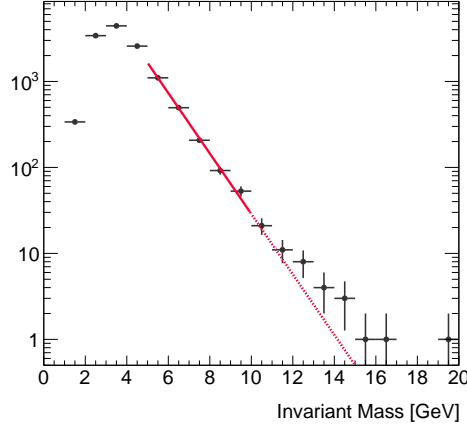
Not reviewed, for internal circulation only



(a) 4-track DVs



(b) 5-track DVs



(c) 6-track DVs

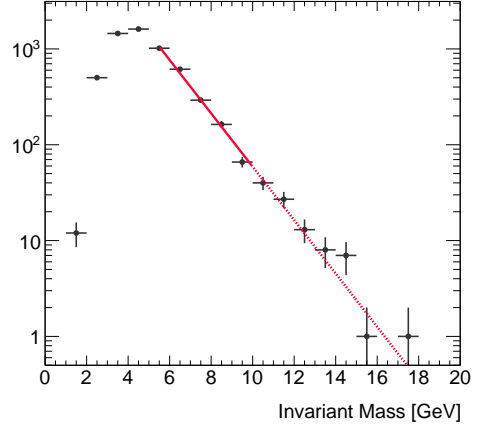
(d)  $\geq 7$ -track DVs

Figure 73: The invariant mass distributions of vertices with more than 3 tracks after “BASE” vertex selection but material veto is inverted. Red solid lines are fitted exponential functions and Red dashed lines are extrapolation of them.

Not reviewed, for internal circulation only

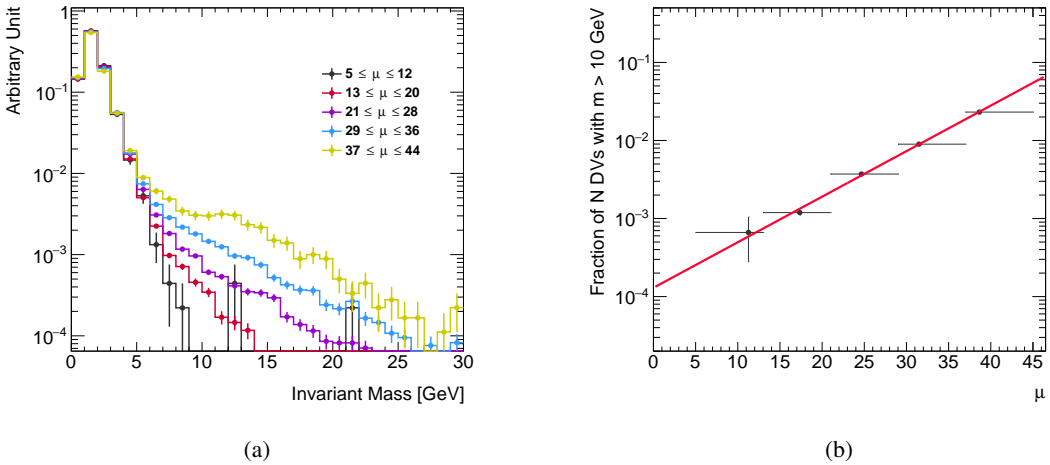


Figure 74: (a) The  $\mu$  slices of 3-track DV mass distribution of SUSY15 data samples in 2016. The DVs passed the base selection but inverting material veto requirement. Non-exponential components in the mass spectra decrease as  $\mu$  value decreases. (b) Fraction of the number of DVs with mass above 10 GeV for each  $\mu$  slice. The  $x$  position of each points represents average  $\mu$  of each slice. Fitting function is simple exponential function  $\exp(p_0 + p_1 \cdot \mu)$ . The fitting results are  $p_0 = -8.95 \pm 0.81$  and  $p_1 = 0.13 \pm 0.03$ .

1086 **F.2. GEANT4 studies**

1087 A study was performed using full AODs of the PYTHIA8 dijet sample (slice JZ3W). Truth vertices with bar-  
 1088 code -200000 or below were selected as being interactions simulated by GEANT4. For these interactions,  
 1089 a vertex mass is calculated several ways.

- 1090 1. Using all outgoing truth particles from the truth vertex  
 1091 2. Using only final-state charged particles with  $p_T$  above 1 GeV  
 1092 3. Using only final-state charged particles with  $p_T$  above 1 GeV using an assumption of the charged  
 1093 pion mass to simulate the reco-level vertex reconstruction

1094 A plot of these definitions inclusive in vertex particle multiplicity can be found in Figure 75(a), nor-  
 1095 malized to the integral above 10 GeV. The shape of the fully inclusive distribution is indicative of the  
 1096 complex nature of the GEANT4 simulation attempting to describe the interactions with heavy elements in  
 1097 the detector material. This inclusive distribution as a function of mass and radial distance shows clearly in  
 1098 Figure 75(b) that there are features as expected. The largely Be-9 beam pipe at 25 mm is clearly visible,  
 1099 as is the C-12 structures in the IBL support and IBL modules. A clear contribution is seen at the IBL  
 1100 radius of Si-28 interactions.

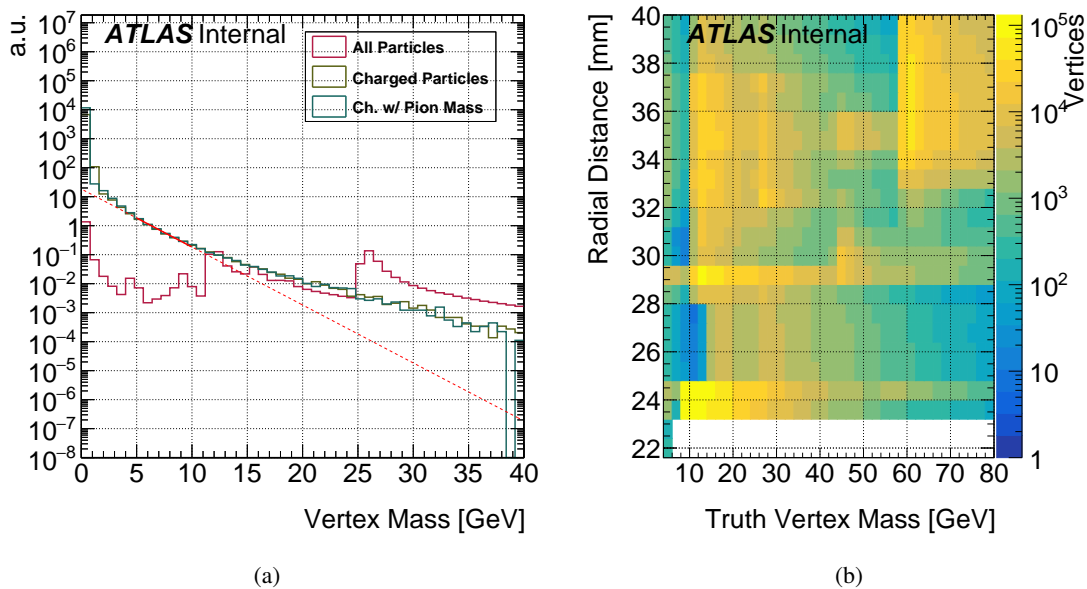


Figure 75: The truth vertex masses are shown in (a) for various selections placed on the outgoing particles from GEANT4-simulated interactions. The vertex mass as a function of radial distance from the interaction point is shown in (b) showing the materials that make up the various layers of material close to the interaction point.

1101 When using only final-state charged particles with  $p_T$  above 1 GeV with an assumed charged pion mass,  
 1102 reconstructable truth-level vertices can be built. These vertices are then binned in particle multiplicity  
 1103 (using the above definition). The distributions of the masses of these vertices are then fit to an exponential  
 1104 distribution in the region of 5-10 GeV. This fit is then extrapolated into the region above 10 GeV in vertex  
 1105 mass. The disagreement between the integral of the fit function above 10 GeV and that of the truth  
 1106 distribution is seen to be  $\sim 300\%$ . Distributions and fits can be seen in Figure 76.

Not reviewed, for internal circulation only

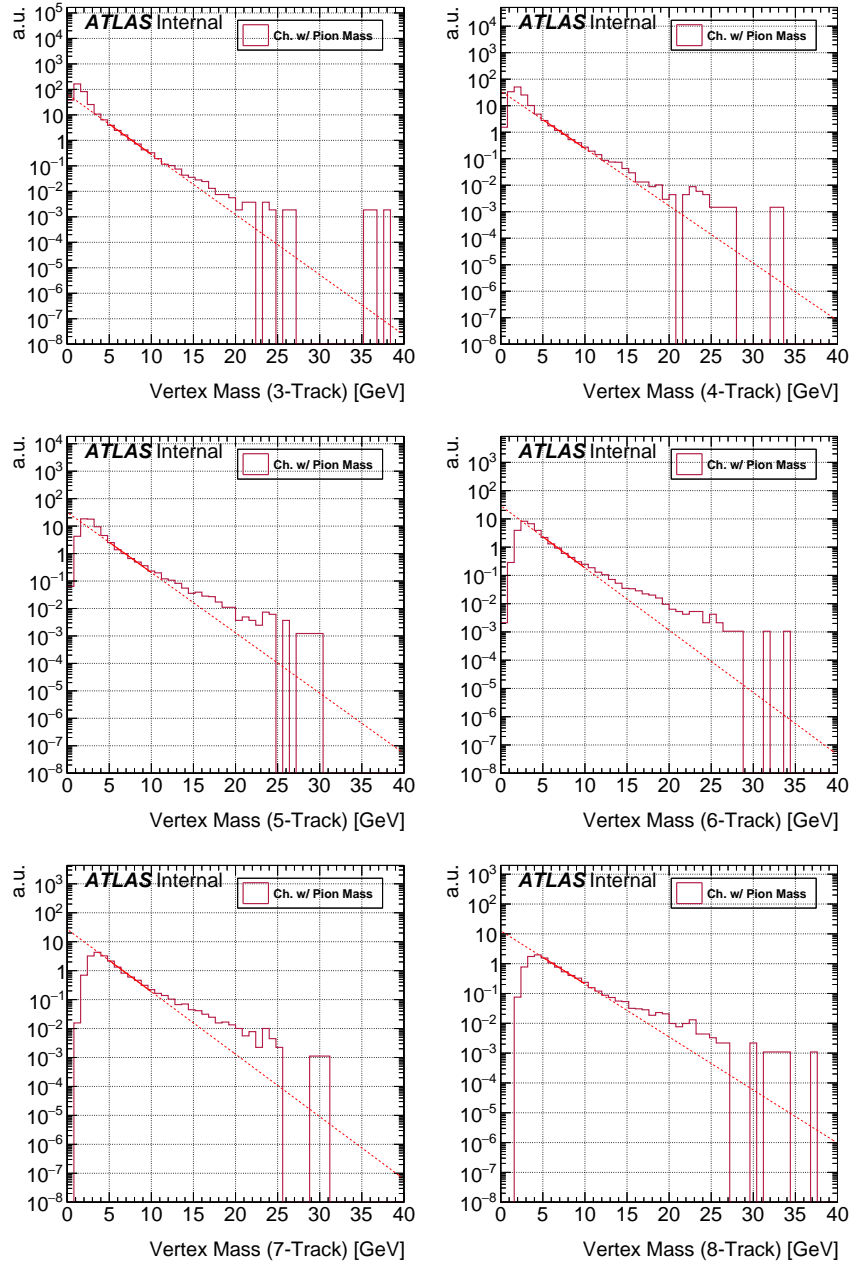


Figure 76: The distributions of reconstructable mass for truth-level vertices is shown binned in the number of reconstructable charged particles. The region between 5-10 GeV is fit to an exponential for comparison in the region above 10 GeV to the truth distribution.

## 1107 G. Vertex pileup dependence

1108 We consider the  $\mu$ - and NPV-dependence of the DV mass and number of tracks. The dependence in data  
 1109 is shown in Figures 77 and 78. We also consider the pileup dependence for signal models with two  
 1110 different lifetimes. In figures 79 and 80, the pileup dependence for the sample 402074 with lifetime 1  
 1111 ns is shown, while in figures 81 and 82, the pileup dependence for the sample 402075 with lifetime 3  
 1112 ns is shown. All of the plots require that the DV passes fiducial,  $\chi^2$ , and displacement cuts as well as the  
 1113 material map veto and the disabled pixel veto.

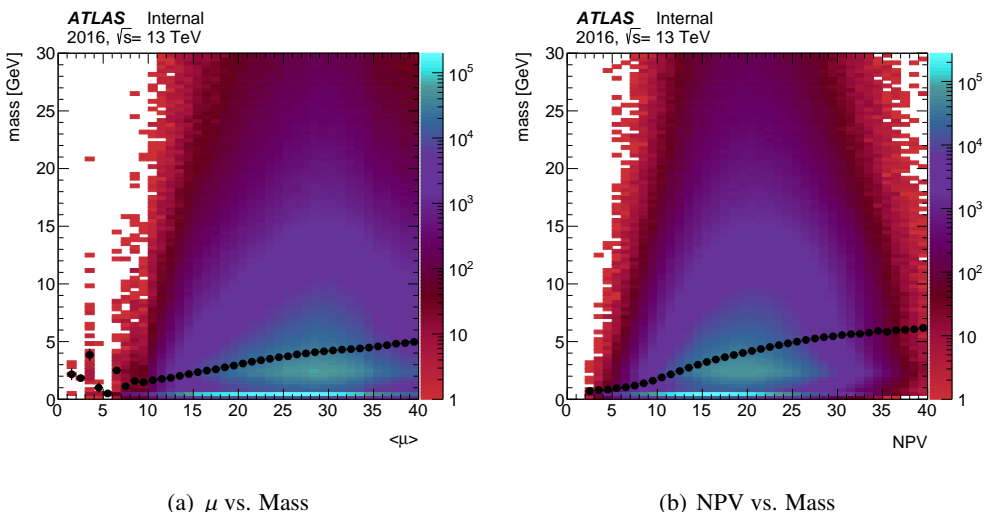


Figure 77: The mass of the displaced vertex is shown as a function of the average number of interactions per bunch crossing  $\langle\mu\rangle$  (Left) and the number of reconstructed primary vertices in the event  $N_{PV}$  (Right). For both plots, the profile is drawn in black.

Not reviewed, for internal circulation only

Not reviewed, for internal circulation only

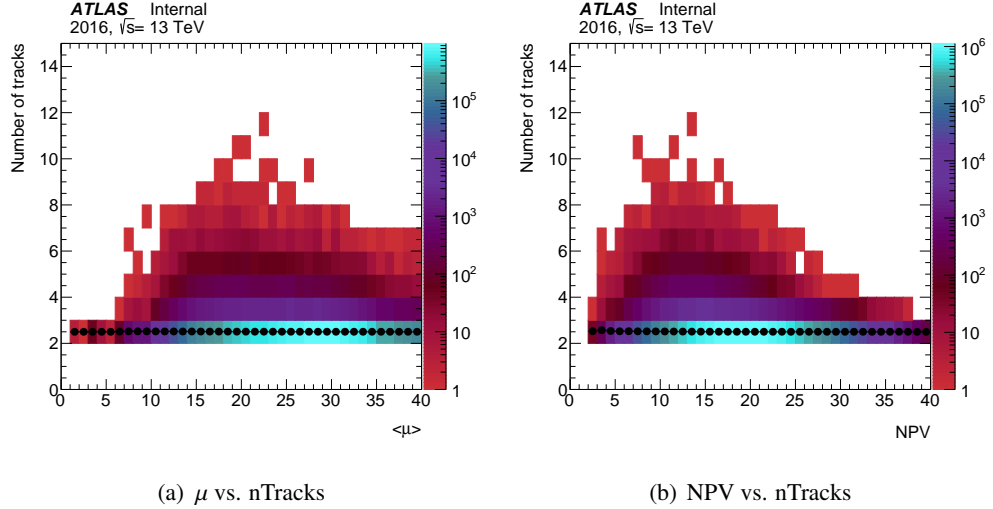


Figure 78: The number of tracks in the displaced vertex in data is shown as a function of the average number of interactions per bunch crossing  $\langle\mu\rangle$  (Left) and the number of reconstructed primary vertices in the event  $N_{PV}$  (Right). For both plots, the profile is drawn in black.

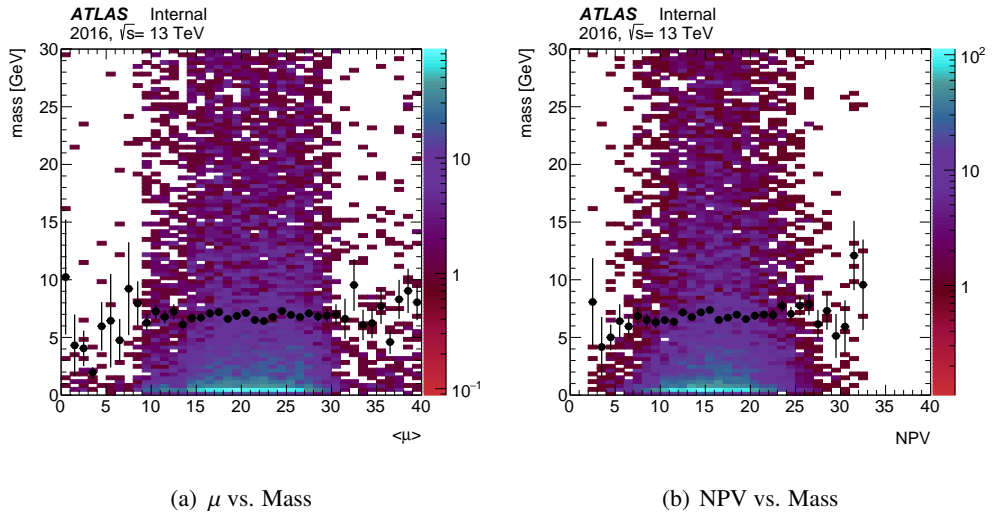


Figure 79: The mass of the displaced vertex in data is shown as a function of the average number of interactions per bunch crossing  $\langle\mu\rangle$  (Left) and the number of reconstructed primary vertices in the event  $N_{PV}$  (Right). For both plots, the profile is drawn in black.

Not reviewed, for internal circulation only

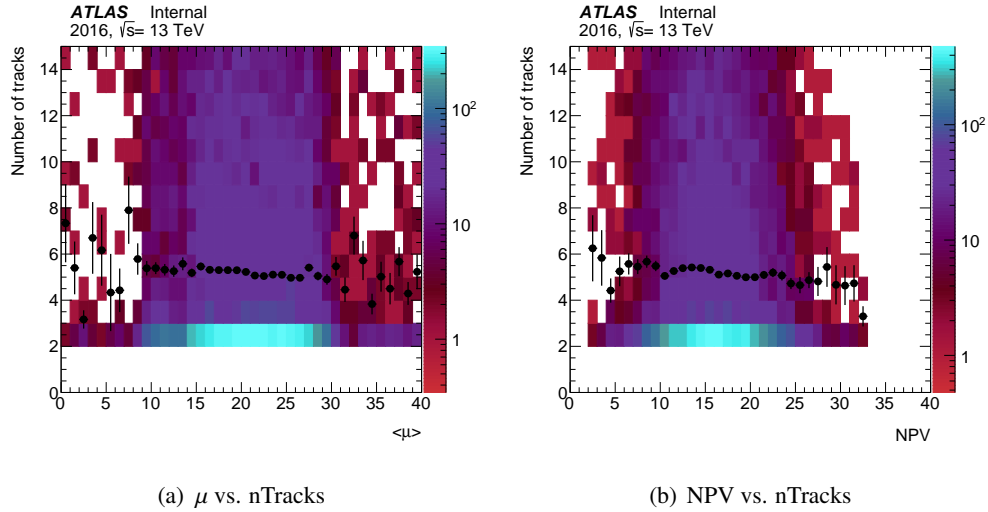


Figure 80: The number of tracks in the displaced vertex is shown as a function of the average number of interactions per bunch crossing  $\langle\mu\rangle$  (Left) and the number of reconstructed primary vertices in the event  $N_{PV}$  (Right). For both plots, the profile is drawn in black.

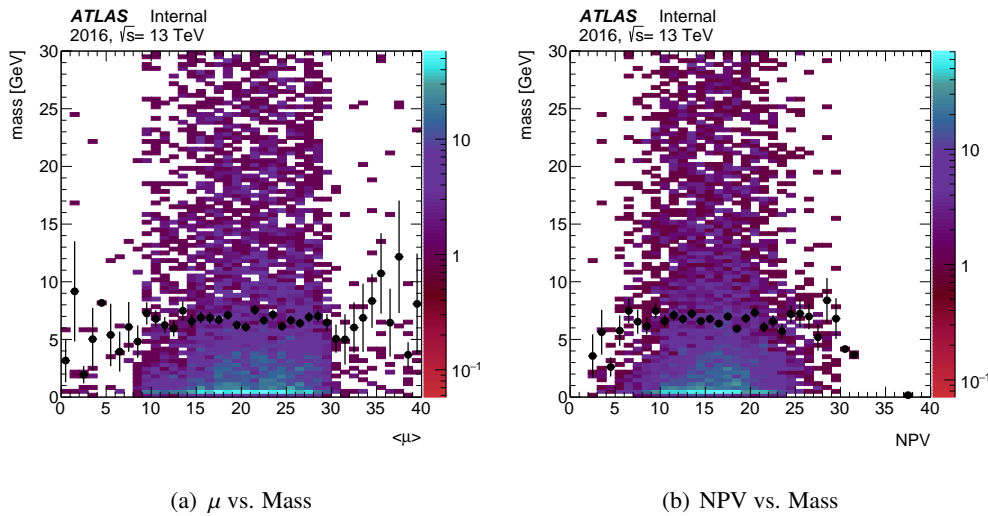


Figure 81: The mass of the displaced vertex is shown as a function of the average number of interactions per bunch crossing  $\langle\mu\rangle$  (Left) and the number of reconstructed primary vertices in the event  $N_{PV}$  (Right). For both plots, the profile is drawn in black.

Not reviewed, for internal circulation only

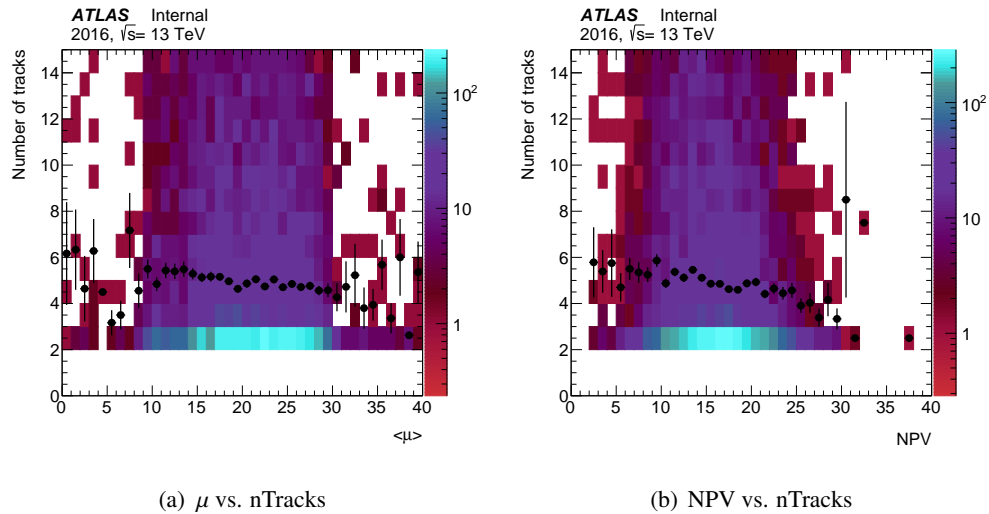


Figure 82: The number of tracks in the displaced vertex is shown as a function of the average number of interactions per bunch crossing  $\langle\mu\rangle$  (Left) and the number of reconstructed primary vertices in the event  $N_{PV}$  (Right). For both plots, the profile is drawn in black.

Not reviewed, for internal circulation only

## 1114 H. Primary vertex reconstruction under R-hadron presence

1115 The cuts applied to the vertex described at Section 3.4 do not prevent an  $R$ -hadron decay vertex to be  
 1116 reconstructed as a primary vertex (PV). This possibility has been studied in this appendix by using a  
 1117 *worst case scenario* MC signal: a large gluino mass with a large  $\Delta m$  assuring enough visible energy in the  
 1118 vertex, and a short generated lifetime in order to enhance the probability for the decay of the  $R$ -hadron be  
 1119 close enough to (0,0,0) or the beam spot definition (DSID: 402777). We used also a intermediate lifetime  
 1120 sample (DSID: 402735) and a very long lifetime (DSID: 402147). The last one shows very few  $R$ -hadrons  
 1121 reconstructed as PVs, becoming irrelevant.

1122 Figure 83 shows the frequency for an  $R$ -hadron to be reconstructed as a PV as function of the radial  
 1123 (transverse plane) decay position in the aforementioned signals. As expected, very close to the origin  
 1124 the probability (frequency) to reconstruct the  $R$ -hadron as PV is maximum, decreasing to negligible rates  
 1125 for larger values, as moves away from the beam spot size. The available statistics of the MC sample  
 1126 (10k events), allow us to check this effect up to  $r_{DV} \simeq 4$  mm for the shorter lifetime. Larger values  
 1127 contains very few events, reaching the maximum distance with a  $R$ -hadron reconstructed as PV around  
 1128  $r_{DV} = 10$  mm in all cases. Figure 84 shows the those  $R$ -hadrons reconstructed as PVs which are also with  
 the highest  $\Sigma_{\text{tracks}} p_T$  in the event.

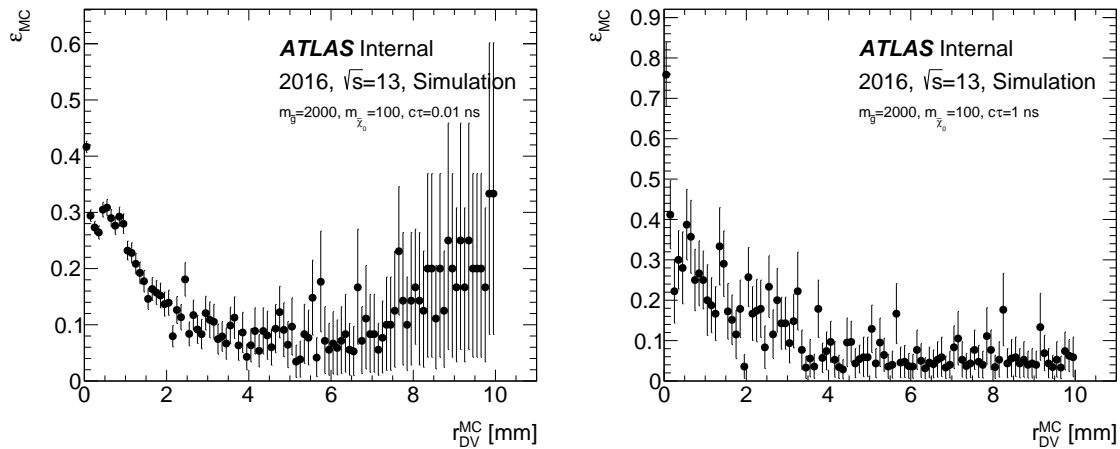


Figure 83: Probability for an  $R$ -hadron to be reconstructed as a PV as a function of true decay radius, for a model with  $m_{\tilde{g}} = 2$  TeV and  $m_{\tilde{\chi}_0} = 100$  GeV generated and with a proper lifetime  $c\tau \simeq 3$  mm (left) and  $c\tau \simeq 300$  mm (right).

1129

1130 Nevertheless, in the cases where one of the  $R$ -hadrons was reconstructed as PV, the secondary vertex  
 1131 reconstruction algorithm is able to, in over 90% of the cases, reconstruct the other  $R$ -hadron as a sec-  
 1132 ondary vertex, as shown in Figure 85. This is indicating that the vertex reconstruction efficiency is not  
 1133 (significantly) affected by the potential reconstruction of an  $R$ -hadron as a PV.

1134 The same MC signal sample has been used to check the reconstruction efficiency for a hard-scattering,  
 1135 showing an almost flat value around 85% for the shorter lifetime sample, and around 60% for the longest  
 1136 one [XXX: reference the PV ATLAS alg? Be careful with the matching!?]; Figure 86 plots the efficiency  
 1137 for the two usual signal samples.

Not reviewed, for internal circulation only

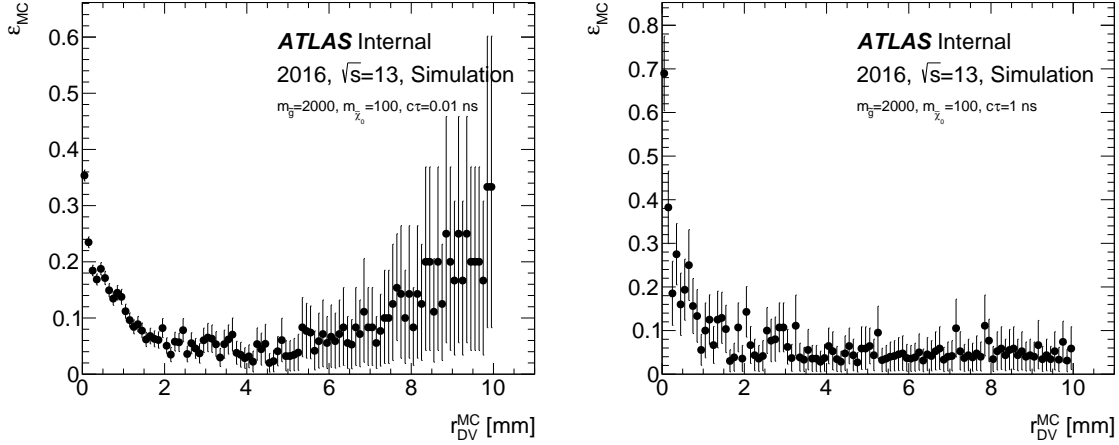


Figure 84: Probability for an  $R$ -hadron to be reconstructed as the PV with highest  $\Sigma_{\text{tracks}} p_T$  in the event, for a model with  $m_{\tilde{g}} = 2 \text{ TeV}$  and  $m_{\tilde{\chi}_0} = 100 \text{ GeV}$  generated and with a proper lifetime  $c\tau \simeq 3 \text{ mm}$  (left) and  $c\tau \simeq 300 \text{ mm}$  (right).

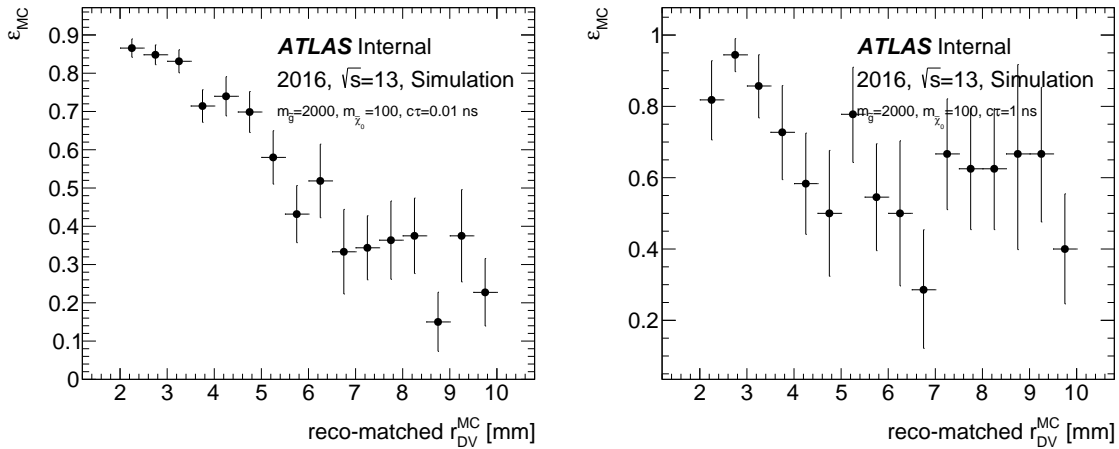


Figure 85: Given an  $R$ -hadron reconstructed as a PV vertex, the figures show the probability for the other  $R$ -hadron in the event to be reconstructed as a SV for the shorter lifetime sample (left), and medium lifetime (right).

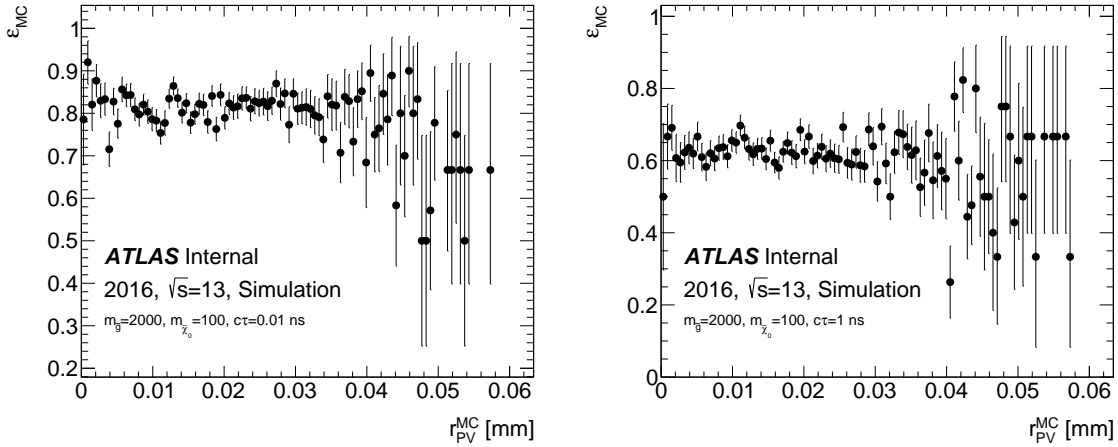


Figure 86: Vertex reconstruction efficiency for the hard-scattering using the ATLAS standard primary vertices algorithm; for a model with  $m_{\tilde{g}} = 2$  TeV and  $m_{\tilde{\chi}_0} = 100$  GeV generated and with a proper lifetime  $c\tau \simeq 3$  mm (left) and  $c\tau \simeq 300$  mm (right).

Not reviewed, for internal circulation only

1138 [NEED TO BE PROPAGATED TO THE SIGNAL EFFICIENCIES AND CHECK THE EFFECT IN  
 1139 THERE]

#### 1140 Reconstruction of PV as a DV

1141 The parallel problem could be present swapping the algorithms: would it be possible that a *real* PV is  
 1142 reconstructed as a DV? It should be noted that it is not applied a minimum cut on the absolute vertex radial  
 1143 position, therefore, *a priori*, it is a valid question. The left plot of Figure 87 shows the (x,y) position of  
 1144 all primary vertices in the whole 2016 DAOD\_RPVLL data. All of them are found to be in the beamspot,  
 1145 less than 1 mm from the origin (0,0). Therefore, given the applied cut to the reconstructed DV to be at  
 1146 a minimum distance of the PV of 4 mm, there will be no DV reconstructed closest, assuring that no real  
 1147 PV can be reconstructed as SV (see Figure 87 right).

Not reviewed, for internal circulation only

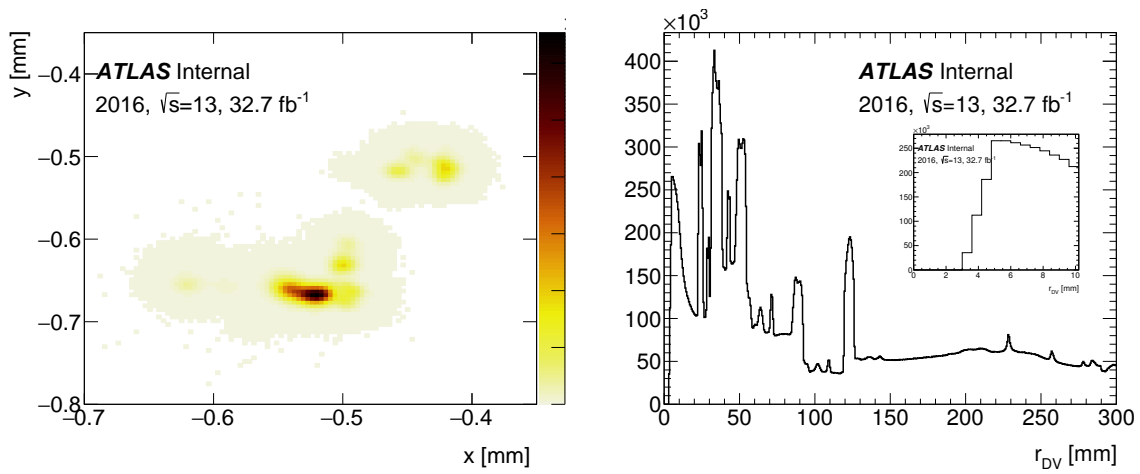


Figure 87: Primary vertices position in the XY-plane for the 2016 data used in the analysis (left). Radial position of the reconstructed SV in the same dataset, with the inset showing the zoomed-in distribution in the first 10 mm. As expected there are no entries for  $r_{\text{DV}} < 3 \text{ mm}$ .

## 1148 I. Lifetime re-weighting

1149 The lifetime re-weighting, explained in Section 4.3, includes an extra factor in order to minimize potential  
 1150 problems due to limited statistics in the samples. Although this factor was applied in the previous  
 1151 versions of this analysis [34], it was never documented (probably because of ). This appendix justify the  
 1152 application of this acceptance factor.

1153 Given a sample with  $N$ -events generated, the number of events with a long-lived particle lifetime decay  
 1154 of  $t_i$  is governed by the exponential decay probability,

$$n_t = \frac{1}{\tau} \sum_{k=1}^N \exp\left(-\frac{t}{\tau}\right) = \frac{N}{\tau} \exp\left(-\frac{t}{\tau}\right) \quad (9)$$

1155 Whenever the proper lifetime is changed, the exponential distribution is changed accordingly, therefore  
 1156 the number evaluated at Equation (9) becomes

$$n_t^{\text{goal}} = \frac{N}{\tau_{\text{goal}}} \exp\left(-\frac{t}{\tau_{\text{goal}}}\right) \quad (10)$$

It is possible to obtain the expected number of events on the new decay distribution by relating its number of events with the original one via a *weight*,

$$n_t^{\text{goal}} = w n_t \Rightarrow w = \frac{\tau}{\tau_{\text{goal}}} \exp\left(-\frac{t}{\tau_{\text{goal}}} + \frac{t}{\tau}\right)$$

1157 Note that this equation in principle holds for every pair simulated-goal lifetime. However, the finite  
 1158 number of simulated events could create artificial properties in the reweighted efficiencies whenever the  
 1159 goal distribution lifetime is away from the simulated and unable to populate enough events. In order to  
 1160 avoid this problem, a cut-off in the reach of the goal lifetime is applied,  $0.3 < \tau_{\text{goal}}/\tau < 3$ , assuring that  
 1161 no more than 1% of the integral over  $\exp(-t/\tau_{\text{goal}})$  is beyond the last generated event.

## 1162 J. JES and JER uncertainties due to displacement

1163 A study of jet response, or the  $p_T$  ratio of reconstructed and truth jets, as a function of jet displacement  
 1164 was completed in order to understand the effects that displaced jets have on the Jet Energy Scale and Jet  
 1165 Energy Resolution. Displaced jet samples from the UEH displaced jets analysis were used to complete  
 1166 this study, because truth jets aren't available in the R Hadron samples used in the DV+MET analysis.  
 1167 Details regarding the,  $\phi \rightarrow ss \rightarrow jets$  sample.

- 1168 • mc15\_13TeV.304820.MadGraphPythia8EvtGen\_A14NNPDF23LO\_HSS LLP\_mH1000\_mS400\_lt5m.merge.D
- 1169 • heavy boson ( $m_\phi$ ) = 1000 GeV
- 1170 • scalars ( $m_s$ ) = 400 GeV
- 1171 •  $c\tau = 5$  m

1172 The heavy boson decays into two scalars,  $s$ , which subsequently decay into two quarks each. The first step  
 1173 in this study was to find the truth displaced vertex arising from where the  $s$  decays into two quarks.  $R_{PV}$ ,  
 1174  $R_{xyPV}$ , and  $Z_{PV}$  are used to study the distance between this displaced vertex and the primary vertex.  
 1175 The displaced vertex is explicitly required to be within the fiducial region of interest for this analysis,  
 1176  $R_{xyPV} < 300$  mm, and  $|Z_{PV}| < 300$  mm. The angle  $\theta$  of each truth quark relative to the vector pointing  
 1177 from the primary vertex to the displaced vertex is used to study the effects of jets which do not point back  
 1178 to the primary vertex.

1179 Each truth quark is matched to the nearest truth jet within a cone of  $\Delta R < 0.4$ . Then each truth jet is  
 1180 matched to the nearest reconstructed jet within a cone of  $\Delta R < 0.4$ . The choice of  $\Delta R < 0.4$ , was made  
 1181 by studying  $\Delta R$  between the reconstructed jet nearest the selected truth jet, and observing that  $R = 0.4$  is  
 1182 more than sufficient to capture jets, even at large distances and angles, see Fig.88. The efficiency of this  
 1183 selection as a function of quark and truth jet  $p_T$  is shown in Fig.89. The matching efficiency increases as  
 1184 a function of jet  $p_T$ , and reaches approximately 100% efficiency for jets with  $p_T > 150$  GeV. In order to  
 1185 confirm that the matching behaves as expected, a comparison of truth quark to matched truth jet  $p_T$ , and  
 1186 truth jet to matched reconstructed jet  $p_T$ , are shown in Fig.90.

1187 In figures 91, 92, and 93, the jet response as a function of several displacement metrics is shown. The  
 1188 mean jet response is overlayed in black, and the rms of each vertical slice is overlayed in grey. Fig.91  
 1189 shows the jet response as a function of the radial distance from the primary vertex, and the radial distance  
 1190 multiplied by  $\sin(\theta)$ . The choice to scale by  $\sin(\theta)$ , was made to multiply jets decaying at a 90 degree  
 1191 angle from the displaced vertex by a factor close to 1, and scale down jets which point back to the  
 1192 primary vertex. Fig.92 shows the jet response as a function of Z, and  $Z\sin(\theta)$ . Finally, Fig.93, shows the  
 1193 jet response as a function of the total distance to the primary vertex, and the angle  $\theta$ .

1194 It is clear that the mean jet response does not change as a function of displacement from the primary  
 1195 vertex. However, the rms of the jet response does change. The width increases from roughly 10% at zero  
 1196 displacement, to 15% at maximal displacement, and this increase primarily comes from jets which do not  
 1197 point back to the primary vertex.

Not reviewed, for internal circulation only

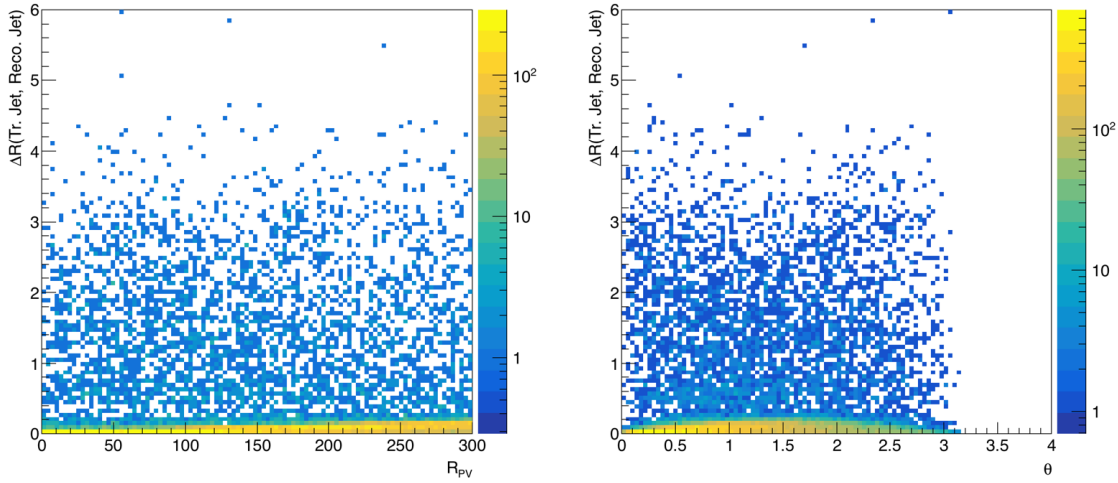


Figure 88:  $\Delta R$  between the reconstructed jet closest to a selected truth jet, as a function of displacement from the primary vertex (left) and angular displacement,  $\theta$  (right).

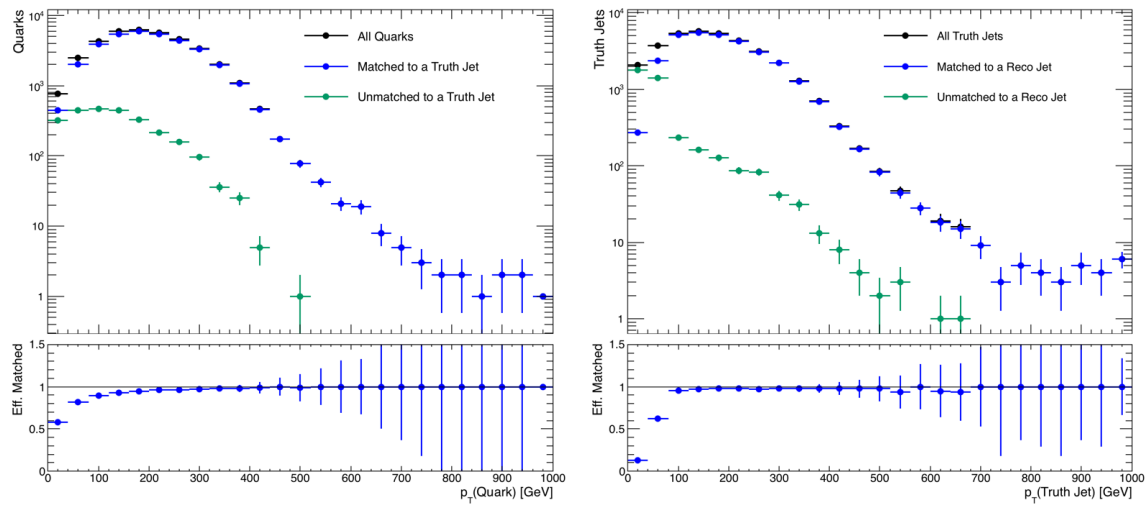


Figure 89: The efficiency for matching a truth quark to a truth jet as a function of truth quark  $p_T$  (left), and the efficiency of matching a truth jet to a reco jet as a function of truth jet  $p_T$  (right).

Not reviewed, for internal circulation only

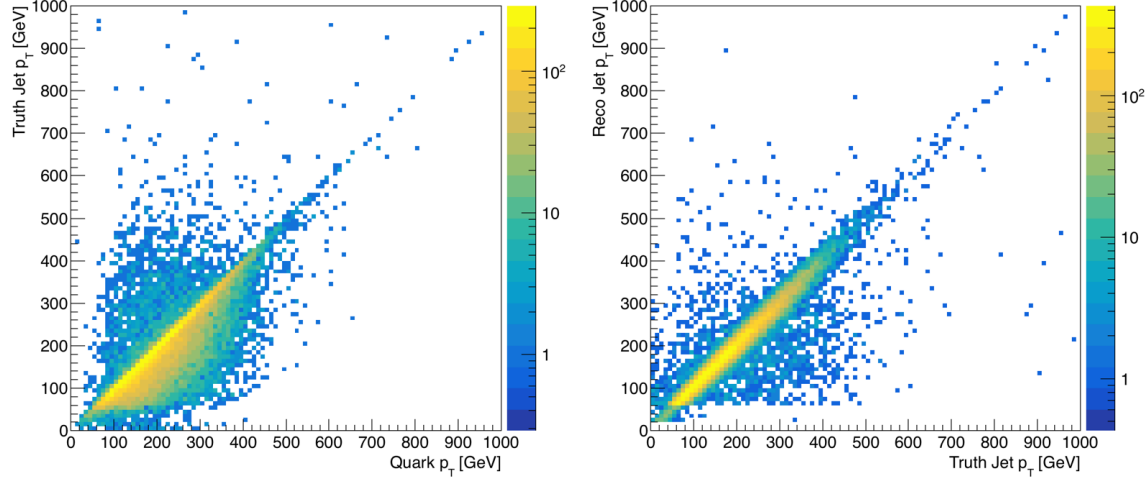


Figure 90: Truth quark  $p_T$  v. matched truth jet  $p_T$  (left), and truth jet  $p_T$  v. matched reconstructed jet  $p_T$  (right), for events where the jets originate from displaced vertices with  $R_{xyPV} < 300$  mm, and  $|Z_{PV}| < 300$  mm.

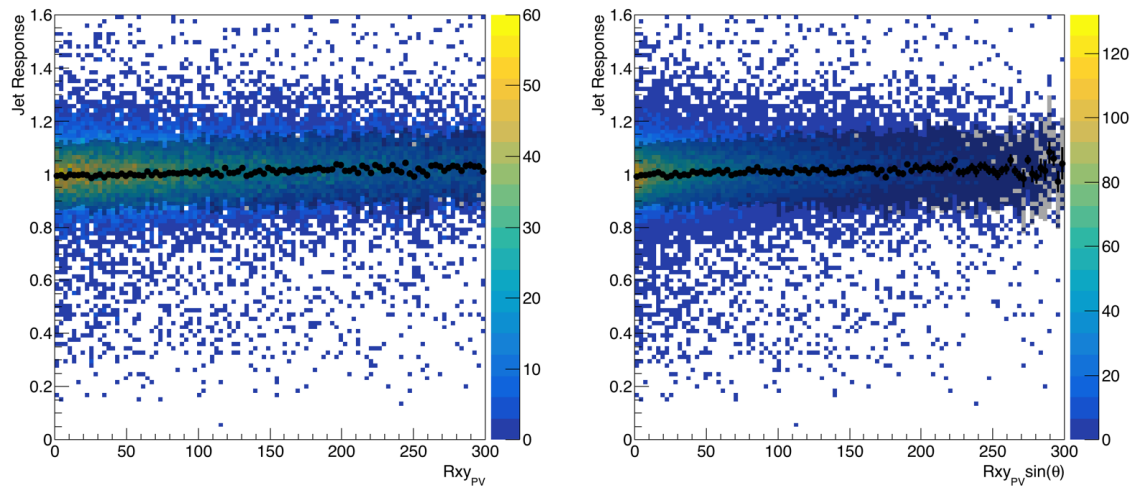


Figure 91: Jet response as a function of  $R_{xy}$  and  $R_{xy} \sin(\theta)$ .

Not reviewed, for internal circulation only

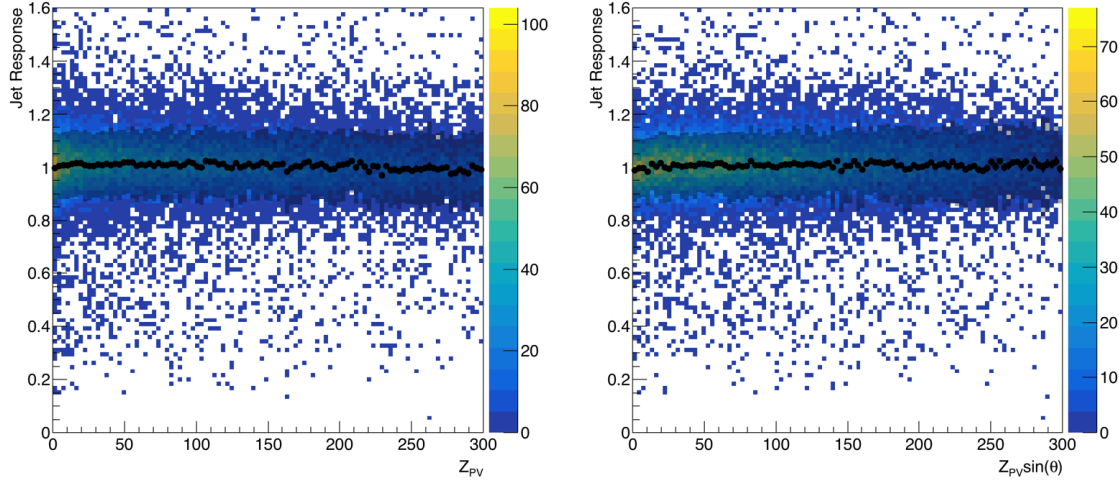


Figure 92: Jet response as a function of  $Z$  and  $Z\sin(\theta)$ .

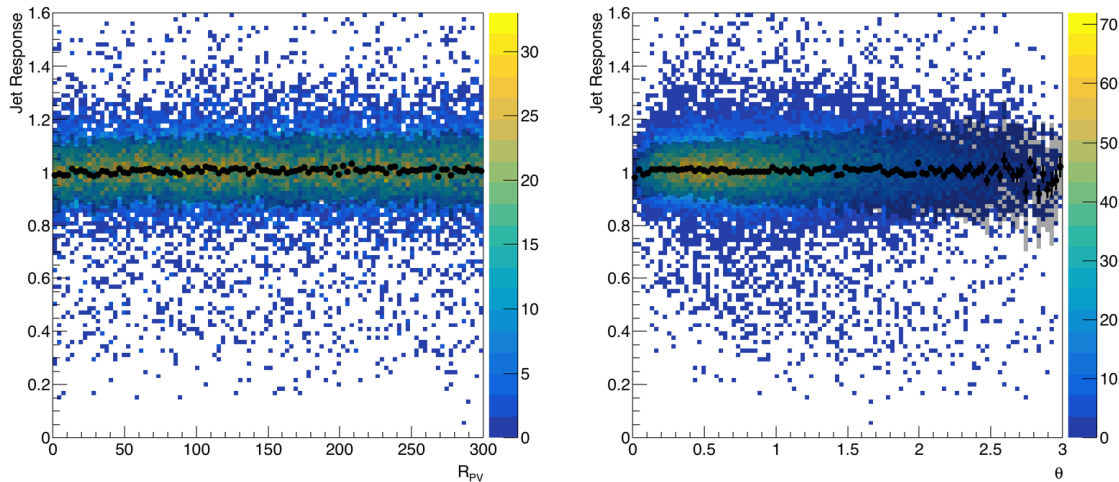


Figure 93: Jet response as a function of  $R$  and  $\theta$ .

## 1198 K. Parametrized Efficiencies for Reinterpretation

### 1199 K.1. Definition of Acceptances

1200 Model independent selection efficiencies are provided for events passing an acceptance defined with  
 1201 particle-level objects. The event-level acceptance  $\mathcal{A}_{\text{Event}}$  is defined by the fraction of events passing  
 1202 particle-level *truth*  $E_T^{\text{miss}}$  and *truth jet* requirements. Event-level efficiencies are provided for those events  
 1203 that have truth  $E_T^{\text{miss}}$  greater than 200 GeV where truth  $E_T^{\text{miss}}$  is defined as the magnitude of the transverse  
 1204 component of the vector sum of stable weakly-interacting particle momenta. In addition, in order to sat-  
 1205 isfy the requirements of the post-trigger filters used in the dedicated data processing used in the analysis,  
 1206 75% of the luminosity must require the existence of either

- 1207 • one truth jet (with  $p_T > 70$  GeV) for which the scalar sum of the charged particle  $p_T$  does not  
 1208 exceed 5 GeV for those particles with small impact parameter with respect to the PV; or
- 1209 • two truth jets (with  $p_T > 25$  GeV) satisfying the same requirement.

1210 Because of changing filter setups, 25% of the luminosity need not satisfy these truth jet requirements, re-  
 1211 taining acceptance for signals without large amounts of displaced jet activity. Finally, an event is required  
 1212 to have an accepted vertex following the prescriptions described below.

1213 The vertex-level acceptance  $\mathcal{A}_{\text{vertex}}$  requires displaced heavy particle decays to have the following prop-  
 1214 erties:

- 1215 • The transverse distance between the IP and the decay position must be greater than 4 mm.
- 1216 • The decay position must lie within the fiducial volume of  $R < 300$  mm and  $|z| < 300$  mm.
- 1217 • The number of *selected decay products* must be at least 5.
- 1218 • The invariant mass of the *truth decay vertex* must be larger than 10 GeV. This mass is calculated  
 1219 using the momenta of the *selected decay products* with a charged pion mass assumption to simulate  
 1220 the assumptions in the analysis vertexing.

1221 The *selected decay products* used in the above *truth decay vertex* construction are those decay products  
 1222 of a given heavy particle decay that satisfy the following conditions:

- 1223 • The particle is charged and stable on timescales required to traverse the tracking volume.
- 1224 • The particle has a transverse momentum  $p_T > 1$  GeV.
- 1225 • The particle has an approximate transverse impact parameter  $d_0 \equiv R \sin \phi > 2$  mm, where  $R$  is  
 1226 the transverse distance between the interaction point and the massive particle decay and  $\phi$  is the  
 1227 azimuthal angle of the particle momentum at its creation.

1228 **K.2. Efficiencies**

1229 Parametrized efficiencies are then provided at the event-level and vertex-level. Because of the inability for  
 1230 the ATLAS detector to fully measure the energy of jets that are produced within or beyond the calorimeter,  
 1231 the event selection efficiency  $\epsilon_{\text{Event}}$  is provided as a function of the truth  $E_{\text{T}}^{\text{miss}}$  described above as well as  
 1232 the transverse distance of the furthest heavy particle decay. These efficiencies can be found in Fig. 94.

1233 In addition to this event-level efficiency, events entering the SR are required to have at least one selected  
 1234 DV. For each heavy particle decay, an efficiency for reconstructing a displaced vertex is provided as a  
 1235 function of truth decay vertex mass, particle multiplicity, and radial detector position. These efficien-  
 1236 cies can be found in Figs. 98 and 99. The effects of the material and disabled pixel module vetoes are  
 1237 encapsulated in the radial binning of these efficiencies.

1238 Overall, the probability that a particular event will fall into the SR is given symbolically by

$$P = \mathcal{A}_{\text{Event}} \times \epsilon_{\text{Event}} \times \left( 1 - \prod_{\text{Vertices}} (1 - \mathcal{A}_{\text{Vertex}} \epsilon_{\text{Vertex}}) \right). \quad (11)$$

1239 Event level efficiencies are also shown as a function of truth MET and the mass splitting between the long  
 1240 lived gluino and neutralino in Fig. 95. Event level efficiencies are lower for smaller mass splittings by  
 1241 nearly 50%. The efficiencies from event level cuts are dominated by two cuts in particular, the DRAW  
 1242 filter's trackless jet requirement, and the offline cut on reconstructed MET. Figure 96 shows the efficiency  
 1243 of passing the DRAW trackless jet requirement,  $\geq 1$  jet with  $p_T > 70$  GeV, or  $\geq 2$  jets with  $p_T > 25$  GeV,  
 1244 applied randomly to 75% of events, as a function of truth MET and mass splitting. Events with small mass  
 1245 splitting are much more likely to fail this requirement than those with a higher mass splitting. Figure 97  
 1246 shows the efficiency of passing the offline MET requirement of  $MET > 250$  GeV, as a function of truth  
 1247 MET and mass splitting. Low mass splittings and High mass splittings have consistent MET efficiencies  
 1248 and turn ons when all truth vertices decay before the calorimeter. However, once a decay is displaced  
 1249 enough that it occurs inside the calorimeter, the MET efficiency degrades for higher mass splittings only.  
 1250 This effect is due to the fact that for low mass splittings, a heavy neutralino is produced without much  
 1251 intrinsic momentum, unless in the presence of a large amount of ISR. ISR jets are prompt, so the MET  
 1252 resolution does not degrade as a function of displacement. For large mass splittings, neutralinos are  
 1253 light and produce intrinsic MET. This MET resolution is significantly degraded if the neutralino becomes  
 1254 displaced.

Not reviewed, for internal circulation only

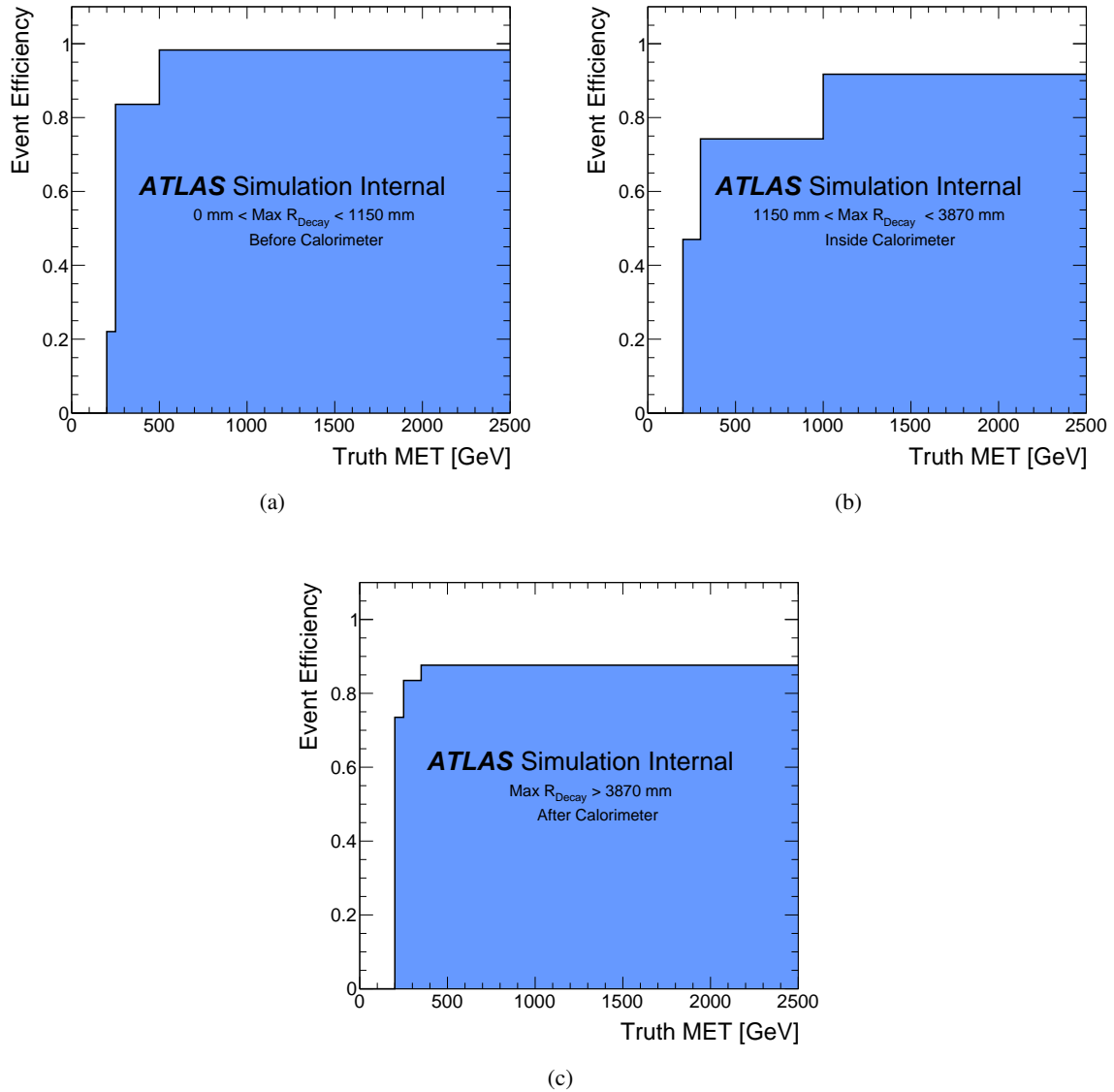


Figure 94: Parameterized event selection efficiencies are shown as a function of truth MET. The truth MET is defined to be the transverse momentum of all invisible particles in the event. Event level efficiencies are evaluated for events which have truth MET  $> 200$  GeV, pass a trackless jet requirement (70% of events must have  $\geq 1$  trackless jet with  $p_T > 70$  GeV or  $\geq 2$  trackless jets with  $p_T > 25$  GeV, to emulate the DRAW filter), and have at least 1 displaced truth decay. This truth decay must have  $\geq 5$  associated truth tracks, (i.e tracks with nonzero electric charge,  $p_T > 1$  GeV, and  $d0 > 2$  mm), an invariant mass  $> 10$  GeV, and be in the region  $4 \text{ mm} < R_{\text{Decay}} < 300$  mm, and  $|Z_{\text{Decay}}| < 300$  mm. To satisfy the event level efficiency, events must then pass the *full event selection*, as defined in Sect. 3. The event efficiencies are evaluated separately for events which have all truth decay vertices occurring before the start of the ATLAS calorimeter, the farthest truth decay occurring inside the calorimeter, and the farthest decay occurring after the end of the ATLAS calorimeter.

Not reviewed, for internal circulation only

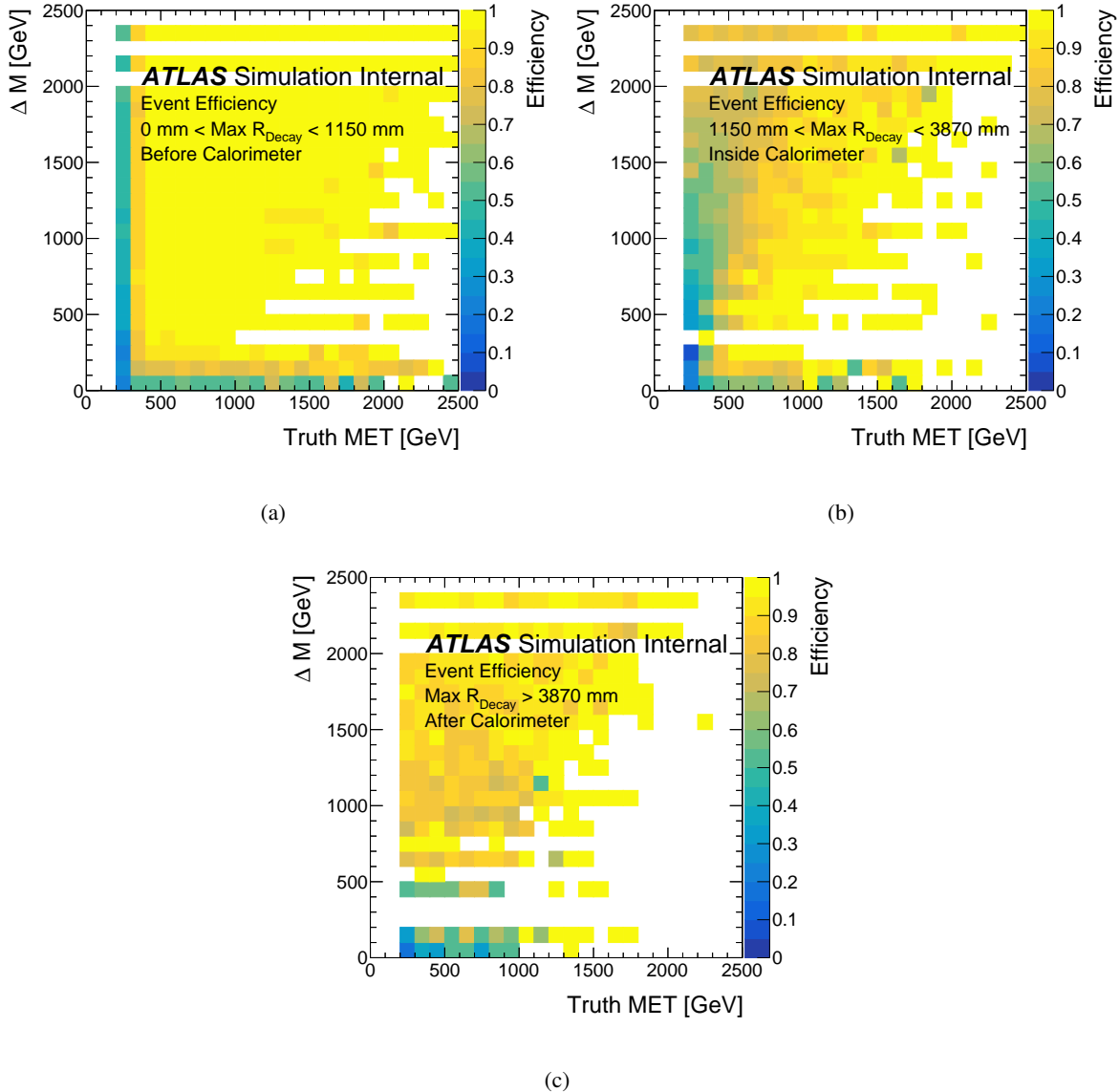


Figure 95: Parameterized event selection efficiencies as a function of truth MET and mass splitting.

Not reviewed, for internal circulation only

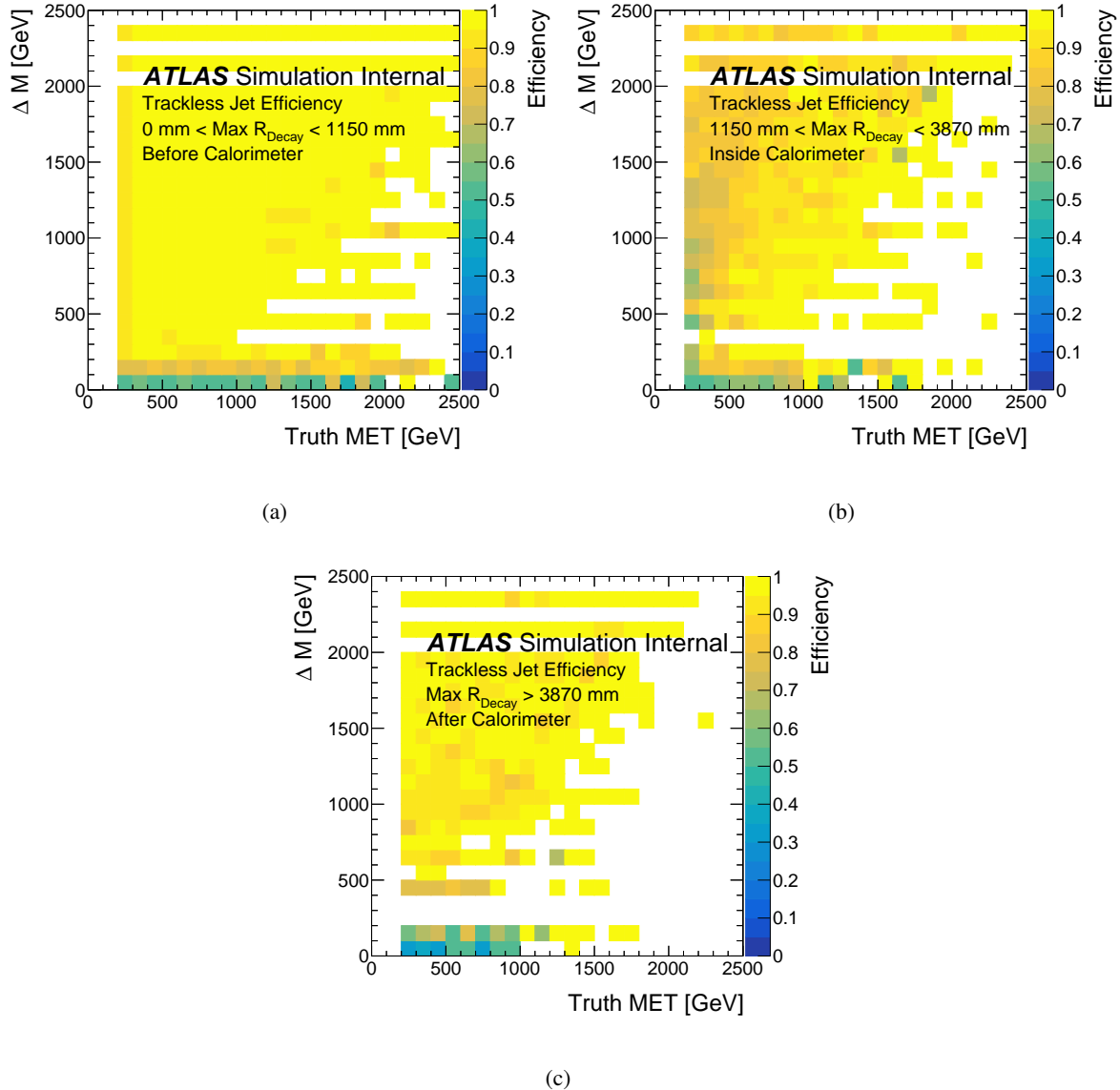


Figure 96: Parameterized trackless jet efficiencies as a function of truth MET and mass splitting.

Not reviewed, for internal circulation only

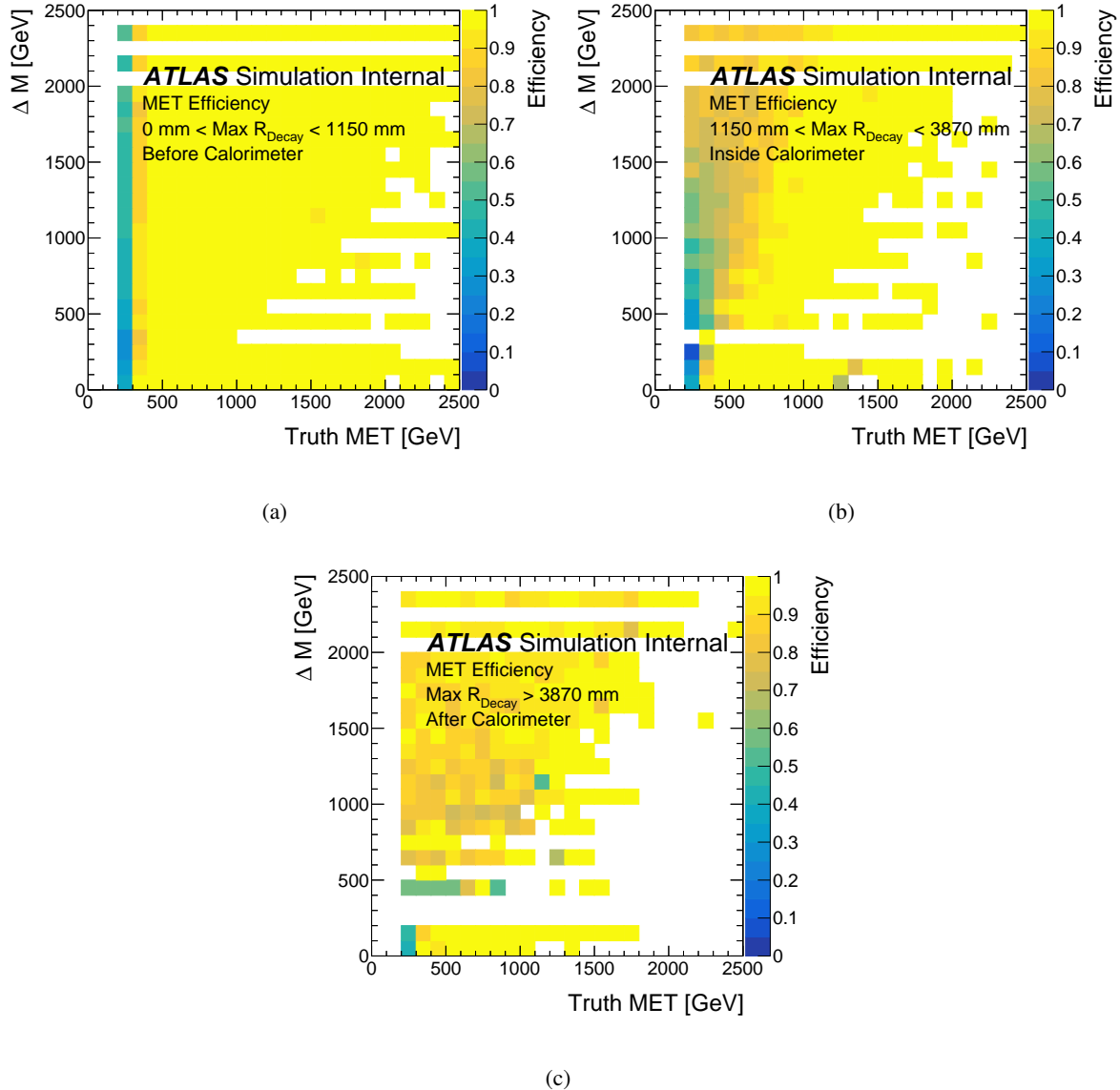


Figure 97: Parameterized MET efficiencies as a function of truth MET and mass splitting.

Not reviewed, for internal circulation only

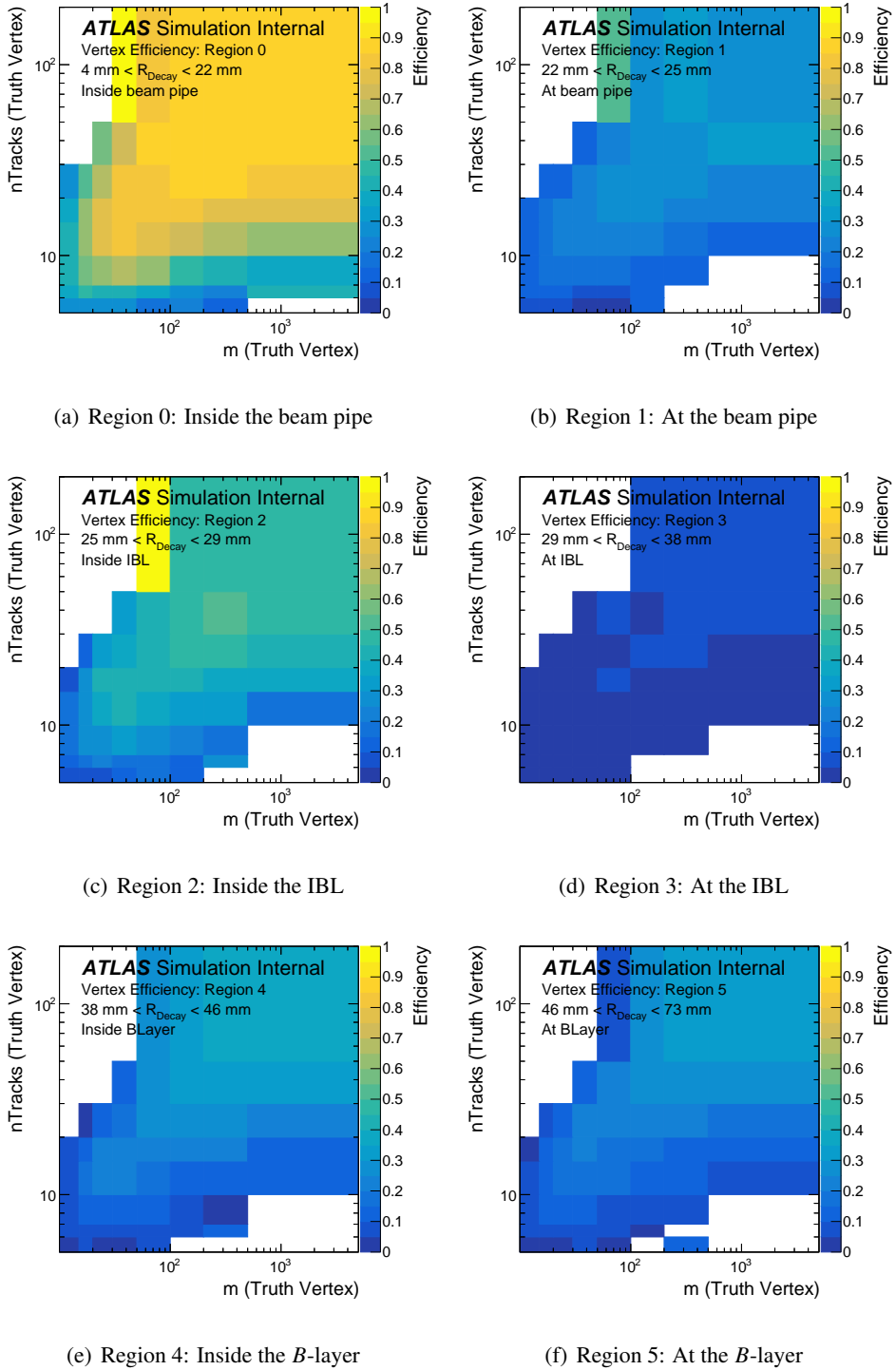


Figure 98: Parameterized vertex level efficiencies as a function of number of tracks associated to a truth decay vertex, and the vertex invariant mass. Truth tracks are required to have nonzero electric charge,  $p_T > 1 \text{ GeV}$ , and  $d0 > 2 \text{ mm}$ . The per-vertex efficiency is evaluated only for truth decay vertices which have at least 5 associated tracks, an invariant mass  $> 10 \text{ GeV}$ , and be in the region  $4 \text{ mm} < R_{\text{DecayVertex}} < 300 \text{ mm}$ , and  $|Z_{\text{DecayVertex}}| < 300 \text{ mm}$ . A truth vertex satisfies the vertex level efficiency if it can be matched to a reconstructed vertex which passes the *final vertex selection* as defined in Sect. 3. Vertex level efficiencies are given separately for each radial region.

Not reviewed, for internal circulation only

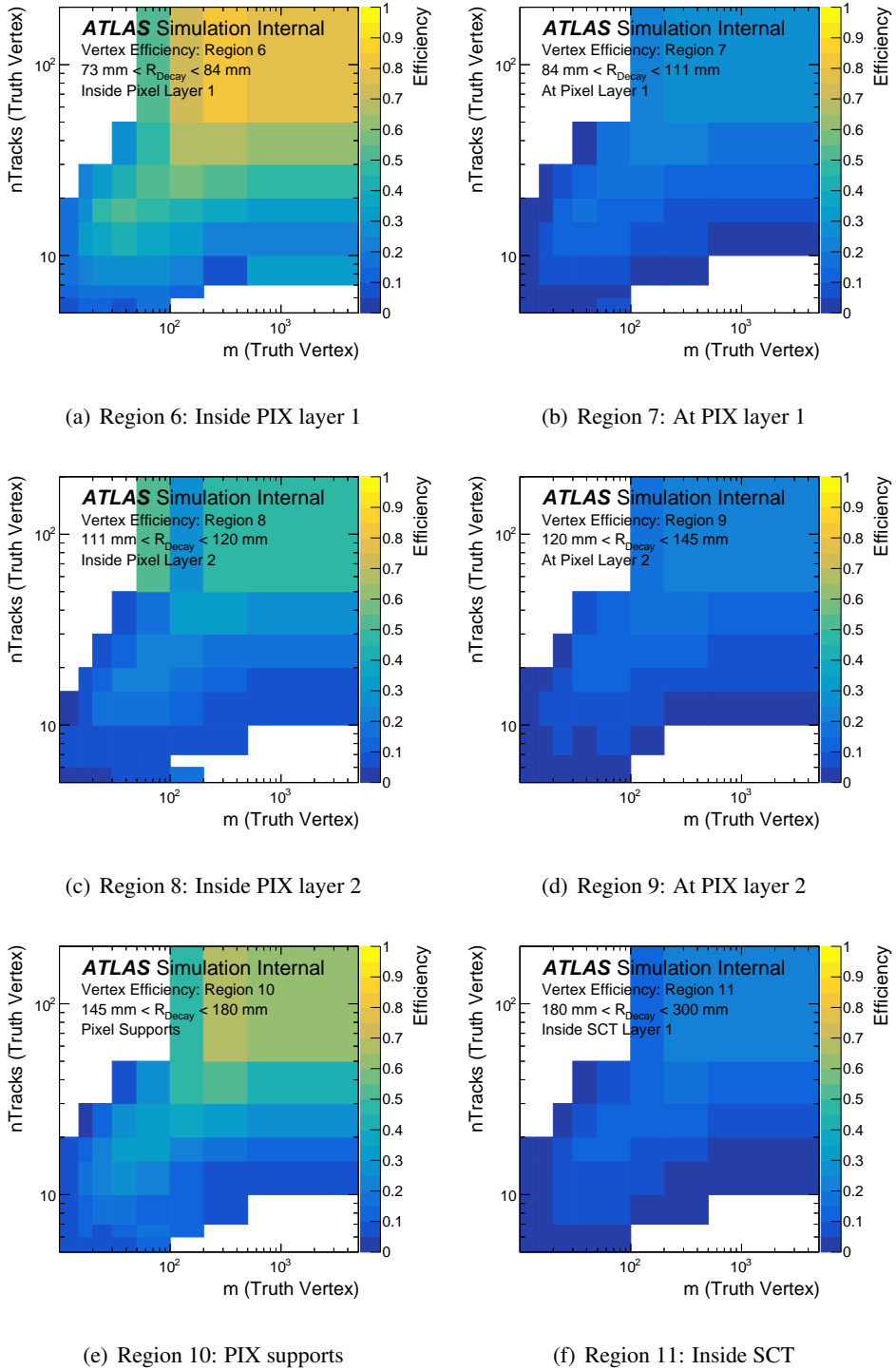


Figure 99: Parameterized vertex level efficiencies as a function of number of tracks associated to a truth decay vertex, and the vertex invariant mass. Truth tracks are required to have nonzero electric charge,  $p_T > 1 \text{ GeV}$ , and  $d_0 > 2 \text{ mm}$ . The per-vertex efficiency is evaluated only for truth decay vertices which have at least 5 associated tracks, an invariant mass  $> 10 \text{ GeV}$ , and be in the region  $4 \text{ mm} < R_{\text{DecayVertex}} < 300 \text{ mm}$ , and  $|Z_{\text{DecayVertex}}| < 300 \text{ mm}$ . A truth vertex satisfies the vertex level efficiency if it can be matched to a reconstructed vertex which passes the *final vertex selection* as defined in Sect. 3. Vertex level efficiencies are given separately for each radial region.

---

**K.3. Closure Test**

In order to ensure the accuracy of these parametrized efficiencies, a closure test was performed. For four samples, the probability of an event passing was calculated using the event and vertex level efficiency histograms, as well as the procedure described above. The predicted number of events passing selection is defined as the sum of probabilities. This prediction is compared to the actual number of events passing the full event and vertex level selections. The predicted and observed number events passing selection agree within 10%. The results of this closure test are shown in Table 19.

$\Delta m$ [GeV]	$\tau$ [ns]	DSID	$A_{EVT}$	$A_{VTX}$	$A_{TOT}$	$E_{EVT}$	$E_{VTX}$	$E_{TOT}$	Pred % Evts Passing	Observed % Evts Passing	Closure
1900	0.1	402793	0.86	0.83	0.74	0.93	0.85	0.79	0.58	0.57	1.6
1900	10	402145	0.93	0.36	0.33	0.89	0.36	0.32	0.11	0.10	2.5
100	0.1	403090	0.09	0.64	0.06	0.70	0.52	0.37	0.022	0.024	10.67
100	10	403089	0.11	0.28	0.03	0.71	0.17	0.12	0.004	0.004	1.5

Table 19: Results of the closure test for four signal samples are shown above. The mass splitting and lifetime of each sample is provided along with the vertex and event level acceptance, as well as the predicted efficiencies. The predicted percentage of events passing the full selection is compared to the observed number of events passing the full selection, along with the overall closure.

## 1262 References

- 1263 [1] M. Fairbairn, A. C. Kraan, D. A. Milstead, T. Sjostrand, P. Z. Skands and T. Sloan,  
 1264 *Stable massive particles at colliders*, *Phys. Rept.* **438** (2007), arXiv: [0611040 \[hep-ph\]](#).
- 1265 [2] ATLAS Collaboration, *Search for displaced vertices arising from decays of new heavy particles*  
 1266 *in 7 TeV pp collisions at ATLAS*, *Phys. Lett. B* **707** (2012) 478, arXiv: [1109.2242 \[hep-ex\]](#).
- 1267 [3] ATLAS Collaboration, *Search for Heavy Medium-Lived Particles at ATLAS*, (2011),  
 1268 URL: <https://cds.cern.ch/record/1329851>.
- 1269 [4] H. K. Dreiner, *An Introduction to explicit R-parity violation*,  
 1270 (1997), [Adv. Ser. Direct. High Energy Phys.21,565(2010)], arXiv: [hep-ph/9707435 \[hep-ph\]](#).
- 1271 [5] ATLAS Collaboration, *Search for long-lived, heavy particles in final states with a muon and*  
 1272 *multi-track displaced vertex in proton–proton collisions at  $\sqrt{s} = 7$  TeV with the ATLAS detector*,  
 1273 *Phys. Lett. B* **719** (2013) 280, arXiv: [1210.7451 \[hep-ex\]](#).
- 1274 [6] ATLAS Collaboration, *Update of search for displaced vertices arising from decays of new heavy*  
 1275 *particles in  $\sqrt{s} = 7$  TeV pp collisions at ATLAS*, (2012),  
 1276 URL: <https://cds.cern.ch/record/1454874>.
- 1277 [7] ATLAS Collaboration, *Search for long-lived, heavy particles in final states with a muon and a*  
 1278 *multi-track displaced vertex in proton–proton collisions at  $\sqrt{s} = 8$  TeV with the ATLAS detector*,  
 1279 ATLAS-CONF-2013-092, 2013, URL: <http://cdsweb.cern.ch/record/1595755>.
- 1280 [8] ATLAS Collaboration,  
 1281 *Search for long-lived, heavy particles using a muon and multi-track displaced vertex, in pp*  
 1282 *collisions at  $\sqrt{s} = 8$  TeV centre-of-mass energy, with the ATLAS detector at the LHC*, (2013),  
 1283 URL: <https://cds.cern.ch/record/1558398>.
- 1284 [9] ATLAS Collaboration, *Search for massive, long-lived particles using multitrack displaced*  
 1285 *vertices or displaced lepton pairs in pp collisions at  $\sqrt{s} = 8$  TeV with the ATLAS detector*,  
 1286 *Phys. Rev. D* **92** (2015) 072004, arXiv: [1504.05162 \[hep-ex\]](#).
- 1287 [10] ATLAS Collaboration, *Search for long-lived, heavy particles using a multi-track displaced vertex*,  
 1288 *in pp collisions at 8 TeV centre-of-mass energy, with the ATLAS detector at the LHC*, (2014),  
 1289 URL: <https://cds.cern.ch/record/1697551>.
- 1290 [11] ATLAS Collaboration, *Search for long-lived, massive particles decaying into leptons in pp*  
 1291 *collisions at 8 TeV centre-of-mass energy, with the ATLAS detector at the LHC*, (2014),  
 1292 URL: <https://cds.cern.ch/record/1749971>.
- 1293 [12] A. Arvanitaki, N. Craig, S. Dimopoulos, and G. Villadoro, *Mini-Split*, *JHEP* **1302** (2013),  
 1294 arXiv: [1210.0555 \[hep-ph\]](#).
- 1295 [13] P. Meade, M. Reece, D. Shih, *Long-Lived Neutralino NLSPs*, *JHEP* **1010** (2010),  
 1296 arXiv: [1006.4575 \[hep-ph\]](#).
- 1297 [14] N. Nagata, H. Otono, S. Shirai, *Probing Bino-Gluino Coannihilation at the LHC*,  
 1298 *Phys. Lett. B* **748** (2015), arXiv: [1504.00504 \[hep-ph\]](#).
- 1299 [15] (), URL: <https://twiki.cern.ch/twiki/bin/viewauth/AtlasProtected/LongLivedDpd>.
- 1300 [16] (), URL: [https://twiki.cern.ch/twiki/bin/viewauth/Atlas/Special2016Reprocessing#20\\_Processing\\_of\\_2016\\_DRAW\\_RPVLL](https://twiki.cern.ch/twiki/bin/viewauth/Atlas/Special2016Reprocessing#20_Processing_of_2016_DRAW_RPVLL).

- Not reviewed, for internal circulation only
- 1302 [17] *SUSY15 Derivation*, (),  
1303 URL: <https://svnweb.cern.ch/trac/atlasoff/browser/PhysicsAnalysis/>  
1304 [DerivationFramework/DerivationFrameworkSUSY/trunk/share/SUSY15.py](#).
  - 1305 [18] ATLAS Collaboration, *Search for long-lived stopped gluino R-hadrons decaying out-of-time with*  
1306 *LHC collisions in 2011 and 2012 using the ATLAS detector*, (2013),  
1307 URL: <https://cds.cern.ch/record/1548127>.
  - 1308 [19] T. Sjöstrand, S. Mrenna, and P. Z. Skands, *PYTHIA 6.4 Physics and Manual*, **JHEP** **10** (2006),  
1309 arXiv: [0603175 \[hep-ph\]](https://arxiv.org/abs/0603175).
  - 1310 [20] S. Agostinelli *et al.* [GEANT4 Collaboration], *GEANT4: A simulation toolkit*, ().
  - 1311 [21] *MC15 processing*, (), URL: <https://twiki.cern.ch/twiki/bin/view/AtlasProtected/CentralMC15ProductionList>.
  - 1313 [22] T. Sjöstrand, S. Mrenna, and P. Z. Skands, *A Brief Introduction to PYTHIA 8.1*,  
1314 *Comput. Phys. Commun.* **178** (2008), arXiv: [0710.3820 \[hep-ph\]](https://arxiv.org/abs/0710.3820).
  - 1315 [23] (), URL: <https://twiki.cern.ch/twiki/bin/viewauth/AtlasProtected/ExtendedPileupReweighting>.
  - 1317 [24] *MC tunes internal ATLAS twiki page*, (),  
1318 URL: <https://twiki.cern.ch/twiki/bin/view/AtlasProtected/MCTunes>.
  - 1319 [25] (), URL: [https://twiki.cern.ch/twiki/bin/view/Atlas/DataPreparationCheckListForPhysicsAnalysis#Rejection\\_of\\_bad\\_corrupted\\_event](https://twiki.cern.ch/twiki/bin/view/Atlas/DataPreparationCheckListForPhysicsAnalysis#Rejection_of_bad_corrupted_event).
  - 1322 [26] (), URL: <https://twiki.cern.ch/twiki/bin/viewauth/AtlasComputing/SoftwareTutorialxAODAnalysisInROOT>.
  - 1324 [27] ATLAS Collaboration,  
1325 *Reconstruction of tracks with large impact parameter in the Inner Detector*, (2012),  
1326 URL: <https://cds.cern.ch/record/1416389>.
  - 1327 [28] T Cornelissen et al.,  
1328 ‘Concepts, Design and Implementation of the ATLAS New Tracking (NEWT)’,  
1329 tech. rep. ATL-SOFT-PUB-2007-007. ATL-COM-SOFT-2007-002, CERN, 2007,  
1330 URL: <https://cds.cern.ch/record/1020106>.
  - 1331 [29] ATLAS Collaboration, *Mapping the material in the ATLAS Inner Detector using secondary*  
1332 *hadronic interactions in 7 TeV collisions*, ATLAS-CONF-2010-058, 2010,  
1333 URL: <http://cdsweb.cern.ch/record/1281331>.
  - 1334 [30] ATLAS Collaboration,  
1335 *Studies of the ATLAS Inner Detector material using  $\sqrt{s} = 13$  TeV pp collision data*,  
1336 ATL-PHYS-PUB-2015-050, 2015, URL: <http://cdsweb.cern.ch/record/2109010>.
  - 1337 [31] ATLAS Collaboration, *Studies of the material within the Run 2 ATLAS Inner Detector*, (2016),  
1338 URL: <https://cds.cern.ch/record/2126848>.
  - 1339 [32] S. R. Das, *On a new approach for finding all the modified cut-sets in an incompatibility graph*,  
1340 IEEE Transactions on Computers **C-22** (2 1973).

- 1341 [33] S. H. Oh and C Wang,  
 1342 ‘Kshort and Lambda Production In Jets from pp Collisions at 7 TeV Center-of-Mass Energy.’,  
 1343 tech. rep. ATL-COM-PHYS-2014-1258, CERN, 2014,  
 1344 URL: <https://cds.cern.ch/record/1951024>.
- 1345 [34] N Barlow et al., ‘Search for long-lived, heavy particles using a multi-track displaced vertex, in  $pp$   
 1346 collisions at 8 TeV centre-of-mass energy, with the ATLAS detector at the LHC.’,  
 1347 tech. rep. ATL-COM-PHYS-2014-370, CERN, 2014,  
 1348 URL: <https://cds.cern.ch/record/1697511>.
- 1349 [35] (), URL: <https://twiki.cern.ch/twiki/bin/viewauth/AtlasProtected/SUSYSignalUncertainties>.
- 1350 [36] 2016 Period-A Run Information, (), URL: <https://twiki.cern.ch/twiki/bin/view/AtlasProtected/DetailedInformationPeriodAIn2016>.
- 1351 [37] ‘Further ATLAS tunes of PYTHIA6 and Pythia 8’, tech. rep. ATL-PHYS-PUB-2011-014,  
 1352 CERN, 2011, URL: <https://cds.cern.ch/record/1400677>.
- 1353 [38] A. Sherstnev and R. S. Thorne, *Parton Distributions for LO Generators*,  
 1354 Eur. Phys. J. **C55** (2008) 553, arXiv: [0711.2473 \[hep-ph\]](https://arxiv.org/abs/0711.2473).
- 1355 [39] *TrackingCP Loose Selection*, (), URL: [https://twiki.cern.ch/twiki/bin/view/AtlasProtected/TrackingCPICHEP2016#Track\\_Selectio](https://twiki.cern.ch/twiki/bin/view/AtlasProtected/TrackingCPICHEP2016#Track_Selectio).
- 1356 [40] ‘Track Reconstruction Performance of the ATLAS Inner Detector at  $\sqrt{s} = 13$  TeV’,  
 1357 tech. rep. ATL-PHYS-PUB-2015-018, CERN, 2015,  
 1358 URL: <https://cds.cern.ch/record/2037683>.
- 1359 [41] *TrackingCP LRT group*, (), URL: <https://twiki.cern.ch/twiki/bin/viewauth/AtlasProtected/TrackingCPLargeRadius>.

---

**1364 List of contributions**

Not reviewed, for internal circulation only

	Karri DiPetrillo	JES/JER vs displacement studies. AUX material construction and planning. Paper editing. DRAW filter responsibilities.
	Jordi Duarte-Campos	Coordination of the group, main responsibility for analysis strategy, main contributor to large-radius tracking effort, secondary vertexing, development of analysis framework
	Dominik Krauss	Development of analysis framework
	Lawrence Lee Jr	Material map studies, design of non-collision background veto, work on disabled pixel modules, development of low- $E_T^{\text{miss}}$ VR, cross-checks of yields and efficiencies, student supervision, paper editor.
1365	Kazuki Motohashi	Main analyst, development of background estimation methods, material-enriched VR design, signal MC development, DRAW filter development, signal efficiency calculation, assessment of systematic uncertainties.
	Christian Ohm	Coordination of the group, main responsibility for analysis strategy, non-collision background studies, development of analysis framework, design of analysis ntuple, ntuple production, event-picking and event displays, main paper editor.
	Hideyuki Oide	Support and maintenance of secondary vertexing algorithm
	Hidetoshi Otono	Turn-on curves for trigger and DRAW $E_T^{\text{miss}}$ cut, signal MC development, student supervision
	Nora Emilia Pettersson	Background estimation, large-radius tracking, material map studies.
	Jennifer Roloff	Studies of the material map and design of disabled-modules veto, pileup dependence.
1366	Abner Soffer	Statistical interpretation, limit calculations, general supervision

---

## 1367 Auxiliary material

1368 In an ATLAS paper, auxiliary plots and tables that are supposed to be made public should be collected in  
1369 an appendix that has the title ‘Auxiliary material’. This appendix should be printed after the Bibliography.  
1370 At the end of the paper approval procedure, this information can be split into a separate document – see  
1371 `atlas-auxmat.tex`.

1372 In an ATLAS note, use the appendices to include all the technical details of your work that are relevant  
1373 for the ATLAS Collaboration only (e.g. dataset details, software release used). This information should  
1374 be printed after the Bibliography.